NOTICES

When Government drawings, specifications, or other data are used for
any purpose other than in connection with a definitely related Government
procurement operation, the United States Government thereby incurs no
responsibility nor any obligation whatsoever; and the fact that the Govern-
ment may have formulated, furnished, or in any way supplied the said
drawings, specifications, or other data, is not to be regarded by implica-
tion or otherwise as in any manner licensing the holder or any other person
or corporation, or conveying any rights or permission to manufacture, use,
or sell any patented invention that may in any way be related thereto.

Qualified users may obtain copies of this report from the Defense
Documentation Center (DDC), Cameron Station, Bldg. 5, 5010 Duke Street,
Alexandria, Virginia.

Distribution of this report is restricted in accordance with the
US Export Act of 1949 as amended (DOD Directive 2030.4; AFR400-10) and it
should not be disseminated to OTS.

Copies of this report should not be returned to the Research and
Technology Division unless return is required by security considerations,
contractual obligations, or notice on a specific document.

FOREWORD

This report was prepared by the Electron Physics Laboratory, Department of Electrical Engineering, The University of Michigan, Ann Arbor, Michigan, under USAF Contract No. AF33(657)-11587 entitled "Solid-State Microwave Research". The secondary report number is Final Report under Project 06031.

The work was administered under the direction of the Electronic Technology Division, Air Force Avionics Laboratory. Captain Philip W. Cary was the project engineer.

This report covers work conducted from December 30, 1963 to April 15, 1965, and is authored by D. C. Hanson, J. E. King, J. E. Rowe and C. Yeh.

This report was submitted by the authors on April 20, 1965.

ABSTRACT

Phonon interactions in solids are investigated with particular
emphasis on the interaction of a phonon wave with a current in a semi-
conductor and on phonon-phonon interactions which can lead to parametric
interactions when the material is characterized by a nonlinear ω-β diagram.
The theory for such parametric amplifiers is outlined and experiments on
ruby and vanadium doped cadmium sulfide are outlined.

Plasma interactions in solids are studied by solving the Boltzmann
equation for a Fermi-Dirac distribution coupled with the Lorentz force
equation and Maxwell's equations for wave propagation in the solid. The
material characteristic is specified in terms of the energy vs. momentum
or wave number diagram. This study will permit the determination of
general criteria for instabilities in solids.

Studies on radiations from GaAs are outlined with particular
emphasis being given to the study of infrared radiation. A great deal of
experimental evidence is presented indicating radiation in the 4-40 micron
region. It is significant that the IR intensity increases linearly from
threshold to a current density of 800 amps/cm^2. The effect of contacts on
the operation is also discussed.

The gain and phase velocity equations are developed for acoustic-
wave interactions in solids including both the piezoelectric effect and
the deformation potential effect. Although materials like cadmium sulfide
and gallium arsenide are acceptable for low-frequency operation one must
utilize materials such as indium antimonide with high deformation potential
for microwave operation. A transducer program is outlined wherein emphasis
is placed on cadmium sulfide thin film transducers. Echo patterns are
shown and the measurement system is described in detail.

TABLE OF CONTENTS

LIST OF ILLUSTRATIONS

LIST OF TABLES

FINAL REPORT

FOR

SOLID-STATE MICROWAVE RESEARCH

<u>1</u>. <u>General</u> <u>Introduction</u>   (J. E. Rowe)

The purpose of this research study was to investigate the general

characteristics of high-frequency interactions in bulk semiconductor

materials. The general program was concerned with the generation, ampli-

fication and detection of coherent electromagnetic energy in the microwave,

infrared and optical regions of the electromagnetic spectrum.

The specific topics which have been under investigation are listed

below and discussed in detail in the following sections of this report.

a. Phonon interactions in solid-state materials.

b. Gunn effect studies.

c. Acoustic-wave interactions, including longitudinal and

shear mode excitations.

d. Solid-state plasma instabilities.

<u>2</u>. <u>Phonon</u> <u>Interaction</u> <u>in</u> <u>Solids</u>   (J. E. King)

<u>2.1</u> <u>Background</u>. In considering phonon interactions in solids

there are a number of possible effects which should be considered. One of

the first that comes to mind is the interaction of a phonon wave with a

current in a semiconductor. This gives rise to a traveling-wave phonon

amplification where energy is converted from the electron beam to the

phonon wave. This particular phenomena is being investigated widely and

is fairly well understood.

A second type of interaction to be considered is phonon-phonon

interaction. The particularly interesting aspect here concerns parametric

interactions which arise from a nonlinear ω-β diagram. The pump, signal,

1

and idler waves must satisfy the standard criteria for parametric inter-
action, namely,

$$\omega_i = \omega_p - \omega_s$$

and

$$\beta_i = \beta_p - \beta_s \quad , \tag{2.1}$$

where ω = radian frequency,

β = phase constant,

i = idler wave,

p = pump wave and

s = signal wave.

If these conditions are satisfied it is possible to obtain amplifi-
cation of the signal wave. There are two possible conditions which will
satisfy the above equations; one is the "forward" wave case where all
waves (signal, idler and pump) travel with group velocities in the same
direction, the second is a "backward" wave case where the signal wave has
a group velocity in the opposite direction to those of the pump and idler
waves. The characteristics of this interaction are beating-wave amplifi-
cation for the "backward" wave and exponential gain for the "forward" wave.

Another type of interaction that should be considered is phonon
paramagnetic resonance. This type of interaction is similar to electron
paramagnetic resonance which utilizes electromagnetic waves. The
characteristics of this type of interaction are an absorption of energy
from the phonon wave and a characteristic slowing of the wave due to
dispersion. This suggests that since the group velocity is changed, the
phase velocity ought also to change and this introduces a nonlinearity in

the ω-β diagram for the phonon waves. In addition this mechanism gives rise to the phonon maser.

From the brief discussion above it can be seen that it is possible to develop an amplifier which combines several of these interaction mechanisms. One particular device will be considered. It is a parametric phonon amplifier using paramagnetic resonance to obtain the nonlinear ω-β diagram.

2.2 Review of Theory. In order to understand the interaction mechanisms further, the fundamental theories will be reviewed below. To begin with consider the details of the parametric interaction theory. The first account of this was published by Tien[1] in 1958. In this article power gain, bandwidth and noise are discussed for electromagnetic waves propagating along one-dimensional transmission lines. An extension of this idea to distributed reactance systems was carried out by Breitzer and Sard[2]. Finally, Hsu[3] calculated the gain and noise figure for parametric interaction. The basic assumption made in these analyses is that of a periodically varying dielectric constant along the direction of propagation. The wave equation is then solved for a variation in dielectric constant

$$\epsilon = \epsilon_o \left[1 + \epsilon(z,t)\right] \ . \tag{2.2}$$

1. Tien, P. K., "Parametric Amplification and Frequency Mixing in Propagating Circuits", Jour. Appl. Phys., vol. 29, pp. 1347-1357; September, 1958.

2. Breitzer, D. I., Sard, E. W., "Low Frequency Prototype Backward-Wave Reactance Amplifier", Microwave Journal, vol. 2, pp. 34-37; August, 1959.

3. Hsu, H., "Analysis of Backward Traveling-Wave Parametric Amplifiers", General Electric Company, TIS, No. R60ELS-3; 1960.

The conditions of Eq. 2.1 which are typical for parametric interaction are obtained. In addition the power gain of the amplifier is calculated. For the "backward" mode the gain is

$$\text{Power gain} \propto \frac{1}{\cos^2 (kz)} \quad . \tag{2.3}$$

For the "forward" mode we obtain

$$\text{Power gain} \propto \cosh^2 (k_1 z) \quad . \tag{2.4}$$

The same analysis can be extended to include phonon waves since all the basic quantities, such as pressure, particle displacement and density, satisfy the wave equation providing that the interaction is small. This assumption depends on the perturbation of the density being small[*] which implies that the same analysis applies for one-dimensional phonon waves. The additional feature of phonon waves is that there is three-dimensional propagation and the propagation constants are in general anisotropic. In this analysis it is assumed that the density varies as a function of frequency and direction of propagation in the same way that the dielectric constant varies for reactance amplifiers. The above establishes the possibility of a traveling-wave parametric interaction providing a material can be found such that the parametric conditions of Eq. 2.1 are satisfied.

One possible way in which to introduce a nonlinearity in the ω-β diagram is to make use of acoustic paramagnetic absorption. Jacobsen and Stevens[4] calculated the ω-β diagram for simple spin systems. A typical

---

[*] See for example Morse, P. M., *Vibration and Sound*, McGraw-Hill, York, Pa., pp. 217-222; 1948.

4. Jacobsen, E. H., Stevens, K. W. H., "Interaction of Ultrasonic Waves with Electron Spins", *Physical Review*, vol. 129, pp. 2036-2044; March, 1963.

ω-β diagram is reproduced in Fig. 2.1 assuming no loss. Figure 2.2 shows the effect of loss on the ω-β diagram. The second figure is obtained as a generalization of the signal velocity changes observed by Shiren[5]. It is assumed that the group velocity and phase velocity form the usual Hilbert transform pair. Thus extrapolating the measurements made on the signal velocity, the curve for the phase velocity leads to an ω-β diagram of the type represented in Fig. 2.2. The size of the nonlinearity depends on the magnitude of the spin-phonon interaction.

The magnitude of the spin-phonon interaction is affected by the particular paramagnetic ion and also the type of crystal lattice. Investigations of spin-phonon interaction began in the early 1950's. However at that time the experimental investigations were limited to nuclear magnetic resonance because of the low frequency sound waves[6]. Since the advent of microwave ultrasonics in 1959, more investigations have been undertaken and most of these have been concerned with electron paramagnetic resonance. These investigations have been initiated in order to understand more about the spin-lattice relaxation time with regard to microwave electron paramagnetic resonance.

The theory of spin-phonon interaction was first worked out by Al'tshuler[7,8]. This paper deals primarily with low frequency (megacycle) phonon waves. Since 1959 a number of papers have been written concerning

6. Shutilov, V. A., "Stimulation of Ultrasonic Nuclear Magnetic Resonance, Review", Soviet Physics-Acoustics, vol. 8, pp. 303-319; April-June, 1963.

7. Al'tshuler, S. A., "Resonance Absorption of Ultrasound in Paramagnetic Salts", Soviet Physics-JETP, vol. 1, pp. 29-36; July, 1955.

8. Al'tshuler, S. A., "On the Theory of Electronic and Nuclear Paramagnetic Resonance Under the Action of Ultrasound", Soviet Physics-JETP, vol. 1, pp. 37-44; July, 1955.
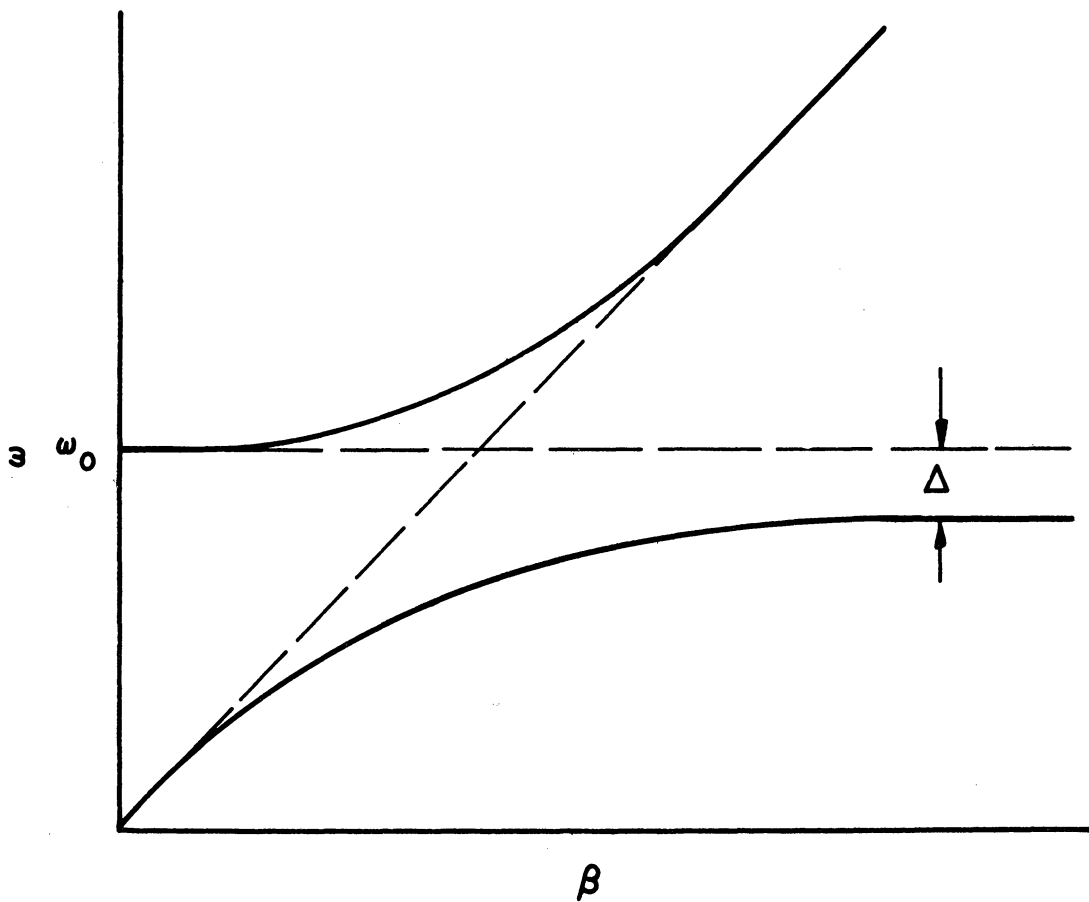
FIG. 2.1   DISPERSION RELATION BETWEEN ELASTIC WAVE FREQUENCY ω AND

PHASE CONSTANT β. Δ IS STOP BAND NEAR SPIN RESONANCE
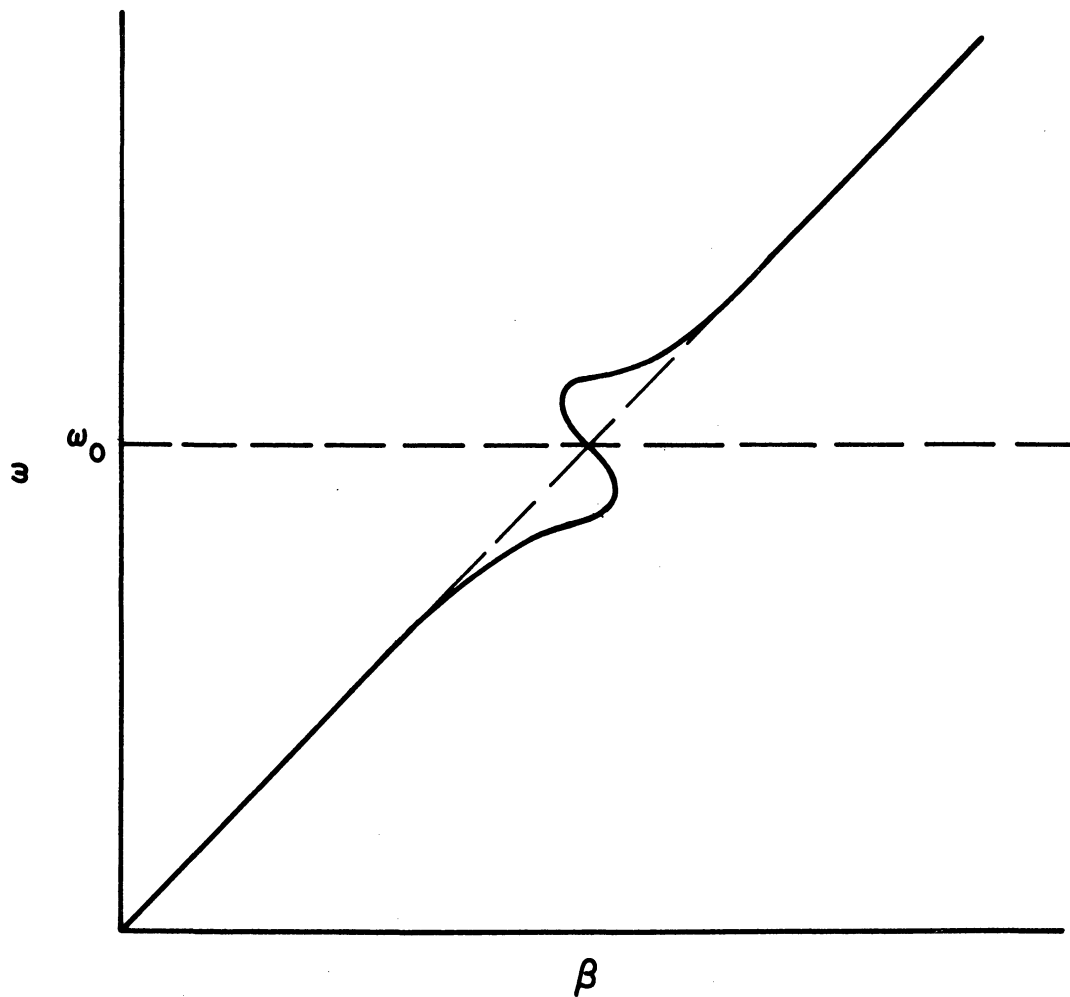
FREQUENCY ω.

FIG. 2.2 DISPERSION RELATION BETWEEN ELASTIC WAVE FREQUENCY ω AND

PHASE CONSTANT β WITH LOSS IN THE PARAMAGNETIC ABSORPTION

NEAR SPIN RESONANCE FREQUENCY ω.

the theory of spin-phonon interaction and the two most notable being one by Mattuck and Strandberg[9] and the other by Al'tshuler, Kochelaev, and Leushin[10]. These consider the recent advances in microwave ultrasonics. Mattuck and Strandberg develop the spin-phonon Hamiltonian. From this Hamiltonian the absorption coefficient can be worked out. Al'tshuler et al. have worked out the absorption coefficient for various paramagnetic ions in crystals[11].

It is possible to work out the ω-β diagram using their theory from the Hamiltonian as Jacobsen and Stevens[4] did. It is also possible to select crystals with various paramagnetic ions according to the magnitude of the spin-phonon absorption coefficient. In addition it is possible to determine the transition probabilities for spin-phonon interaction[12]. Using these transition probabilities it is possible to build a phonon maser. Tucker[13] used ruby to achieve phonon amplification.

9. Mattuck, R. D., Strandberg, M. W. P., "Spin-Phonon Interaction in Paramagnetic Crystals", Physical Review, vol. 119, pp. 1204-1217; August 15, 1960.

10. Al'tshuler, S. A., Kochelaev, B. I., Leushin, A. M., "Paramagnetic Absorption of Sound", Soviet Physics-USPEKHI, vol. 4, p. 880-903; May-June, 1962.

11. Al'tshuler, S. A., Bashkirov, Sh. Sh., Leushin, A. M., "Theory of the Acoustic Paramagnetic Resonance in Crystals Containing Ions of the Iron Group", Soviet Physics-Solid State, vol. 3, pp. 1088-1090; November, 1961.

12. Tucker, E. B., "Attenuation of Longitudinal Ultrasonic Vibrations by Spin-Phonon Coupling in Ruby", Physical Review Letters, vol. 6, pp. 183-185; February 15, 1961.

13. Tucker, E. B., "Amplification of 9.3 kmc/sec Ultrasonic Pulses by Maser Action in Ruby", Physical Review Letters, vol. 6, pp. 547-548; May 15, 1961.

2.3 Theory.

2.3.1 Parametric Conditions.

Let us consider a crystal lattice fixed in a coordinate system x,y,z in which we have traveling waves of frequency ω_p, ω_i, and ω_s for the pump, idler, and signal frequencies respectively. Now consider a second coordinate system x', y', z' moving with a velocity $\vec{v}$ with respect to x,y,z coordinates.

Recall from the Lorentz transformations of a plane wave, the frequencies convert as

$$\frac{\omega'}{\omega} = \frac{1 - v/c \cos \theta}{\sqrt{1 - (v/c)^2}} \quad . \tag{2.5}$$

Now considering the case where $v \ll c$

$$\omega' = \omega - \frac{v\omega}{c} \cos \theta \quad . \tag{2.6}$$

Recall that $\beta = \omega/c$, the phase constant, and $ab \cos \theta = \vec{a} \cdot \vec{b}$, thus

$$\omega' = \omega - \vec{v} \cdot \vec{\beta} \quad . \tag{2.7}$$

One now has the relations for the Doppler frequency in the moving coordinate system. They are

$$\omega'_p = \omega_p - \vec{v} \cdot \vec{\beta}_p \quad ,$$

$$\omega'_i = \omega_i - \vec{v} \cdot \vec{\beta}_i$$

and

$$\omega'_s = \omega_s - \vec{v} \cdot \vec{\beta}_s \quad . \tag{2.8}$$

Parametric interaction becomes possible when the pump frequency is equal to the signal plus idling frequencies in any moving coordinate system. Thus

$$\omega_p = \omega_s + \omega_i \tag{2.9}$$

and

$$\omega_p' = \omega_s' + \omega_i' \ . \tag{2.10}$$

Substituting the relations for the moving coordinate system into Eq. 2.6 gives

$$\vec{v} \cdot \vec{\beta}_p = \vec{v} \cdot \vec{\beta}_i + \vec{v} \cdot \vec{\beta}_s \ . \tag{2.11}$$

If all waves have the same velocity then for the forward wave

$$\vec{\beta}_p = \vec{\beta}_i + \vec{\beta}_s \ . \tag{2.12a}$$

If the signal wave has an oppositely directed group velocity then for the backward wave

$$\vec{\beta}_p = \vec{\beta}_i - \vec{\beta}_s \ . \tag{2.12b}$$

Thus Eqs. 2.9 and 2.12 are the conditions to be satisfied for traveling-wave parametric interaction. If Eqs. 2.9 and 2.12 are multiplied by $\hbar$ (Planck's constant/2π) the following is obtained:

$$\hbar \, \omega_p = \hbar \, \omega_s + \hbar \, \omega_i \ , \tag{2.13}$$

$$\hbar \, \vec{\beta}_p = \hbar \, \vec{\beta}_i + \hbar \, \vec{\beta}_s \tag{2.14a}$$

or

$$\hbar \, \vec{\beta}_p = \hbar \, \vec{\beta}_i - \hbar \, \vec{\beta}_s \ . \tag{2.14b}$$

These equations represent the conservation of energy (Eq. 2.13) and momentum (Eq. 2.14).

2.3.2 Interaction of Traveling Waves.

The following development applies to either phonon waves or to electromagnetic waves. For phonon waves, one has the wave equation

$$\nabla^2 \xi - k \frac{\partial^2}{\partial t^2} (\rho \xi) = 0 \;, \tag{2.15}$$

where ξ = displacement,

ρ = mass density,

$k = 1/P_o \gamma_c$,

P_o = equilibrium pressure and $\gamma_c = C_p/C_v$ the ratio of specific heats.

ρ is allowed to be time dependent since ρ is to vary with the pump wave. For electromagnetic waves

$$\nabla^2 E - \mu_o \frac{\partial^2}{\partial t^2} (\epsilon E) = 0 \;, \tag{2.16}$$

where E = electric field,

μ_o = permeability and

ϵ = dielectric constant.

In the above two wave equations a homogeneous and continuous media has been assumed. The density and dielectric constant are assumed to be time dependent, being perturbed by the pump wave. It is further assumed that the signal, pump and idler waves are all plane waves. For phonon waves it is assumed that the attenuation constant is zero and that the lattice is perfect with no dislocations or imperfections. It is also assumed that the lattice is at a low temperature so that the number of thermal phonons is negligible at the frequencies of interest. In the case of the electromagnetic waves the space charge and conductivity of the medium are

11

considered to be negligible. Thus one sees that the two wave equations are basically the same and a solution to either one is a representative solution of both. Note though that the assumptions are much more restrictive for the phonon wave than for the electromagnetic wave. This is mainly because isotropic perfect crystals with zero attenuation constant are hard to find. As a result of the similarity of the two equations, only a solution for the electromagnetic wave equation will be developed.

The dielectric constant will be assumed to be perturbed by the traveling wave at the pump frequency. Thus the dielectric constant can be written as

$$\epsilon = \epsilon_o [1 + \zeta \cos (\omega_p t - \vec{\beta}_p \cdot \vec{\gamma})] \; , \qquad (2.17)$$

with the pump wave traveling with a phase constant $\vec{\beta}_p$ in the direction $\vec{\gamma}$, the general coordinate vector given by

$$\vec{\gamma} = x \; \hat{i} + y \; \hat{j} + z \; \hat{k} \; .$$

Thus if the pump wave was propagating in the z-direction

$$\vec{\beta}_p \cdot \vec{\gamma} = \beta_{p_z} z \; .$$

A solution to the wave equation is assumed whose coefficients are functions of z but not of t. Then

$$E = A_1 (z) \; e^{j(\omega_1 t - \beta_1 z)} + A_2 (z) \; e^{j(\omega_2 t - \beta_2 z)}$$

$$+ B_1 (z) \; e^{-j(\omega_1 t - \beta_1 z)} + B_2 (z) \; e^{-j(\omega_2 t - \beta_2 z)} \; . \qquad (2.18)$$

ω_1 and ω_2 represent the signal and idling frequencies.

The wave equation is given by Eq. 2.16 and the dielectric constant can be expanded as

$$\epsilon = \epsilon_0 \left\{ 1 + \frac{\zeta}{2} \left[e^{j(\omega t - \beta z)} + e^{-j(\omega t - \beta z)} \right] \right\} , \qquad (2.19)$$

where

$$\omega = \omega_1 - \omega_2 ,$$

$$\beta = \beta_1 - \beta_2 . \qquad (2.20)$$

Substituting the assumed solution and the expression for the dielectric constant into the wave Eq. 2.16 and noting that $\beta^2 = \omega^2 \mu_0 \epsilon$, the following equation results:

$$e^{j(\omega_1 t - \beta_1 z)} \left[\frac{\partial^2 A_1}{\partial z^2} - j2\beta_1 \frac{\partial A_1}{\partial z} + \frac{\zeta}{2} A_2 \beta_1^2 \right]$$

$$+ e^{j(\omega_2 t - \beta_2 z)} \left[\frac{\partial^2 A_2}{\partial z^2} - j2\beta_2 \frac{\partial A_2}{\partial z} + \frac{\zeta}{2} A_1 \beta_2^2 \right]$$

$$+ e^{-j(\omega_1 t - \beta_1 z)} \left[\frac{\partial^2 B_1}{\partial z^2} + j2\beta_1 \frac{\partial B_1}{\partial z} + \frac{\zeta}{2} B_2 \beta_1^2 \right]$$

$$+ e^{-j(\omega_2 - \beta_2 z)} \left[\frac{\partial^2 B_2}{\partial z^2} + j2\beta_2 \frac{\partial B_2}{\partial z} + \frac{\zeta}{2} B_1 \beta_2^2 \right] = 0 . \qquad (2.21)$$

Note that A_1 and A_2 are coupled by ζ as are B_1 and B_2. For the equation to be satisfied independent of time and distance each term must be individually zero. If in addition the A's and B's are assumed to be slowly varying functions of z, then the second derivatives can be

considered small with respect to the term $\beta \, \partial/\partial z$. As a result two sets of first-order equations arise.

$$\frac{\partial A_1}{\partial z} = -j \frac{\zeta}{4} \beta_1 A_2 \quad ,$$

$$\frac{\partial A_2}{\partial z} = -j \frac{\zeta}{4} \beta_2 A_1 \qquad\qquad (2.22)$$

and

$$\frac{\partial B_1}{\partial z} = +j \frac{\zeta}{4} \beta_1 B_2 \quad ,$$

$$\frac{\partial B_2}{\partial z} = +j \frac{\zeta}{4} \beta_2 B_1 \quad . \qquad\qquad (2.23)$$

The solution of Eq. 2.22 for β_1, $\beta_2 > 0$ is

$$A_1 = a_1 e^{j\alpha z} + b_1 e^{-j\alpha z} \quad ,$$

$$A_2 = - \sqrt{\beta_2/\beta_1} \, [a_1 e^{j\alpha z} - b_1 e^{-j\alpha z}] \quad , \qquad\qquad (2.24)$$

where $\alpha = \sqrt{\zeta^2 \beta_1 \beta_2/16} = \zeta \sqrt{\beta_1 \beta_2}/4$. The solution of Eq. 2.23 is

$$B_1 = a_2 e^{j\alpha z} + b_2 e^{-j\alpha z} \quad ,$$

$$B_2 = \sqrt{\beta_2/\beta_1} \, [a_2 e^{j\alpha z} - b_2 e^{-j\alpha z}] \quad . \qquad\qquad (2.25)$$

Recall A_2 and B_2 are the coefficients for the wave at frequency ω_2 and A_1 and B_1 are the coefficients for the wave at frequency ω_1. The boundary conditions imposed are that a signal and a pump wave are applied at the input. It is assumed that the signal is in phase at the input. The idler

14

will be assumed to have a zero initial amplitude. Consequently the coefficients are such that

$$a_1 = b_1$$

and

$$a_2 = b_2 \quad ,$$

in order to assure that the idler has zero amplitude at the origin. If the signal has amplitude E_o at the origin then

$$a_1 = b_1 = a_2 = b_2 = \frac{E_o}{4} \quad . \qquad (2.26)$$

Combining this result with Eqs. 2.24 and 2.25 and substituting into Eq. 2.18, the assumed solution for E becomes

$$E = E_o \cos \alpha z \cos (\omega_1 t - \beta_1 z) + E_o \sqrt{\beta_2/\beta_1} \sin \alpha z \sin (\omega_2 t - \beta_2 z) \quad .$$

$$(2.27)$$

Substituting $\alpha = \zeta \sqrt{\beta_1 \beta_2}/4$ yields

$$E = E_o \cos \zeta z \sqrt{\beta_1 \beta_2}/4 \cos (\omega_1 t - \beta_1 z)$$

$$+ E_o \sqrt{\beta_2/\beta_1} \sin \zeta z \sqrt{\beta_1 \beta_2}/4 \sin (\omega_2 t - \beta_2 z) \quad . \quad (2.28)$$

Now recall that $\omega = \omega_1 - \omega_2$ and $\beta = \beta_1 - \beta_2$.

    If one lets

$$\omega_p = \omega$$

$$\beta_p = \beta$$

$$\omega_1 = \omega_s$$

$$\beta_1 = \beta_s$$

and

$$\omega_2 = -\omega_i$$

$$\beta_2 = -\beta_i \qquad (2.29)$$

for the forward wave, then

$$\omega_p = \omega_s + \omega_i \quad ,$$

$$\beta_p = \beta_s + \beta_i \quad . \qquad (2.30)$$

Making these substitutions in Eq. 2.28 and using the fact that $\cos j\,\theta = \cosh \theta$ and $\sin j\,\theta = j \sinh \theta$, gives

$$E = E_o \cosh \left(\frac{\zeta z}{4} \sqrt{\beta_s(\beta_p - \beta_s)} \right) \cos (\omega_s t - \beta_s z)$$

$$+ E_o \sqrt{(\beta_p - \beta_s)/\beta_s} \; \sinh \left(\frac{\zeta z}{4} \sqrt{\beta_s(\beta_p - \beta_s)} \right) \sin (\omega_i t - \beta_i z) \quad . \quad (2.31)$$

This is the expression for field as a function of z and t for the signal and idler waves where both are in the forward direction. For backward waves $\beta_s < 0$ and $B_1 = -|\beta_s|$ is substituted in Eq. 2.29. Then

16

$$\omega_p = \omega_s + \omega_i \quad ,$$

$$\beta_p = -|\beta_s| + \beta_i \quad . \tag{2.32}$$

Substituting in Eq. 2.28 for the backward wave field gives

$$E = E_o \cos \frac{\zeta z}{4} \sqrt{|\beta_s| \, (\beta_p + |\beta_s|)} \cos (\omega_s t + |\beta_s| z)$$

$$- E_o \sqrt{(\beta_p + |\beta_s|)/|\beta_s|} \, \sin \frac{\zeta z}{4} \sqrt{|\beta_s| \, (\beta_p + |\beta_s|)} \sin (\omega_i t - \beta_i z) \quad .$$

$$\tag{2.33}$$

This represents the electric field as a function of z and t for the signal and idler waves, the first term for the signal and the second for the idler. Note that the major difference between Eqs. 2.31 and 2.33 is their dependence on ζ. In Eq. 2.31 for the forward wave there is exponential dependence and in Eq. 2.33 for the backward wave there is a beating-wave effect wherein energy is transferred between the idler and signal waves as a function of distance.

The power associated with the signal wave is proportional to the time average field squared.

For the forward signal wave the time average output field at position z is given by

$$E_s = \frac{E_o}{2} \cosh \frac{\zeta z}{4} \sqrt{\beta_s \, (\beta_p - \beta_s)} \quad .$$

The input signal wave is just $E_o/2$ so that the power gain is proportional to

$$P_s \propto \cosh^2 \frac{\zeta z}{4} \sqrt{\beta_s \, (\beta_p - \beta_s)} \quad . \tag{2.34}$$

For the backward wave, consider that the signal input is at $z = z_o$.
Then the input signal is given by

$$E_s = \frac{E_o}{2} \cos \frac{\zeta z_o}{4} \sqrt{|\beta_s| (\beta_p + |\beta_s|)} \ .$$

The output is at $z = 0$ and is just $E_o/2$ so that the power output is
proportional to

$$P_s \ \alpha \ \frac{1}{\cos^2 \frac{\zeta z_o}{4} \sqrt{|\beta_s| (\beta_p + |\beta_s|)}} \ . \tag{2.35}$$

Therefore if the modulation parameter ζ is adjusted so that the argument of
the cosine is nearly $\pi/2$, the denominator will be quite small giving a
sizable gain.

2.3.3 <u>Phonon Paramagnetic Resonance</u>. The method of obtaining
information about the spin-phonon interaction is to start with the total
Hamiltonian for the crystal. This Hamiltonian includes terms which
account for spin-spin interaction, lattice energy, free ion energy, and
orbital coupling. The Hamiltonian can then be written as

$$\mathsf{H} = \mathsf{H}_L + \mathsf{H}_o + V + 2\beta \vec{S} \cdot \vec{H} + \lambda \vec{L} \cdot \vec{S} + \beta \vec{L} \cdot \vec{H} \ , \tag{2.36}$$

where β is the Bohr magneton,

λ is the spin-orbit coupling parameter,

$\vec{S}$ and $\vec{L}$ are the spin and orbital angular moments of the paramagnetic ion,

$\vec{H}$ is the external d-c magnetic field,

V is the energy of the ion due to the crystalline electric field,

H_o is the energy of the free ion and

H_L represents the lattice energy.

18

Under the assumption of harmonic forces between atoms in the crystal, the lattice Hamiltonian becomes

$$H_L = \sum_{\rho} \hbar \omega_\rho \left(a_\rho^+ a_\rho + \frac{1}{2} \right) , \qquad (2.37)$$

where a_ρ^+ and a_ρ are the phonon creation and annihilation operators. They have the properties that

$$a_\rho^+ \mid \ldots \eta_\rho \ldots > = (\eta_\rho + 1)^{1/2} \mid \ldots \eta_\rho + 1 \ldots >$$

$$a_\rho \mid \ldots \eta_\rho \ldots > = \eta_\rho^{1/2} \mid \ldots \eta_\rho - 1 \ldots > , \qquad (2.38)$$

where η_ρ is the ρth eigenvalue.

After a number of complicated perturbation calculations a spin-phonon interaction Hamiltonian can be calculated for direct interaction between phonons and spin. The following equivalent Hamiltonian involving spin and phonon operators results[14]:

$$H_{sp} = \sum_{\substack{\rho,f \\ i \geq j}} A^{f\rho} P_\rho [h\nu \, b_i^f (\lambda S_i) - b_{ii}^f \{ \lambda^2 S_i S_i + \lambda\beta (S_i H_i + H_i S_i) \}$$

$$+ b_{ij}^f \{ \lambda^2 (S_i S_j + S_j S_i) + \lambda\beta (S_i H_j + H_i S_j + S_j H_i + H_j S_i) \}] , \quad (2.39)$$

where b_i^f and b_{ij}^f represent coupling parameters between orbital levels through the orbital angular momentum L and the perturbation of the crystalline electric field.

---

14. Mattuck, R. D., Strandberg, M. W. P., loc. cit., p. 1208.

A_ρ^f represents the amplitudes associated with the normal modes of vibration of the lattice and P_ρ is the creation and annihilation operator = $a_\rho^+ + a_\rho$. This equation represents a multipole expansion of the interaction in terms of the spin operators. The terms linear in S_i are the dipolar terms, with those quadratic in S_i being quadrapolar.

Using this interaction Hamiltonian it is possible to calculate matrix elements which will yield the absorption coefficient of spin-phonon interaction between two spin states i and j. Before doing this the Hamiltonian can be simplified under certain cases. The first simplification distinguishes between when the total effective spin quantum number $S' = 1/2$ or when $S' > 1/2$.

Case I. $S' = 1/2$.

When $S' = 1/2$ one has what is termed a Kramer's Doublet. The two energy levels are then split uniformly by the Zeeman interaction. The terms linear in S_i are the dipolar expansion and should be the largest. The S_iS_j terms stimulate transitions of 0 or ±2 in quantum number, since the S_i operators operate 0 or ±1, and the term $(S_iS_z + S_zS_i)$ exactly cancels. The terms remaining are then linear in S_i since the S_iS_i terms also give 0 or ±2 transitions. Note with two levels a change of ±2 is not allowed. The result is then

$$H_{sp} = \sum_{\substack{\rho,f \\ i \geq j}} A^{f\rho} P_\rho [h\lambda \, b_i^f \, \lambda S_i - b_{ii}^f \, \lambda\beta \, (S_iH_i + H_iS_i)$$

$$+ b_{ij}^f \, \lambda_\rho(S_iH_j + H_iS_j + S_jH_i + H_jS_i)] \quad . \quad (2.40)$$

Take Eq. 2.36 and make the following substitutions:

1. $\vec{H} = H_z$,

2. $h\nu = E_k - E_{k'} = g_{kk'}\beta H$,

3. The phonon wave is an x-directed longitudinal wave and

4. Define $\hbar\epsilon = \sum_f B_f \lambda\beta H_z (g_{kk'} b_x^f + b_{zx}^f)$.

It is then possible to reduce the interaction Hamiltonian to

$$H_{sp} = \hbar\epsilon (U_{n+1} - U_{n-1}) S_x^n , \qquad (2.41)$$

where n represents the paramagnetic ion at location n in the lattice.

Equation 2.37 is exactly the same interaction Hamiltonian used by Jacobsen and Stevens[15] in the derivation of the dispersion relation for S' = 1/2.

Case II. S' > 1/2.

For this case, some terms can be dropped on the basis of their small size. In general $\lambda \gg \beta H$ and $h\nu$ so that only terms proportional to λ^2 will contribute. This leaves

$$H_{sp} = \sum_{\substack{\rho,f \\ i \geq j}} A^{f\rho} P_\rho [b_{ii}^f \lambda^2 S_i S_i + b_{ij}^f \lambda^2 (S_i S_j + S_j S_i)] . \qquad (2.42)$$

Using this form it is possible to generate the terms that Al'tshuler, Kochelaev and Leushin[16] use in calculating the absorption coefficients for various paramagnetic ions. The procedure is to calculate the matrix elements between various levels. In addition this form can be simplified in particular cases to simple interaction Hamiltonians. For S' = 1 this can be simplified to the result used by Jacobsen and Stevens.

---

15. Loc. cit.

16. Loc. cit.

2.3.4 <u>Theoretical Conclusions</u>. Using the spin-phonon Hamiltonian, Al'tshuler, Kochelaev, and Leushin[17] have calculated the coefficients of sound absorption. These are summarized in the tables below.

Table 2.1

Coefficients of Sound Absorption for Ions with

$$S' = 1/2. \quad \sigma = A \frac{\nu^4}{T} \times 10^{-40} \text{ cm}^{-1}$$

Configuration and term of ion		Spin	Ion	A
d^1	^2D	$S' = S = 1/2$	Ti^{3+}	10^4
d^7	^4F	$S' = 1/2 \quad S = 3/2$	Co^{2+}	10^2
d^9	^2D	$S' = S = 1/2$	Cu^{2+}	1

where S = spin of free ion, S' is effective spin of lattice site.

Table 2.2

Coefficients of Sound Absorption for Ions with

$$S' > 1/2. \quad \sigma = A \frac{\nu^2}{T} \times 10^{-19} \text{ cm}^{-1}$$

Configuration and term of ion		Spin	Ion		A
d^2	^3F	1	V^{3+}		10^6
d^3	^4F	$3/2$	Cr^{3+}	V^{2+}	1
d^4	^5D	2	Cr^{2+}	Mn^{3+}	10^5
d^6	^5D	2	Fe^{2+}		10^6
d^8	^3F	1	Ni^{2+}		10^3

---

17. Loc. cit.

Table 2.3

Coefficients of Absorption of Longitudinal Sound Waves in

Ethylsulfates of Rare-Earth Ions with an Even Number of Electrons.

$$\sigma = A \frac{\nu^2}{T} \times 10^{-13} \text{ cm}^{-1}$$

Ion	No. of Doublet	Interval Between Doublet and Ground State (in cm^{-1})	A	Ion	No. of Doublet	Interval Between Doublet and Ground State (in cm^{-1})	A
Pr^{3+}	1	0	1.7	Ho^{3+}	1	4	7.3
	2	170	8.8		2	47	15.8
	3	212	1.7		3	60	150.1
Eu^{3+}	1	270	800.7		4	139	0
Tb^{3+}	1	7	3.7		5	141	1.5
	2	24	10.9		6	197	150.1
	3	26	60.8	Tm^{3+}	1	14	5.6
	4	50	10.5		2	26	12.0
					3	98	49.4
					4	129	13.4

Table 2.4

Coefficients of Absorption of Sound. Rare-Earth Ions

with Odd Number of Electrons. $\sigma = A \frac{\nu^4}{T} \times 10^{-40} \text{ cm}^{-1}$

Ion	A
Nd^{3+}	600
Ce^{3+}	10^6

Based on this calculated data, the absorption coefficients will be compared for various ions. Assume $v = 10^9 = 1$ Gc, then

$$\sigma_{Ti^{3+}} = 1/T \; , \qquad \sigma_{V^{3+}} = 10^5/T \; ,$$

$$\sigma_{Cr^{3+}} = 1/10T \; , \qquad \sigma_{Pr^{3+}} = 1.7 \times 10^5/T \; ,$$

$$\sigma_{Fe^{2+}} = 10^5/T \; , \qquad \sigma_{Ce^{3+}} = 100/T \; .$$

Note in general that the rare-earth ions have the largest absorption coefficient. This is due to the fact that for rare-earth ions, the outer electrons shield the ion from changes in crystalline field so that it is more sensitive to orbital changes. Note also that Cr^{3+} corresponds to the configuration found in ruby and that it has the smallest absorption coefficient. The even electron configurations also have large coefficients.

Based on this data it is possible to select a material for high absorption coefficient. It appears that semiconductors can provide a suitable host lattice for some of these ions and in particular the rare-earth ions. In addition there is the possibility that these levels will be unequally spaced because of lattice distortions. This means that it might be possible to use these crystals for a phonon maser.

The absorption coefficients all contain frequency to some power in the numerator and temperature in the denominator. Thus in order to increase the absorption coefficient the frequency must be increased and the temperature lowered. However by increasing the frequency the attenuation constant of the material increases[18]. Thus a compromise between increasing σ and α must be reached.

---

18. Tannenwald, P. E., "Microwave Ultrasonics", Microwave Journal, vol. VI, pp. 61-65; December, 1963.

It is interesting to note that although ruby has the lowest absorption coefficient it has been the material most often used experimentally. The phonon maser was demonstrated using ruby. However, Shiren[19] used Ni^{2+} and Fe^{2+} and noted that the absorption for Fe^{2+} was larger than that for Ni^{2+} as is predicted by Table 2.2. Shiren also noted about a 20 percent slowing of the signal velocity for Fe^{2+} and only about five percent for Ni^{2+} which would also be predicted by the absorption coefficients.

This amount of change in the signal velocity should result in a significant change in the phase velocity. These quantities are related by the normal dispersion relation so that a sizable change in the phase constant is expected. This will result in an ω-β diagram similar to that of Fig. 2.2.

2.4 Review of Relating Experiments.

2.4.1 Review of Electron Paramagnetic Experiments. From

Table 2.2, the absorption coefficients for the configurations with an even number of electrons is seen to be much higher than for the configurations with an odd number of electrons. This could have been anticipated from the general results of electron paramagnetic resonance where the even configurations have a very short spin-lattice relaxation time, implying a strong coupling between the lattice and the spin of the electrons. It is because of this extremely short relaxation time that very little is known about the paramagnetic resonance spectra for the even electron configurations.

At present the even configurations have been examined mainly in cubic crystals where the spin Hamiltonian is much simpler. The original

---

19. Loc. cit.

experimental work in this area was done by Low[20] on $Ni^{2+}(3d^8)$ and

$Fe^{2+}(3d^6)$ in MgO. Fe^{2+} was also investigated in cubic ZnS but the spectra could not be interpreted.

For the $Ni^{2+}(3d^8)$ in MgO, one broad line at g = 2.23 was found. This again was substantiated by Walsh[21]. The linewidth is very large indicating a large dipole-dipole interaction. For $Fe^{2+}(3d^6)$ in MgO, three lines are observed--a very narrow and a very broad line at g = 3.427 and a line with high-field cutoff at g = 6.33. The high g line is due to a forbidden transition $\Delta M = \pm 2$ and the high field cutoff is attributed to an asymmetrical distribution of strains. These lines were only observable at liquid helium temperature (4.2°K) indicating an extremely short spin-lattice relaxation time. Recently the same type of spectra for $Fe^{2+}(3d^6)$ has been observed in CaO^{22}.

No results have been obtained on the $3d^4$ configuration although several people have been investigating the effect of electron trapping by $C_r^{2+}(3d^4)$ to become $C_r^+(3d^5)$ in ZnS^{23}. The trappling occurs under stimulation by 365mμ light. It is very probable that the relaxation time is so short that electron paramagnetic resonance is not observed. This effect also has been observed in ZnSe and $ZnTe^{24}$.

20. Low, W., "The Paramagnetic Resonance and Optical Spectra of Some Ions in Cubic Crystalline Fields", Annals of the New York Academy of Sciences, vol. 72, Article 2, pp. 69-126; March 17, 1958.

21. Walsh, W. M., "Effects of Hydrostatic Pressure on the Paramagnetic Spectra of Several Iron Group Ions in Cubic Crystals", Physical Review, vol. 122, pp. 762-771; May 1, 1961.

22. Shuskus, A. J., "Paramagnetic Resonance of Divalent Iron in Calcium Oxide", Jour. Chem. Phys., vol. 46, pp. 1602-1604; March 15, 1964.

23. Kallmann, H., "Progress Report 20 on Paramagnetic Resonance in the Solid State", New York University; August, 1963.

24. Title, R. S., "Paramagnetic-Resonance Spectra of the $3d^5$ Configuration of Chromium in ZnSe and ZnTe", Physical Review, vol. 133, pp. A1613-A1616; March 16, 1964.

The $3d^2$ configuration of V^{3+} has been investigated in several substances. It has been observed in ZnS and ZnTe cubic crystals and CdS which is hexagonal crystal. Strain broadened transitions were observed for the $\Delta M = \pm 1$ transition and a rather sharp line for the forbidden transition $\Delta M = \pm 2$ was observed for V^{3+} in ZnS[25]. These transitions were observed at $1.3°K$ indicating possible short relaxation times. The $3d^2$ configuration has also been observed in hexagonal CdS[26].

2.4.2 Review of Ultrasonic Spin Resonance. The work of Browne and Dobrov[27,28] using ruby is very interesting as they have correlated phonon absorption and spin lattice relaxation times. In addition they have obtained several absorption curves using their spectrometer. This instrument is designed to integrate pulses and to display this as an absorption signal. In this manner they obtain the absorption line shape where in electron paramagnetic resonance the derivative of the absorption curve is normally displayed.

25. Holton, W. C., Schneider, J., Estle, T. L., "Electron Paramagnetic Resonance of Photosensitive Iron Transition Group Impurities in ZnS and ZnO", Physical Review, vol. 133, pp. A1638-A1641; March 16, 1964.

26. Ludwig, G. N., Woodbury, H. H., "Electron Spin Resonance in Semi-conductors", Solid State Physics, Academic Press, New York, vol. 13, p. 299; 1962.

27. Browne, M. E. Dobrov, W. I., "Magnetic Resonance Absorption of Hypersonic Waves in Paramagnetic Crystals", Jour. of the Phys. Soc. of Japan, vol. 17, Supplement B-I, pp. 469-471; 1962.

28. Dobrov, W. I., Browne, M. E., "Low Temperature Relaxation in Ruby from Microwave Acoustic Measurement", Paramagnetic Resonance, Academic Press, New York, pp. 447-455; 1963.

Shiren's[29],[30] work shows excellent agreement between ultrasonic

measurements and static stress measurements for the fourth rank

spin-phonon coupling tensor G. Using this data he is able to calculate

relaxation times in reasonable agreement with measured values.

2.4.3 <u>Nonlinear</u> <u>Acoustic</u> <u>Interaction</u> <u>and</u> <u>Parametric</u>

<u>Amplification</u>. Two important articles by Shiren[31],[32] have appeared in

the literature. In the first of these, he reports a strong nonlinear

interaction which is characterized by an increased absorption of the

signal. This absorption is power dependent and can result in as much as

an increase of 65 to 70 percent in the absorption. This nonlinear effect

is the result of anharmonic restoring forces between adjacent atoms.

Shiren showed that the nonlinear effect was not due to impurities in the

crystal but only due to the anharmonic restoring forces. He attributed

the interaction to a three-phonon process, i.e., a signal, a pump and an

idler. For the nonlinear effect to occur the waves must satisfy the

following parametric equations:

$$\omega_p = \omega_s + \omega_i \ ,$$

$$\beta_p = \beta_s + \beta_i \ . \tag{2.43}$$

29. Shiren, N. S., "Comparison of Ultrasonic Spin Resonance Measurements with Paramagnetic Relaxation Theory", <u>Proc.</u> <u>of</u> <u>the</u> <u>Internat'l.</u> <u>Conference</u> <u>on</u> <u>Magnetic</u> <u>and</u> <u>Electronic</u> <u>Resonance</u> <u>and</u> <u>Relaxation</u>, Eindhoven, Holland, pp. 114-122; 1962.

30. Shiren, N. S., "Dipolar Broadening from Pulse Velocity in Ultrasonic Spin Resonance", <u>Paramagnetic</u> <u>Resonance</u>, Academic Press, New York, pp. 482-485; 1963.

31. Shiren, N. S., "Nonlinear Acoustic Interaction in MgO at 9 Gc/sec", <u>Physical</u> <u>Review</u> <u>Letters</u>, vol. 11, No. 1, pp. 3-6; July 1, 1963.

32. Shiren, N. S., "Ultrasonic Traveling-Wave Parametic Amplification in MgO[1]", <u>Appl.</u> <u>Phys.</u> <u>Letters</u>, vol. 4, No. 4, pp. 82-85; February 15, 1964.

Thus by using phonon paramagnetic resonance Shiren was able to mismatch the phase constants so that

$$\beta_p \neq \beta_s + \beta_i$$

and thus eliminate the nonlinear interaction. The mechanism for doing this is the same as outlined in an earlier section. The phonon paramagnetic resonance introduces a slowing of the group velocity and also a change in the phase velocity as the frequency of the phonon wave passes through a resonance. Consequently it is possible to mismatch the phase constants by tuning the resonance to one of the frequencies involved.

There was no observed change in nonlinear effect over a temperature range from $1.6°K$ to $4.2°K$. The nonlinearity was also not affected by the concentration of impurities. This further substantiates the belief that it is a property of the lattice and not of the paramagnetic ions.

In the second paper Shiren reports gain due to parametric amplification. He achieved gain by tuning the phonon paramagnetic resonance to simultaneously mismatch the pump plus signal frequency and twice the pump frequency which was made possible since the sample contained two different impurities, nickel and iron. These ions have different g-values and so split at different rates in a magnetic field. The crystal MgO is cubic so that there is no zero field splitting and thus, by correct choice of frequencies, it is possible to have the s + p and 2p frequencies resonant at the same magnetic field in the two different spin systems.

These two papers offer experimental evidence for traveling-wave parametric amplification of acoustic waves. One of the difficulties of Shiren's techniques is that the ω-β diagram is linear out to the frequency s + p. This means that any frequencies less than the pump frequency will satisfy the parametric interaction conditions. Thus it would seem possible

that a large part of the nonlinear interaction is wasted in "noise" caused by all other undesired frequencies. Gain is thus achieved for only those modes in which the upper side band is tuned out, thus converting additional power into the signal frequencies. Because of this the system proposed earlier should be considerably better. By using several tunable resonances it would be possible to eliminate the upper side band and, in addition, to have the parametric conditions satisfied for only the particular pump and signal frequencies. This would allow considerably more power to be transferred into the signal frequency.

A second difficulty is that by using a cubic crystal there is little tuning of the energy levels since they split linearly with magnetic field. Also because of the requirements of eliminating higher harmonics of the pump and signal frequencies it is desirable to have both resonances at the same magnetic field value. This requirement fixes the frequency ratio for pump and signal in a cubic crystal since two separate spin systems are required, each with its own g-value. In a noncubic crystal such as cadmium sulfide, this problem is eliminated since the energy levels vary with angle from the c-axis. Thus it would appear possible to satisfy the simultaneous resonance condition for perhaps several different signal frequencies.

An interesting article concerning nonlinear acoustic effects in CdS was written by Nill[33] who points out several interesting effects associated with piezoelectric semiconductors such as CdS. Phonon-phonon nonlinear effects are not only due to anharmonic lattice effects, but can also be caused by bunching of the electrons by the high-power acoustic-wave interactions through the piezoelectric constant. This causes interaction with a second acoustic wave of different frequency in the usual parametric sense.

---

33. Nill, K. W., "Piezoelectric Coupling Between Ultrasonic Waves and Free Electrons in Cadmium Sulfide", Tech. Report 181, Laboratory for Insulation Research, Massachusetts Institute of Technology, ASTIA No. AD 414 853; July, 1963.

This particular effect should be important for parametric amplification in CdS:V. This means that, as Nill points out, there is an observable phonon-phonon scattering. This interaction is a consequence of the nonhomogeneous elastic constant resulting from the presence of space charge and takes place with perfectly harmonic lattice forces. For photoconducting CdS, it is possible to alter the space charge by changing light intensity. This means that it might be possible to control the nonlinear phonon-phonon interaction with light.

The second conclusion is that it is possible to achieve nonlinear interactions even with harmonic lattice forces. This means that the proposed parametric amplifier should work and be considerably better than the effects reported by Shiren[34].

2.5 <u>Material Selection</u>. There are several factors which govern the selection of a material. In Section 2.3.4 the absorption coefficients of sound are tabulated. From these it is obvious that the paramagnetic ion should be either a rare earth ion or an ion with an even number of unpaired electrons. These particular configurations yield the highest absorption coefficient. Neither of these types of paramagnetic ions have been widely investigated. The even configurations investigated have been Fe^{2+} and Ni^{2+} in MgO[35] and V^{3+} in CdS, ZnS and ZnTe[36]. The rare earths have not been investigated to any extent. Of these materials, it was pointed out in Section 2.4.3 that a nonlinear interaction can occur in piezoelectric semiconductors such as CdS. Lastly CdS is a hexagonal crystal so that a zero field splitting occurs among the spin states. Consequently, the ideal

34. Shiren, N. S., loc. cit.

35. Low, W., loc. cit.

36. Ludwig, G. N., Woodbury, H. H., loc. cit.

material for this type of parametric interaction seems to be vanadium doped cadmium sulfide. There are, however, certain problems in growing vanadium doped cadmium sulfide.

2.6 Vanadium Doped Cadmium Sulfide Energy Eigenvalues.

Before beginning any experimental work on CdS:V^{3+} it is first necessary to calculate the expected energy eigenvalues for paramagnetic interaction. The energy eigenvalues are obtained by finding the matrix elements of the Hamiltonian and then finding the characteristic values. The eigenvectors could then be found which would indicate the admixture of the pure spin states in each eigenvector. To be precise, the eigenvalues should be obtained for each of the 24 energy levels, three fine lines each divided into eight hyperfine lines due to the vanadium nuclear spin. The spectrum is further complicated by two inequivalent spin sites. The Hamiltonian is given by

$$|—| = \beta [g_{||} J_z H_z + g_{\perp} (J_x H_x + J_y H_y)] + DJ_z^2$$

$$+ \frac{a}{6} [J_\xi^4 + J_\eta^4 + J_\zeta^4] + \frac{F}{180} [35 J_z^4 - 30 J(J + 1) J_z^2 + 25 J_z^2]$$

$$+ AJ_z I_z + B (J_x I_x + J_y I_y) \quad . \quad (2.44)$$

The ξ, η, ζ axes are given so that the body diagonal of the cube formed by the ξ, η, ζ unit vectors lies along the z-axis. It is possible to show that for the appropriate orientation of the $\xi\eta\zeta$ axis and since $J = 1$ the terms in a and F do not contribute. Also $g_{||} \approx g_{\perp}$ and $A \approx B$ so that the Hamiltonian can be approximately reduced to

$$|—| = g\beta J \cdot H + DJ_z^2 + AJ \cdot I \quad . \quad (2.45)$$

To simplify the results, assume $A = 0$. This gives a 3 x 3 matrix which can be solved for the energy-eigenvalues. The spin state $J = 1$ is

32

represented by the eigenstate $|1>$, $J = 0$ by $|0>$ and $J = -1$ by $|-1>$.

The matrix elements are then given by

Table 2.5

Hamiltonian Matrix Elements

	$\|+1>$	$\|0>$	$\|-1>$
$<+1\|$	$D + g\beta H \cos\theta$	$\frac{1}{\sqrt{2}} g\beta H \sin\theta\, e^{i\psi}$	0
$<0\|$	$\frac{1}{\sqrt{2}} g\beta H \sin\theta\, e^{-i\psi}$	0	$\frac{1}{\sqrt{2}} g\beta H \sin\theta\, e^{i\psi}$
$<-1\|$	0	$\frac{1}{\sqrt{2}} g\beta H \sin\theta\, e^{-i\psi}$	$D - g\beta H \cos\theta$

where θ is the polar angle from the z-axis and ψ is the angle measured in the x-y plane from the x-axis.

Diagonalizing this matrix and solving gives the energy levels of Fig. 2.3 for angles of $\theta = 0°$, $\cos^{-1} 1/\sqrt{3}$ and $90°$.

With $A \neq 0$ the matrix becomes considerably more complicated and expands to a 24 x 24 matrix. In general there is no simplification that results in a reduction of the matrix except by setting $\theta = 0°$. This eliminates off diagonal terms due to electron spin but does not affect the terms due to nuclear spin-electron spin interaction. At $\theta = 0°$ the matrix breaks up into six 3 x 3 submatrices, two 2 x 2 and two 1 x 1 matrices. Hence it is possible to calculate the energy eigenvalues at $0°$. If a spin eigenstate is denoted by $|M, m>$, where M is the electronic spin quantum number and m the nuclear spin quantum number and the matrix elements between these states at $0°$ are evaluated, it is found that the submatrices involve admixtures of the following states:

33
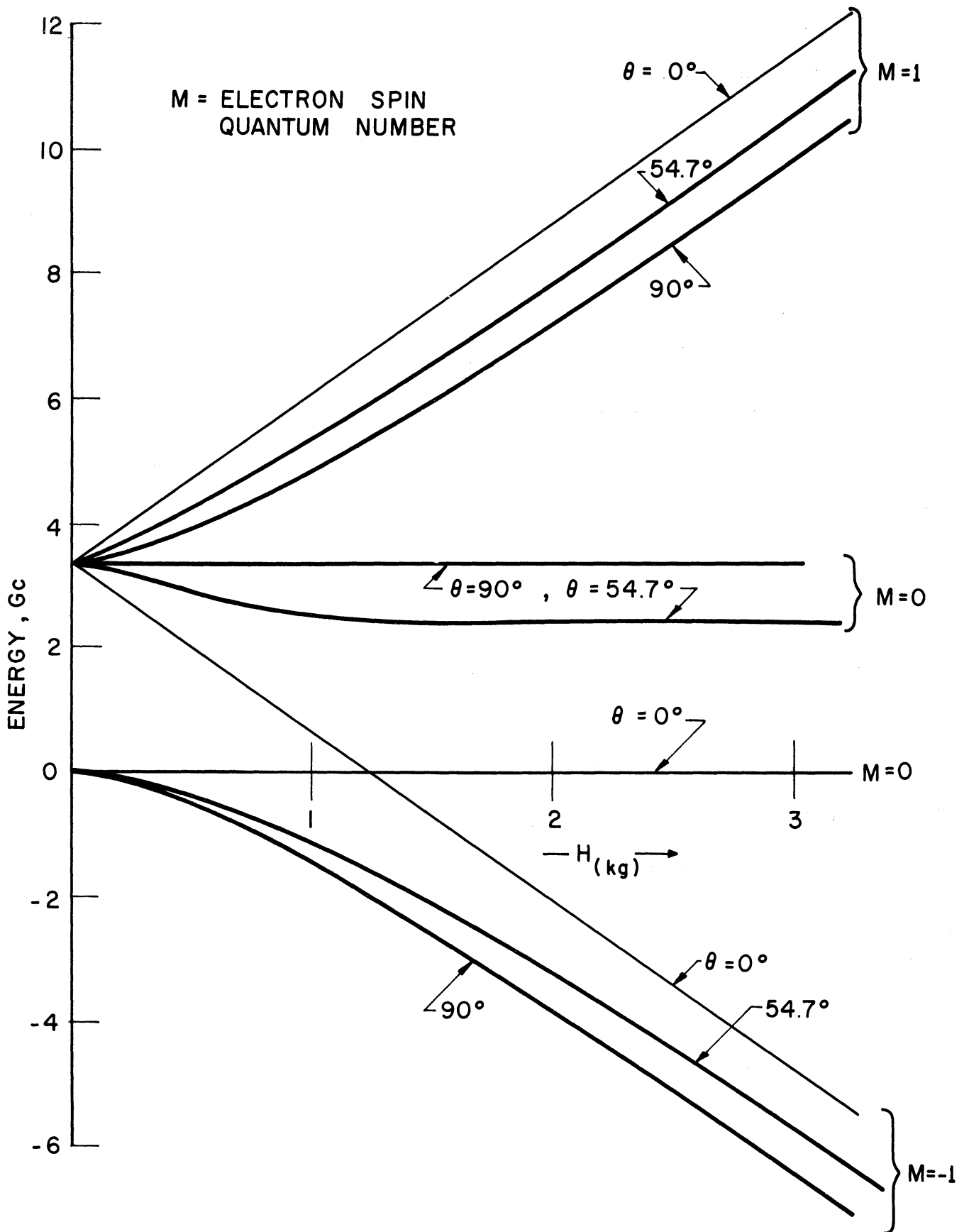
FIG. 2.3 ENERGY EIGENVALUES AS A FUNCTION OF ANGLE, A = 0.

$|1, 7/2 >$

$|0, 7/2 >$ and $|1, 5/2 >$

$|-1, 7/2 >$, $|0, 5/2 >$, and $|1, 3/2 >$

$|-1, 5/2 >$, $|0, 3/2 >$, and $|1, 1/2 >$

$|-1, 3/2 >$, $|0, 1/2 >$, and $|1, - 1/2 >$

$|-1, 1/2 >$, $|0, - 1/2 >$, and $|1, - 3/2 >$

$|-1, - 1/2 >$, $|0, - 3/2 >$, and $|1, - 5/2 >$

$|-1, - 3/2 >$, $|0, - 5/2 >$, and $|1, - 7/2 >$

$|-1, - 5/2 >$, and $|0, - 7/2 >$

$|-1, - 7/2 >$.

This shows the six 3 x 3 submatrices, the two 2 x 2's and the two unperturbed states. Some of the submatrices have been diagonalized and the energy eigenvalues were determined. Those chosen were the two unperturbed levels, the two 2 x 2's and the first and last 3 x 3 since they differed only in the signs of some of the terms. The eigenvalues are determined by solving $W = D + (7/2) A + g\beta H$, $W = D + (7/2) A - g\beta H$

$$W^2 - [g\beta H + D + (5/2) A] W - (7/2) A^2 = 0 ,$$

$$W^2 - [-g\beta H + D + (5/2) A] W - (7/2) A^2 = 0 ,$$

$[- g\beta H + D - (7/2) A - W] [W^2 - \{g\beta H + D + (3/2) A\} W - 6A^2]$

$$- (7/2) A^2 [g\beta H + D + (3/2) A - W] = 0$$

and

$[g\beta H + D - (7/2) A - W] [W^2 - \{ -g\beta H + D + (3/2) A\} W - 6A^2]$

$$- (7/2) A^2 [-g\beta H + D + (3/2) A - W] = 0 ,$$

and using $D = 0.1130 \text{ cm}^{-1}$ and $A = 0.0064 \text{ cm}^{-1}$.

The curves of Fig. 2.4 are then obtained. Note that although A is more than one order of magnitude smaller than D the curves are drastically affected for magnetic field less than 1 kg. Also it is possible to get transitions between states which are mixed.

2.7 Experimental Results.

2.7.1 Ruby Experiments. At the beginning of this contract several experiments to detect nonlinear interaction in ruby were undertaken. It is known that parametric interaction of phonon waves is a general property of all materials having a suitable ω-β diagram. Because of the availability of several small ruby rods from a previous laser project experimental effort at the beginning was channeled toward measuring the ω-β diagram for phonon waves in these rods. Acoustic paramagnetic resonance will occur for any suitable paramagnetic material so that information gained from this investigation would be useful in any experiment involving acoustic paramagnetic resonance. In order to construct a possible phonon parametric amplifier, more detail knowledge of the ω-β diagram is required. Since the wavelength of phonon waves approaches optical wavelengths, the material needs to be polished flat and parallel on the end surfaces. With the small ruby rods for a laser available, attempts were made to measure the ω-β diagram. The method of measurement was to resonate the length of the rod by a pulse several times as long as the transit time through the rod. The resonance causes the reflected wave to add in phase with the input pulse and cause a buildup of phonon waves in the material. This condition is illustrated in Fig. 2.5. Then by adjusting the magnetic field for paramagnetic resonances, the phase velocity will change, thus changing the apparent length of the rod. Consequently as the magnetic field is swept, the rod will change from resonance to antiresonance.
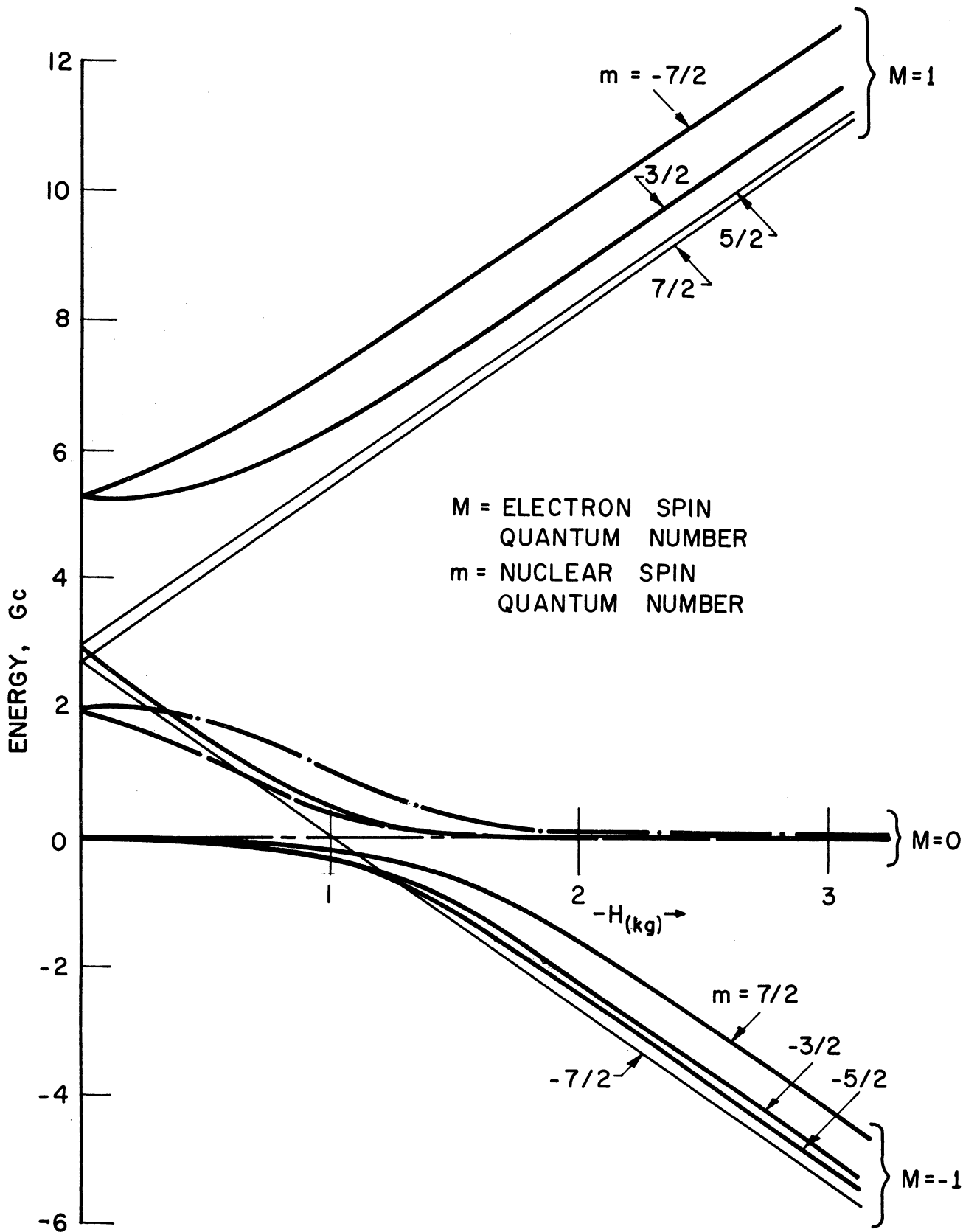
FIG. 2.4   TWELVE OF THE TWENTY-FOUR ENERGY EIGENVALUES FOR $\theta = 0°$, $A \neq 0$.
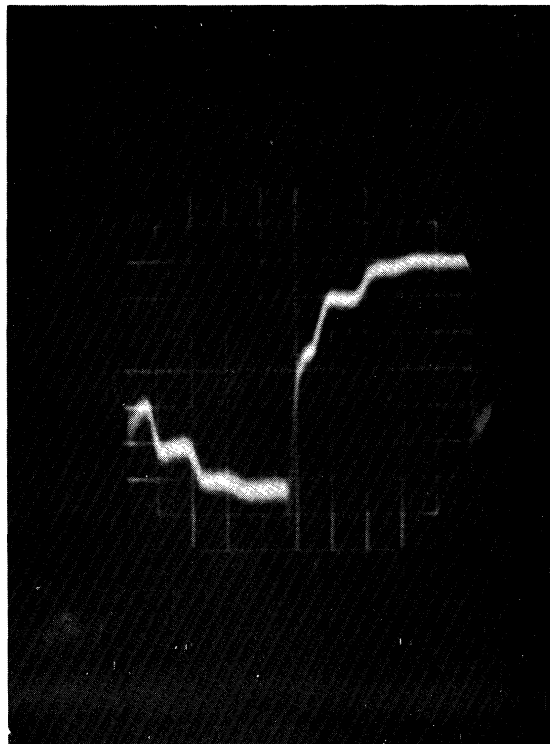
←— TIME ——

10 μsec / cm   PHONON FREQUENCY
~ 29.8 Mc/sec

FIG. 2.5   RESONANT BUILDUP OF PHONON WAVE.

Antiresonance is illustrated in Fig. 2.6 where the wave has a net 180°

phase shift per round trip. By measuring the change in field between

resonant points and knowing the change in phase between these resonances,

it is possible to construct an ω-β diagram.

As mentioned earlier, the frequency should be increased to increase

the absorption coefficient. However, the material attenuation constant

increases extremely rapidly above 1000 mc at room temperature. Conse-

quently, attempts were made to observe the ω-β diagram for phonon waves in

the UHF region, 300 to 700 mc. Another reason for this was that it is

difficult to find a long pulse (> 50 μ sec) source at much higher

frequencies. The long pulse was needed because the two-way transit time

of the ruby rod is 12 μ sec.

In attempting to obtain acoustic echoes at these frequencies, a

wideband transducer was obtained so that the frequency could be changed

easily. The transducer, an x-cut quartz crystal, giving longitudinal waves

has a fundamental resonance of 1.4 mc. The ruby rod had resonances every

70 kc because of its much greater length. The transducer was mounted at

the end of an open-circuited transmission line which gives maximum

electric field to couple piezoelectrically with the phonon wave in the

quartz. This setup gives wideband response because of its lack of tuned

circuits. The transducer was then bonded mechanically onto the ruby.

Figure 2.7 is a drawing of the transmission-line transducer. Using this

equipment, echoes were seen for frequencies up to 200 mc. using these

transducers.

A trial package of transducers was obtained from Valpey Corporation.

These transducers were gold plated x-cut longitudinal quartz units which

were resonant at various frequencies from 5 mc to 40 mc. A 17.5 mc
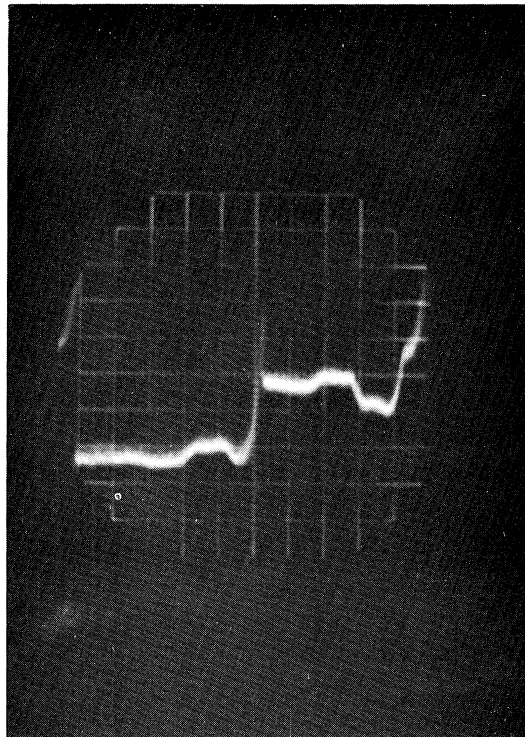
◄— TIME —►

10 μ sec / cm   PHONON FREQUENCY
~ 29.8 Mc / sec.

FIG. 2.6   ANTIRESONANT BUILDUP OF PHONON WAVE.

COAXIAL

INSULATOR

QUARTZ TRANSDUCERS

RUBY ROD

GROUND PLANE

INSULATOR

COAXIAL
INPUT
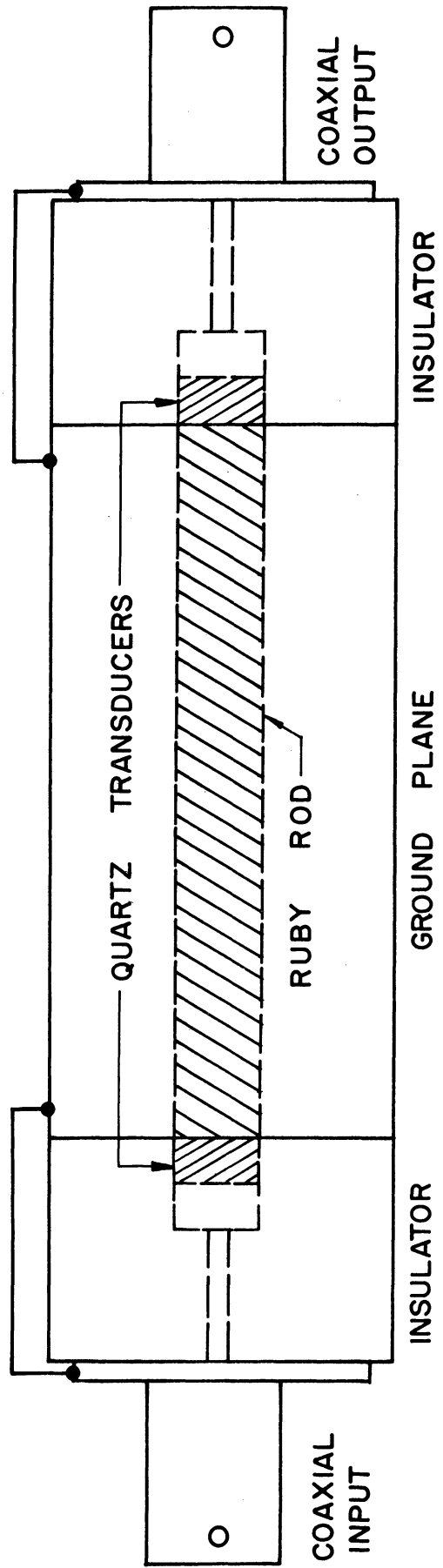
FIG. 2.7 TRANSMISSION-LINE TRANSDUCER.

transducer was used which was plated in such a way that connections to both sides were made from the front surface. This transducer was bonded with Duco Cement to the ruby rod in place of the 1.4 mc transducer. Using this experimental setup echoes have been observed as high as 577 mc at room temperature. Figures 2.8 through 2.11 show some representative results at various frequencies. A noticeable improvement in the echo pattern has been observed when operating at 77°K. This is attributed to the improvement in the mechanical bond between transducer and rod. Using this apparatus echoes have been seen as high as 892 mc. This has been achieved using a configuration similar to that illustrated in Fig. 2.7. For this application resonant transducers with gold plating on each side have been bonded to each end of the ruby rod. These transducers are resonant at 17.5 mc and 10.5 mc respectively, i.e., in the ratio 5:3. Thus every fifth harmonic of the 10.5 mc transducer corresponds to every third harmonic of the 17.5 mc transducer. Thus it is possible to obtain transmission at the following frequencies (only odd harmonics resonate) as shown below.

Table 2.6

Transducer Eigenfrequencies

f (mc)	Harmonic No. of 17.5 mc Transducer	Harmonic No. of 10.5 mc Transducer
52.5	3	5
157.5	9	15
262.5	15	25
367.5	21	35
472.5	27	45
577.5	33	55
682.5	39	65
787.5	45	75
892.5	51	85

10 μ sec / cm

20 μ sec / cm

50 μ sec / cm
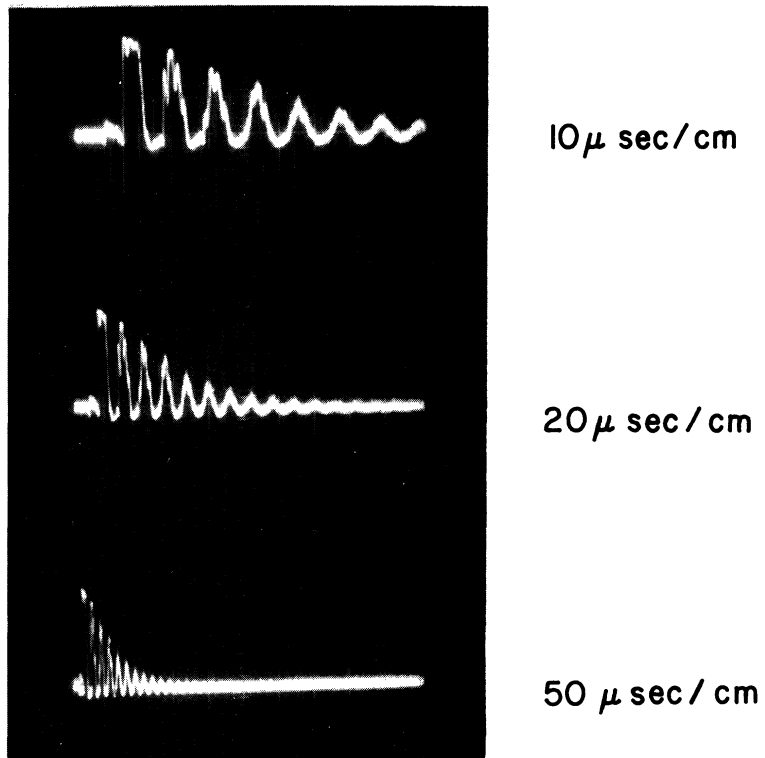
29.3 Mc / sec

FIG. 2.8 ROOM TEMPERATURE ECHOES.

50 μsec / cm

20 μsec / cm

10 μsec / cm
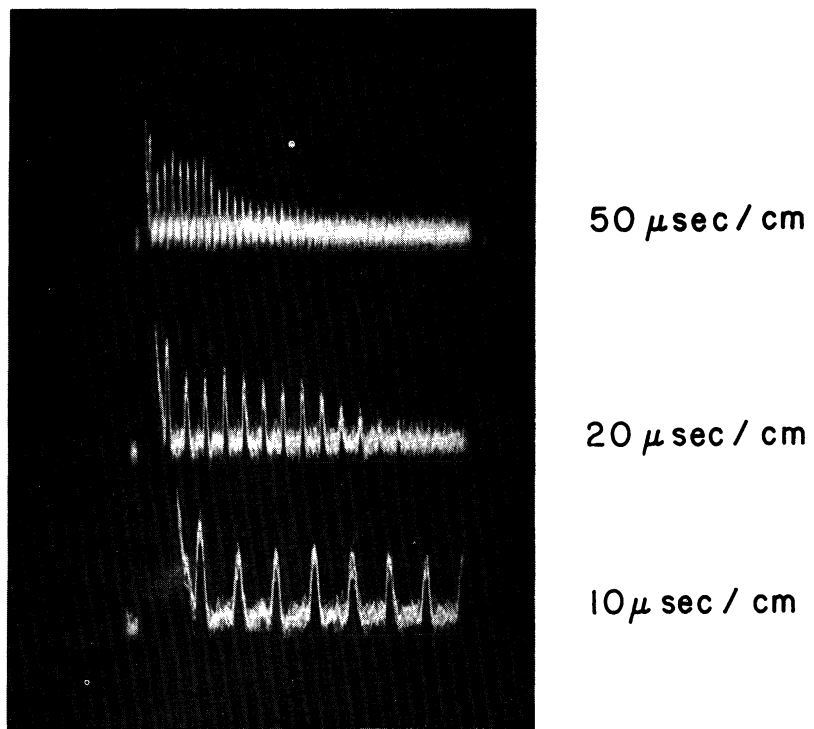
121 Mc

FIG. 2.9 ROOM TEMPERATURE ECHOES.

50 μ sec / cm

50 μ sec / cm

50 μ sec / cm

332 Mc / sec
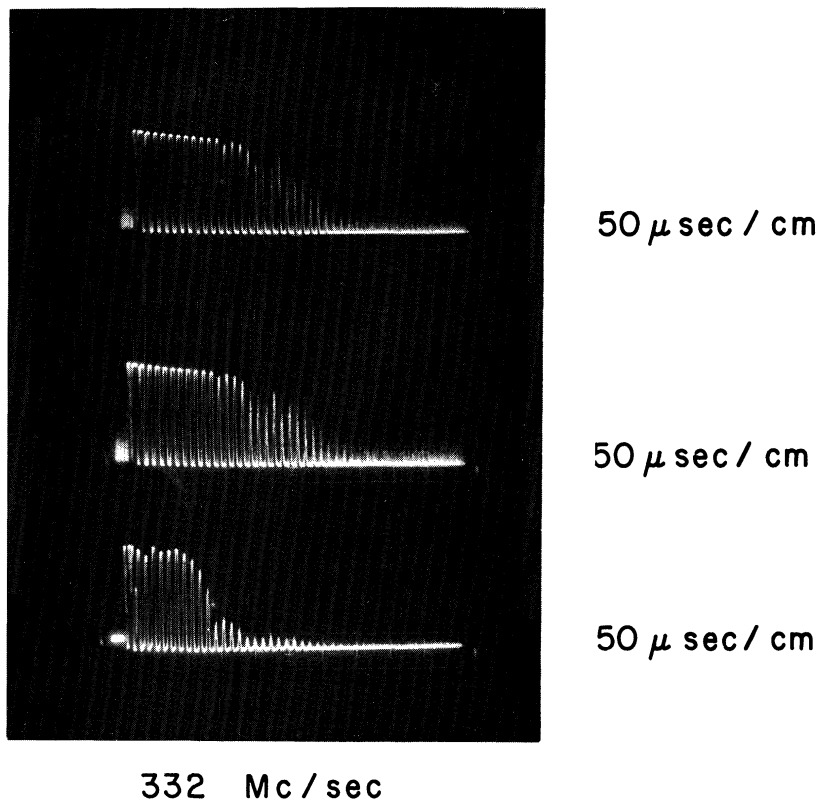
FIG. 2.10 ROOM TEMPERATURE ECHOES, RECEIVER GAIN CHANGED.

50 μ sec / cm

20 μ sec / cm

10 μ sec / cm
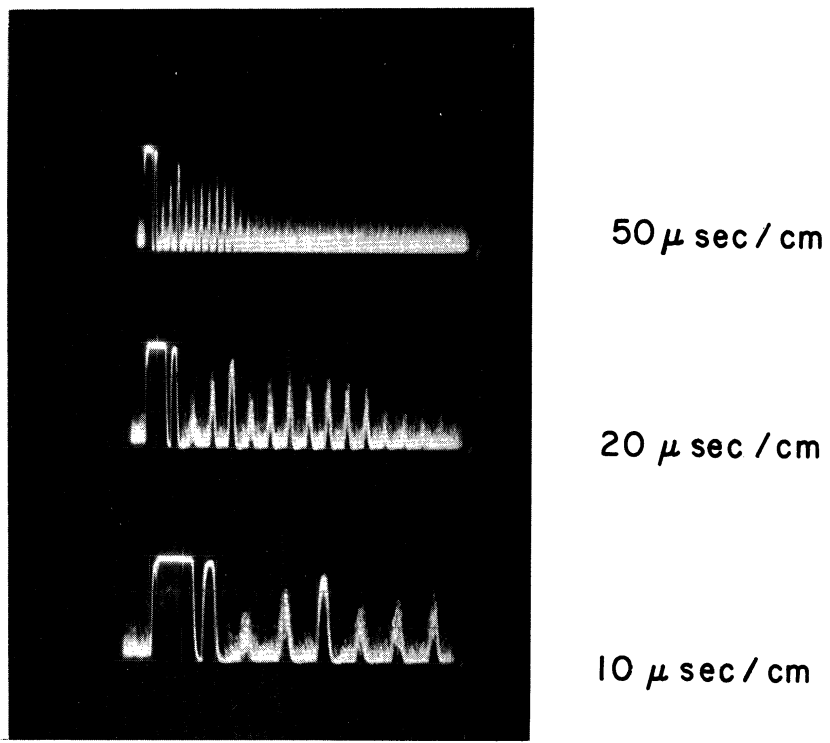
507 Mc / sec

FIG. 2.11 ROOM TEMPERATURE ECHOES.

One can see that 892.5 mc operation occurs at a very high harmonic of the fundamental resonance. This means that any imperfections in parallelism and surface preparation is most noticeable. In addition the attenuation constant of the material is getting larger at the higher frequencies. Consequently it is more difficult to see echoes at the very high frequencies. Because of these effects only one echo was observed at 892.5 mc and it was quite weak.

The use of two resonant transducers also allows multiple frequency operation. Consequently effects were investigated using a very high power pump at approximately twice the frequency of the smaller signal. The pump was square wave modulated and the signal was pulsed. This allowed a resonant buildup of pump power in the rod as illustrated in Fig. 2.5 and then application of the signal pulse. The purpose of this experiment was to determine if there was any nonlinear pumping action within the crystal due to anharmonic coupling forces between atoms in the lattice. No non-linear effect was observed. Experiments were carried on with a pump frequency of 402.5 mc (23rd harmonic of 17.5 mc) and a signal of 199.5 mc (19th harmonic of 10.5 mc) which is very near the degenerate parametric conditions $\omega_i = \omega_s$.

As noted earlier, the phonon absorption coefficient for ruby is very small and consequently any phase change introduced in the ω-β diagram would be very small. Although the nonlinear interaction in the crystal may be present, it was felt that the tuning required for successful amplifier operation could not be achieved because of the small change in phase constant. Thus further investigation of ruby as a traveling-wave parametric acoustic amplifier was dropped.

47

2.7.2 Electron Paramagnetic Resonance Spectrometer. In order
to set up a phonon parametric amplifier using vanadium doped cadmium
sulfide, the energy level spacings must be checked. To do this using
phonon waves would involve considerable complication, mainly due to pulsed
signals. Consequently, a program for investigating the energy levels was
attempted using electron paramagnetic resonance where the sample is
mounted in a cavity and low level cw microwave signals could be used.

Several different microwave configurations were used in this study.
One of the earlier configurations utilized a traveling-wave amplifier and
a transmission cavity to selectively return the signal to the amplifier so
that oscillation occurred. The sample was then placed in the cavity. The
advantage to this scheme was automatic frequency stabilization due to the
fact that the cavity determines the frequency of oscillation. As the
frequency of the cavity shifts due to changes in the dielectric constant of
the sample, the oscillation frequency automatically follows. The disadvan-
tage was that operation was limited to the fundamental frequency of the
transmission cavity. It is necessary to investigate the spectrum over a
range of 4 to 10 Gc due to the splitting of the energy levels which can
be seen in Fig. 2.4. This would mean a number of different cavities as
well as traveling-wave amplifiers. Oscillations at other frequencies cause
noise so that only the fundamental cavity frequency should be present.

In order to satisfy the requirements of wide tunability a coaxial
system seemed most appropriate. However, the lack of a coaxial equivalent
of the waveguide hybrid T made coaxial systems very difficult. A coaxial
cavity, tunable from 1 to 10 Gc, was built. Using this cavity it was
possible to operate over a wide frequency range with good coupling to the
cavity. This cavity was used either in a simple video detection

configuration as shown in Fig. 2.12 or in a balanced bridge arrangement as shown in Fig. 2.13.

The video detection arrangement consists of a stabilized klystron oscillator driving a magic-T. One arm of the T contains the cavity which is located in a dewar in the magnetic field. The second arm contains a slide screw tuner and load so that the phase and amplitude of the input signal reflected to the crystal detector can be changed, thus changing the crystal bias.

This system was quite good in that one could easily detect as little as one grain of DPPH at helium temperatures. However, the vanadium absorption lines were not observed. Consequently a more sophisticated microwave bridge was used as shown in Fig. 2.13.

The balanced bridge spectrometer used superheterodyne detection. One arm of the bridge contained the cavity, the other arm contained an attenuator and phase shifter. The idea was to balance the two signals in the magic-T so that the 30 mc receiver was not saturated. Then, since the reflected power from the cavity changes with absorption of the crystal in a magnetic field, the signal received at the 30 mc receiver was the difference. Thus one had the greatest possible gain and consequently the most sensitive spectrometer. Even with this system no absorption was observed even though the receiver was saturated with the signal from a grain of DPPH. In order to reduce the noise caused by frequency drift and cavity vibration a fixed tuned X-band rectangular cavity was built which operated in the TE_{012} mode. The sample was mounted midway on the long axis, thus placing the sample in maximum r-f magnetic field. Orienting the cavity so that the r-f and d-c magnetic fields were always orthogonal gave the highest matrix elements for electromagnetic absorption

LOAD

DETECTOR

ISOLATOR

SLIDE
SCREW
TUNER

MAGIC-
T

ATTENUATOR

STABILIZED
SIGNAL
GENERATOR

CAVITY

MAGNET

MODULATING FIELD
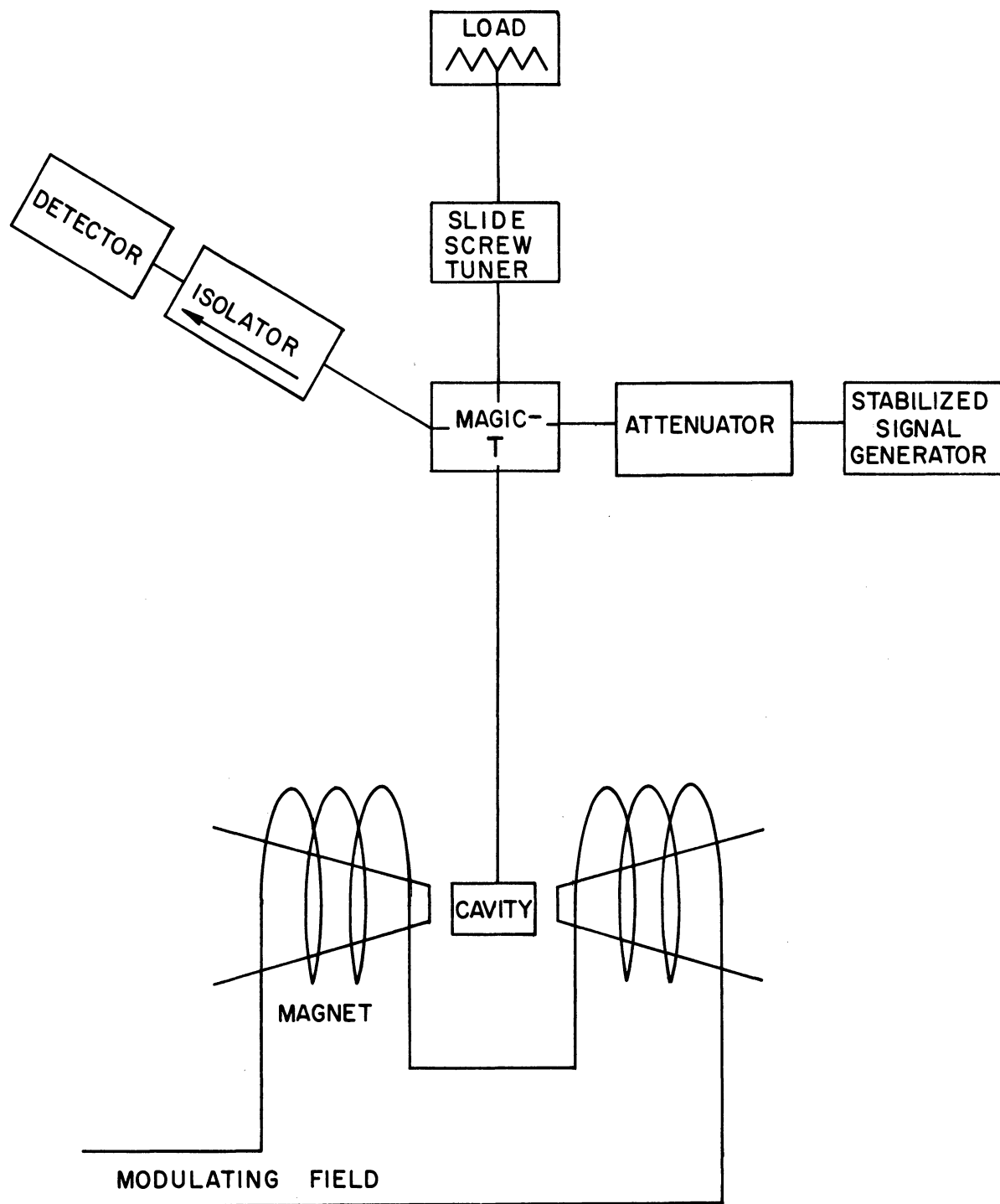
FIG. 2.12 MICROWAVE ELECTRON PARAMAGNETIC RESONANCE SPECTROMETER.

PHASE SHIFTER   ◄── ISOLATOR

VARIABLE ATTENUATOR   ⋏ LOAD

VIDEO TO LOCK-IN AMPLIFIER

30 MC. RECEIVER

TRANSFORMER

STABILIZED KLYSTRON OSCILLATOR

LOCAL OSCILLATOR

STABILIZED KLYSTRON OSCILLATOR

BALANCED MIXER

MAGIC-T

CAVITY

MAGNET

MODULATION FIELD
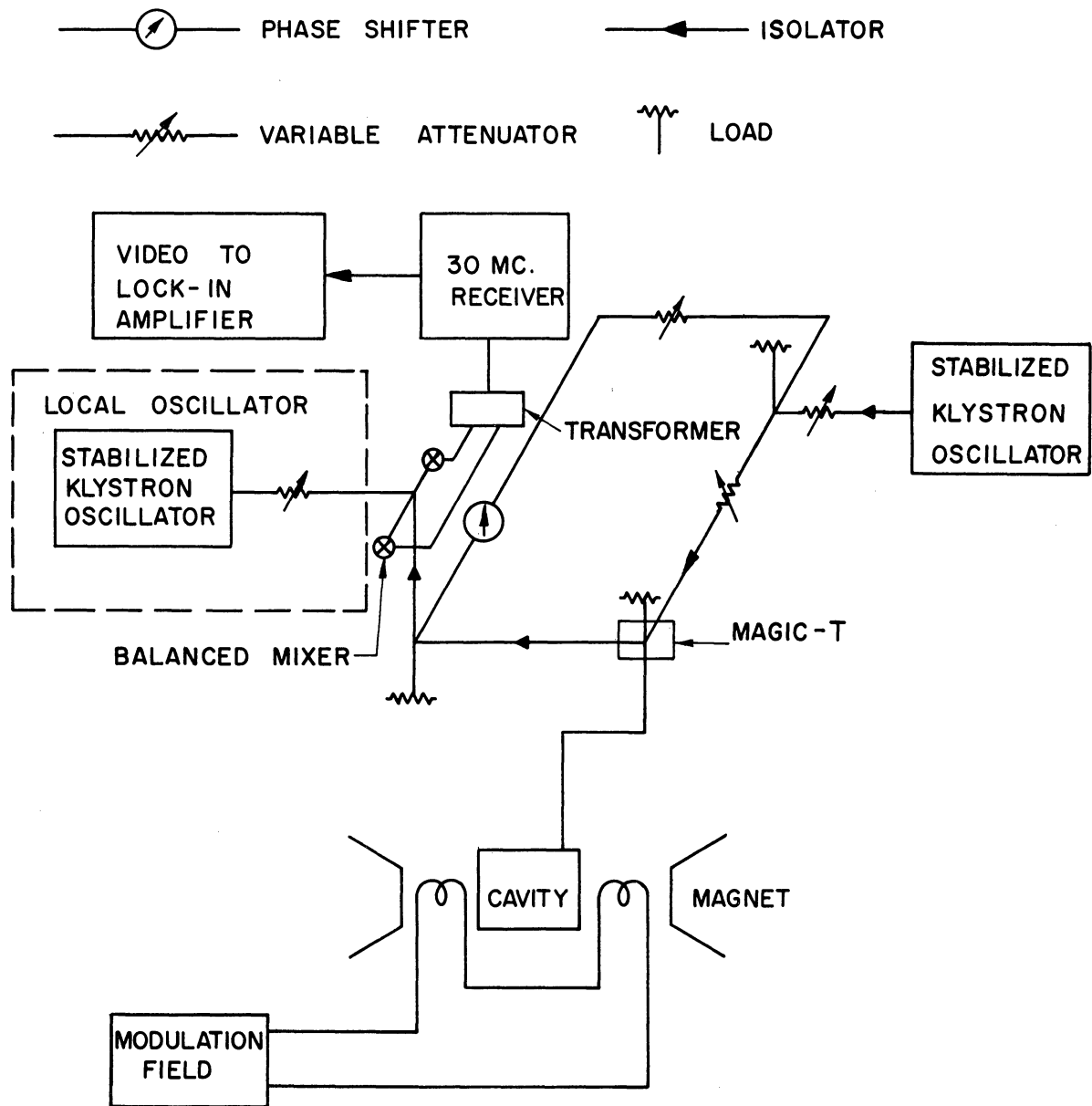
FIG. 2.13   BALANCE BRIDGE SUPERHETERODYNE SPECTROMETER.

by the spin system. This cavity was used in both spectrometer arrangements. The balanced bridge gave a very sensitive response with minimum noise because of the use of an ultrastable oscillator.

2.7.3 <u>Vanadium Doped Cadmium Sulfide Results</u>. After many attempts to find electron paramagnetic resonance with no success it was decided to try phonon paramagnetic resonance. In order to do this, the sample which was obtained from Semi-elements in the form of a cylinder had to be polished on the ends. While polishing one end the sample was found to be inhomogeneous in color; it also had pits, cracks and bubbles in it. With this information it was decided that it would be highly unlikely to have either electron or phonon paramagnetic resonance because of the inhomogeneity of doping. Because of the difficulty in obtaining another vanadium doped sample and also considering the possibility that nothing new would be learned from this experiment this effort was ended.

<u>3</u>. <u>Plasma Interaction in Solids</u>   (J. E. King)

3.1 <u>Introduction</u>. In the course of an extensive literature survey many reports of bulk semiconductor oscillation were noted[1-4].

1. Hurwitz, C. E., McWhorter, A. L., "Growing Helical Density Waves in Semiconductor Plasmas", <u>Physical Review Letters</u>, vol. 10, No. 1, pp. 20-22; January, 1963.

2. Kikuchi, M., Abe, Y., "Observations of Instability in Semiconductors Caused by Heavily Injected Minority Carriers", <u>Jour. of the Phys. Soc. of Japan</u>, vol. 17, No. 8, pp. 1268-1280; August, 1962.

3. Kikuchi, M., "Experimental Observations of Undamped Current Oscillations in CdSe Single Crystals", <u>Japanese JAP</u>, vol. 3, No. 8., pp. 448-458; August, 1964.

4. Interim Engineering Report No. 1, Solid State Plasma Microwave Generators, RCA Laboratories, Princeton, N. J.; September, 1964.

These reports and many more indicate the possibility of a fundamental interaction between the semiconductor viewed as a plasma and an externally controlled variable such as the current. The purpose of this investigation will be to develop a theory for semiconductor plasma interactions that will predict instabilities that occur both with and without a magnetic field.

One of the major problems is that the motion of particles in the semiconductor are governed by the laws of motion for a crystal lattice. In particular if an energy surface is defined, the velocity and effective mass of the particle are determined by the derivatives of the energy with respect to the crystal momentum. The complicating factor is that there are several bands, oriented in various directions, which must be taken into account.

The approach which will be taken is to evaluate the distribution function in the Boltzmann equation for an elliptic energy surface. The conductivity will then be found for this band. The effects of all the bands will be accounted for by adding their contributions to the conductivity. This will involve using rotation matrices to account for the band orientation. Finally instabilities in the electromagnetic field will be investigated using the current density and conductivity calculated from the Boltzmann equation.

3.2 Boltzmann Equation and Distribution Function. The general Boltzmann equation can be written as

$$\frac{\partial f}{\partial t} + \dot{\vec{r}} \cdot \nabla_r f + \dot{\vec{k}} \cdot \nabla_k f = \left(\frac{\partial f}{\partial t} \right)_{coll} , \qquad (3.1)$$

where $\rightharpoonup$ represents a vector quantity,

$\leftrightharpoons$ represents a tensor quantity and

$f(\vec{r},\vec{k},t)$ denotes the fraction of the total number of electrons whose position coordinates lie between $\vec{r}$ and $\vec{r} + \vec{dr}$ and whose wave vector lies between $\vec{k}$ and $\vec{k} + \vec{dk}$ at a time t.

Assume that the collision term can be represented by a collision frequency or collision time which is not isotropic and is actually a tensor dependent on the energy.

Under steady-state conditions the Boltzmann equation now becomes

$$\left(\overleftrightarrow{\tau}\ \dot{\vec{r}}\right) \cdot \nabla_r f + \left(\overleftrightarrow{\tau}\ \dot{\vec{k}}\right) \cdot \nabla_k f = (f - f_o) \ , \qquad (3.2)$$

where the collision relaxation time $\overleftrightarrow{\tau}$ is given by

$$\overleftrightarrow{\tau} = \begin{bmatrix} \tau_x & 0 & 0 \\ 0 & \tau_y & 0 \\ 0 & 0 & \tau_z \end{bmatrix} . \qquad (3.3)$$

From the Lorentz force equation

$$\vec{F} = \hbar \dot{\vec{k}} = q[\vec{E} + \vec{v} \times \vec{B}] \ , \qquad (3.4)$$

where $\vec{F}$ = force,

$\hbar$ = Plank's constant/2π,

$\vec{E}$ = electric field vector,

$\vec{v}$ = velocity vector = $\dot{\vec{r}}$,

$\vec{B}$ = magnetic field vector,

q = charge (for electron q = - e)

and from the relations for velocity in a solid,

$$\vec{v} = \dot{\vec{r}} = \frac{1}{\hbar} \nabla_k \mathcal{E} \quad , \tag{3.5}$$

where $\mathcal{E}$ = energy, the Boltzmann equation can be reduced to

$$\frac{1}{\hbar}\left(\tau\nabla_k\mathcal{E}\right) \cdot \nabla_r f + \left[\frac{q}{\hbar}\tau\left(\vec{E} + \frac{1}{\hbar}\nabla_k\mathcal{E}x\vec{B}\right)\right] \cdot \nabla_k f = (f - f_0) \quad . \tag{3.6}$$

For a small anisotropy, f can be replaced by an isotropic part and a small correction term. Let

$$f = f_0(\mathcal{E}) - \frac{1}{\hbar}\vec{G} \cdot \nabla_k\mathcal{E}\frac{\partial f_0}{\partial\mathcal{E}} \quad , \tag{3.7}$$

where $\vec{G}$ is a measure of the degree of anisotropy. Recall that the isotropic normalized equilibrium distribution function in energy is the Fermi-Dirac probability function. That is

$$f_0(\mathcal{E}) = \left[1 + \exp\left(\frac{\mathcal{E}-\mathcal{E}_F}{kT}\right)\right]^{-1} \quad , \tag{3.8}$$

where $\mathcal{E}_F$ = Fermi energy.

As a result of this distribution function

$$\nabla_r f = -\frac{\partial f_0}{\partial\mathcal{E}}\left[T \nabla_r\left(\frac{\mathcal{E}_F}{T}\right) + \frac{\mathcal{E}}{T}\nabla_r T\right] \quad . \tag{3.9}$$

For small anisotropy the Boltzmann equation then becomes

$$-\left\{\tau\left[T\nabla_r\left(\frac{\mathcal{E}_F}{T}\right) + \frac{\mathcal{E}}{T}\nabla_r T\right]\right\} \cdot \nabla_k\mathcal{E} + q(\tau \vec{E}) \cdot \nabla_k\mathcal{E}$$

$$-\frac{q}{\hbar^2}[\tau(\nabla_k\mathcal{E}x\vec{B})] \cdot \nabla_k(\vec{G} \cdot \nabla_k\mathcal{E}) + \vec{G} \cdot \nabla_k\mathcal{E} = 0 \quad . \tag{3.10}$$

Now define a reciprocal effective mass tensor $\overleftrightarrow{\mu}$ with components

$$\mu_{ij} = \frac{1}{\hbar^2} \frac{\partial^2 \mathcal{E}}{\partial k_i \partial k_j} \qquad (3.11)$$

and collecting terms the magnetic field term becomes

$$- q \left[\overleftrightarrow{\tau} (\nabla_k \mathcal{E} \times \vec{B}) \right] \cdot \left[\hbar^2 \vec{G} \cdot \overleftrightarrow{\mu} + \left(\nabla_k \mathcal{E} \cdot \frac{\partial \vec{G}}{\partial \mathcal{E}} \right) \nabla_k \mathcal{E} \right] . \qquad (3.12)$$

The second term is of the approximate form $\vec{a} \cdot \vec{b} \times \vec{a}$ which is identically zero. It is assumed to result in a second-order correction. As a result the Boltzmann equation finally reduces to

$$- \overleftrightarrow{\tau} \left[T \nabla_r \left(\frac{\mathcal{E}_F}{T} \right) + \frac{\mathcal{E}}{T} \nabla_r T \right] + q \overleftrightarrow{\tau} \vec{E} + q \overleftrightarrow{\tau} (\vec{G} \overleftrightarrow{\mu}) \times \vec{B} + \vec{G} = 0 \qquad (3.13)$$

for an elliptical energy band of the form

$$\mathcal{E} = \frac{\hbar^2}{2} \left(\frac{k_x^2}{m_x} + \frac{k_y^2}{m_y} + \frac{k_z^2}{m_z} \right) , \qquad (3.14)$$

where $\mu_x = (1/m_x)$, $\mu_y = (1/m_y)$ and $\mu_z = (1/m_z)$.

Equation 3.13 is an equation for $\vec{G}$ which is a measure of the anisotropy introduced by thermal gradients and electromagnetic fields. This equation is best solved by writing it in component form and solving using Cramer's Rule. Solving Eq. 3.13 yields

56

$$\vec{G} = [1 + q^2 \, (\overset{\leftrightarrow}{\alpha} \, \vec{B}) \cdot \vec{B}]^{-1} \left\{ - q \, \overset{\leftrightarrow}{\tau} \, \vec{E} + \overset{\leftrightarrow}{\tau} \left[T\nabla_r \left(\frac{\mathscr{E}_F}{T} \right) + \frac{\mathscr{E}}{T} \nabla_r T \right] \right.$$

$$+ q \, \vec{B} \times \overset{\leftrightarrow}{\tau} \left(\left\langle \overset{\leftrightarrow}{\tau} \left[T\nabla_r \left(\frac{\mathscr{E}_F}{T} \right) + \frac{\mathscr{E}}{T} \nabla_r T \right] \right\rangle \overset{\leftrightarrow}{\mu} \right)$$

$$+ q^2 \left\langle \overset{\leftrightarrow}{\tau} \left[(\overset{\leftrightarrow}{\tau} \vec{E}) \, \overset{\leftrightarrow}{\mu} \right] \right\rangle \times \vec{B} + q^2 \left\langle \overset{\leftrightarrow}{\tau} \left[T\nabla_r \left(\frac{\mathscr{E}_F}{T} \right) + \frac{\mathscr{E}}{T} \nabla_r T \right] \cdot \vec{B} \right\rangle (\overset{\leftrightarrow}{\alpha} \vec{B})$$

$$\left. - q^3 \, [(\overset{\leftrightarrow}{\tau} \vec{E}) \cdot \vec{B}] \, (\overset{\leftrightarrow}{\alpha} \vec{B}) \right\} \quad , \quad (3.15)$$

where

$$\overset{\leftrightarrow}{\alpha} = \begin{bmatrix} \dfrac{\tau_y \tau_z}{m_y m_z} & 0 & 0 \\[2ex] 0 & \dfrac{\tau_x \tau_z}{m_x m_z} & 0 \\[2ex] 0 & 0 & \dfrac{\tau_x \tau_y}{m_x m_y} \end{bmatrix}$$

and recalling that the notation $\overset{\leftrightarrow}{\alpha} \, \vec{E}$ stands for $\overset{\leftrightarrow}{\alpha} \cdot \vec{E}$.

There are two important cases to be considered:

Case 1. $\vec{B} = 0$.

In this case the anisotropy term reduces to

$$\vec{G} = - q \, \overset{\leftrightarrow}{\tau} \, \vec{E} + \overset{\leftrightarrow}{\tau} \left[T\nabla_r \left(\frac{\mathscr{E}_F}{T} \right) + \frac{\mathscr{E}}{T} \nabla_r T \right] \qquad (3.16)$$

and the distribution function becomes

$$f = f_0(\mathscr{E}) - \frac{1}{\hbar} \left\{ - q \, \overset{\leftrightarrow}{\tau} \, \vec{E} + \overset{\leftrightarrow}{\tau} \left[T\nabla_r \left(\frac{\mathscr{E}_F}{T} \right) + \frac{\mathscr{E}}{T} \nabla_r T \right] \right\} \cdot \nabla_k \mathscr{E} \, \frac{\partial f_0}{\partial \mathscr{E}} \quad . \quad (3.17)$$

57

Case 2. No Thermal Variations.

In this case the anisotropy term becomes

$$\vec{G} = \left\{ - q \overset{\leftrightarrow}{\tau} \vec{E} + q^2 \left\langle \overset{\leftrightarrow}{\tau} [(\overset{\leftrightarrow}{\tau} \vec{E}) \overset{\leftrightarrow}{\mu}] \right\rangle \times \vec{B} \right.$$

$$\left. - q^3 [(\overset{\leftrightarrow}{\tau} \vec{E}) \cdot \vec{B}] (\overset{\leftrightarrow}{\alpha} \vec{B}) \right\} [1 + q^2 (\overset{\leftrightarrow}{\alpha} \vec{B}) \cdot \vec{B}]^{-1} \qquad (3.18)$$

and the distribution function becomes

$$f = f_o(\mathcal{E}) - \frac{1}{\hbar} [1 + q^2 (\overset{\leftrightarrow}{\alpha} \vec{B}) \cdot \vec{B}]^{-1} \left\{ - q \overset{\leftrightarrow}{\tau} \vec{E} \right.$$

$$\left. + q^2 \left\langle \overset{\leftrightarrow}{\tau} [(\overset{\leftrightarrow}{\tau} \vec{E}) \overset{\leftrightarrow}{\mu}] \right\rangle \times \vec{B} - q^3 [(\overset{\leftrightarrow}{\tau} \vec{E}) \cdot \vec{B}] (\overset{\leftrightarrow}{\alpha} \vec{B}) \right\} \cdot \nabla_k \mathcal{E} \frac{\partial f_o}{\partial \mathcal{E}} \; . \qquad (3.19)$$

These two equations determine the distribution function to a
first-order correction for a semiconductor crystal with one elliptic
band. The problem now is to use this distribution function to calculate
the conductivity, then to account for all the bands in the semiconductor
by using appropriate rotation matrices and summing the conductivities in
the coordinate directions due to each of the bands.

3.3 Time Dependent Distribution Functions. If it is assumed that
each variable in the Boltzmann equation (3.1) has a steady state and a
time-varying term of the form

$$f = f_o - \frac{1}{\hbar} \vec{G} \cdot \nabla_k \mathcal{E} \frac{\partial f_o}{\partial \mathcal{E}} + f_1 e^{j\omega t} \; ,$$

$$\vec{v} = \dot{\vec{r}} = \vec{v}_o + \vec{v}_1 e^{j\omega t}$$

and

$$\vec{k} = \vec{k}_o + \vec{k}_1 e^{j\omega t} \; , \qquad (3.20)$$

58

then substituting into the Boltzmann equation and assuming a relaxation time approximation gives

$$j\omega f_1 e^{j\omega t} + (\vec{v}_o + \vec{v}_1 e^{j\omega t}) \cdot \nabla_r \left(f_o - \frac{1}{\hbar} \vec{G} \cdot \nabla_k \mathcal{E} \frac{\partial f_o}{\partial \mathcal{E}} + f_1 e^{j\omega t} \right)$$

$$+ (\dot{\vec{k}}_o + \dot{\vec{k}}_1 e^{j\omega t} + j\omega k_1 e^{j\omega t}) \cdot \nabla_k \left(f_o - \frac{1}{\hbar} \vec{G} \cdot \nabla_k \mathcal{E} \frac{\partial f_o}{\partial \mathcal{E}} + f_1 e^{j\omega t} \right)$$

$$= -\frac{1}{\hbar} \frac{\vec{G} \cdot \nabla_k \mathcal{E} \frac{\partial f_o}{\partial \mathcal{E}}}{\tau} + \frac{f_1}{\tau} e^{j\omega t} \quad (3.21)$$

and collecting nontime-varying terms

$$\vec{v}_o \cdot \nabla_{r_o} \left(f_o - \frac{1}{\hbar} \vec{G}_o \cdot \nabla_k \mathcal{E} \frac{\partial f_o}{\partial \mathcal{E}} \right) + \dot{\vec{k}}_o \cdot \nabla_{k_o} \left(f_o - \frac{1}{\hbar} \vec{G}_o \cdot \nabla_{k_o} \mathcal{E} \frac{\partial f_o}{\partial \mathcal{E}} \right)$$

$$= -\frac{1}{\hbar} \frac{\vec{G}_o \cdot \nabla_{k_o} \mathcal{E} \frac{\partial f_o}{\partial \mathcal{E}}}{\tau} \quad . \quad (3.22)$$

This is the same equation as obtained for the time independent case and has the solution given by Eq. 3.15 with the variables $\vec{G}$, $\vec{B}$ and $\vec{E}$ replaced by $\vec{G}_o$, $\vec{B}_o$ and $\vec{E}_o$.

The subscripts on the electric and magnetic field are for the time independent fields since they arise from the time independent part of the Lorentz equation. The terms containing $e^{j\omega t}$ yield the equation

59

$$j\omega f_1 + \vec{v}_0 \cdot \nabla_r f_1 + \vec{v}_1 \cdot \nabla_r \left[f_0 - \frac{1}{\hbar} \vec{G} \cdot \nabla_k \mathcal{E} \frac{\partial f_0}{\partial \mathcal{E}} \right]$$

$$+ \dot{\vec{k}}_0 \cdot \nabla_k f_1 + (\dot{\vec{k}}_1 + j\omega \vec{k}_1) \cdot \nabla_k \left[f_0 - \frac{1}{\hbar} \vec{G} \cdot \nabla_k \mathcal{E} \frac{\partial f_0}{\partial \mathcal{E}} \right]$$

$$+ \vec{v}_0 \cdot \nabla_r f_1 e^{j\omega t} + (\dot{\vec{k}}_1 + j\omega \vec{k}_1) \cdot \nabla_k f_1 e^{j\omega t}$$

$$+ [\text{terms from } \nabla_r f_0 \text{ and } \nabla_k f_0 \text{ which contain time}] = \frac{f_1}{\tau} \quad . \quad (3.23)$$

The terms in the above equation containing $e^{j\omega t}$ are second order and are dropped. However the terms from $\nabla_k f_0$ and $\nabla_r f_0$, etc. are not negligible.

Consider the energy, for an ellipsoidal band

$$\mathcal{E}(\vec{k}) = \mathcal{E}(\vec{k}^j) + \frac{\hbar^2}{2} \left[\frac{(k_1 - k_1^j)^2}{m_1} + \frac{(k_2 - k_2^j)^2}{m_2} + \frac{(k_3 - k_3^j)^2}{m_3} \right]$$

$$= \mathcal{E}^j + \frac{\hbar^2}{2} (\vec{k} - \vec{k}^j) \cdot \overset{\leftrightarrow}{\mu} (\vec{k} - \vec{k}^j) \quad , \quad (3.24)$$

where $\vec{k}_j$ is the position of the energy minimum and $\mathcal{E}(\vec{k}^j)$ is the magnitude of the energy at the minimum. Then

$$\nabla_k \mathcal{E} = \hbar^2 \left[\frac{(k_1 - k_1^j)}{m_1} \hat{1} + \frac{(k_2 - k_2^j)}{m_2} \hat{2} + \frac{(k_3 - k_3^j)}{m_3} \hat{3} \right]$$

$$= \hbar^2 \overset{\leftrightarrow}{\mu} (\vec{k} - \vec{k}^j) \quad . \quad (3.25)$$

Now if $\vec{k} = \vec{k}_0 + \vec{k}_1 e^{j\omega t}$, then

$$\nabla_k \mathcal{E} = \hbar^2 \overset{\leftrightarrow}{\mu} (\vec{k}_0 - \vec{k}^j) + \hbar^2 \overset{\leftrightarrow}{\mu} \vec{k}_1 e^{j\omega t} \quad . \quad (3.26)$$

60

Thus the gradient operator does have a time dependent contribution. It is terms like this which must be added into Eq. 3.20 to obtain the correct results.

Recall from band theory that

$$\vec{v} = \frac{1}{\hbar} \nabla_k \mathcal{E} \quad . \tag{3.27}$$

Thus

$$\vec{v}_0 + \vec{v}_1 e^{j\omega t} = \hbar \overset{\leftrightarrow}{\mu} (\vec{k}_0 - \vec{k}^j) + \hbar \overset{\leftrightarrow}{\mu} \vec{k}_1 e^{j\omega t} \tag{3.28}$$

and

$$\vec{v}_0 = \hbar \overset{\leftrightarrow}{\mu} (\vec{k}_0 - \vec{k}^j)$$

$$\vec{v}_1 = \hbar \overset{\leftrightarrow}{\mu} \vec{k}_1 \quad . \tag{3.29}$$

The Lorentz equation is

$$\hbar \dot{\vec{k}} = q(\vec{E} + \vec{v} \times \vec{B}) \tag{3.30}$$

and thus

$$\hbar(\dot{\vec{k}}_0 + \dot{\vec{k}}_1 e^{j\omega t} + j\omega \vec{k}_1 e^{j\omega t}) = q[\vec{E}_0 + \vec{E}_1 e^{j\omega t} + (\vec{v}_0 + \vec{v}_1 e^{j\omega t}) \times (\vec{B}_0 + \vec{B}_1 e^{j\omega t})]$$

giving

$$\hbar \dot{\vec{k}}_0 = q\vec{E}_0 + q\vec{v}_0 \times \vec{B}_0 \tag{3.31}$$

and

$$\hbar(\dot{\vec{k}}_1 + j\omega \vec{k}_1) = q\vec{E}_1 + q\vec{v}_1 \times \vec{B}_0 + q\vec{v}_0 \times \vec{B}_1 \quad , \tag{3.32}$$

where the term in $\vec{v}_1 \times \vec{B}_1$ is of second order and thus has been dropped. In the future Eq. 3.23 will be solved subject to the conditions (3.29) coming from band theory and Eqs. 3.31 and 3.32 from the Lorentz force

equation. In addition Maxwell's equations are also coupled because of the electric and magnetic fields.

3.4 <u>Current Densities Due to a Single Elliptic Band</u> (Time Independent). For a material having n particles of charge q per unit volume, all moving with velocity $\vec{v}$, the current density $\vec{J}$ is

$$\vec{J} = n e \vec{v} \ . \tag{3.33}$$

When the velocities are not all the same, the current density becomes

$$\vec{J} = q \int \vec{v} \, dn \ , \tag{3.34}$$

where dn represents the number of electrons (or particles) per unit volume whose velocities lie in a range $\vec{v}$ to $\vec{v} + d\vec{v}$. This velocity range corresponds to a wave vector range $\vec{k}$ to $\vec{k} + d\vec{k}$. Since each particle occupies one energy state, this is equivalent to the density of states. Then

$$\vec{J} = \frac{q}{4\pi^3} \int \vec{v} \, f \, d^3k \ , \tag{3.35}$$

where q < 0 for electrons. Recall that

$$f = f_o - \frac{1}{\hbar} \vec{G} \cdot \nabla_k \mathcal{E} \frac{\partial f_o}{\partial \mathcal{E}}\bigg|_o \ . \tag{3.36}$$

Substituting Eq. 3.36 into Eq. 3.35 it is seen that since f_o is a perfectly symmetric function in $\vec{k}$, the integral of $\vec{v}$, an odd function of $\vec{k}$, will be zero. Then the only contribution is that due to the anisotropy. Thus using Eqs. 3.27 and 3.24

$$\vec{J} \;=\; -\,\frac{q}{4\pi^3\hbar}\;\int\;\frac{1}{\hbar}\,\nabla_k\mathcal{E}\left\{-\,q\overset{\leftrightarrow}{\tau}\,\vec{E}+\overset{\leftrightarrow}{\tau}\left[T\nabla_r\left(\frac{\mathcal{E}_F}{T}\right)+\left(\frac{\mathcal{E}}{T}\right)\nabla_r T\right]\right.$$

$$+\,q\vec{B}\times\overset{\leftrightarrow}{\tau}\left(\left\langle\overset{\leftrightarrow}{\tau}\left[T\nabla_r\left(\frac{\mathcal{E}_F}{T}\right)+\left(\frac{\mathcal{E}}{T}\right)\nabla_r T\right]\right\rangle\overset{\leftrightarrow}{\mu}\right)+q^2\left\langle\overset{\leftrightarrow}{\tau}\left[(\overset{\leftrightarrow}{\tau}\,\vec{E})\,\overset{\leftrightarrow}{\mu}\right]\right\rangle\times\vec{B}$$

$$+\,q^2\left\langle\overset{\leftrightarrow}{\tau}\left[T\nabla_r\left(\frac{\mathcal{E}_F}{T}\right)+\left(\frac{\mathcal{E}}{T}\right)+\frac{\mathcal{E}}{T}\nabla_r T\right]\cdot\vec{B}\right\rangle\cdot(\overset{\leftrightarrow}{\alpha}\,\vec{B})$$

$$\left.-\,q^3\,[(\overset{\leftrightarrow}{\tau}\,\vec{E})\cdot\vec{B}]\,(\overset{\leftrightarrow}{\alpha}\,\vec{B})\right\}\cdot\nabla_k\mathcal{E}\,\frac{\partial f_o}{\partial\mathcal{E}}\,[1+q^2\overset{\leftrightarrow}{\alpha}\,\vec{B}\cdot\vec{B}]^{-1}\,d^3k\quad.\quad(3.37)$$

Introducing the notation

$$\vec{V}\;=\;-\,q\,\overset{\leftrightarrow}{\tau}\,\vec{E}+\overset{\leftrightarrow}{\tau}\left[T\nabla_r\left(\frac{\mathcal{E}_F}{T}\right)+\left(\frac{\mathcal{E}}{T}\right)\nabla_r T\right]\quad,\qquad(3.38)$$

Eq. 3.37 becomes

$$\vec{J}\;=\;\frac{-q}{4\pi^3\hbar^2}\;\int\;\nabla_k\mathcal{E}\left\{\vec{V}-q\,[\overset{\leftrightarrow}{\tau}\,(\vec{V}\,\overset{\leftrightarrow}{\mu})]\times\vec{B}\right.$$

$$\left.+\,q^2\,(\vec{V}\cdot\vec{B})\,(\overset{\leftrightarrow}{\alpha}\,\vec{B})\right\}\cdot\nabla_k\mathcal{E}\,\frac{\partial f_o}{\partial\mathcal{E}}\cdot[1+q^2\,(\overset{\leftrightarrow}{\alpha}\,\vec{B})\cdot\vec{B}]^{-1}\,d^3k\quad.\quad(3.39)$$

From this equation it is possible to calculate the conductivity tensor as the proportionality constant between $\vec{J}$ and $\vec{E}$. This would involve knowing the energy dependence of $\overset{\leftrightarrow}{\tau}$ and evaluating the integrals. This equation represents the generalized Ohm's law. That is

$$\vec{J}\;=\;\overset{\leftrightarrow}{\sigma}\,\vec{E}+\overset{\leftrightarrow}{\gamma}\,\nabla_r T\quad,\qquad(3.40)$$

where $\overset{\leftrightarrow}{\gamma}$ is the tensor quantity relating the temperature gradient to the electrical current. $\overset{\leftrightarrow}{\gamma}$ is related to the thermal conductivity and the absolute thermoelectric power.

A similar relation can be obtained for the heat current. This is defined as

$$\vec{Q} = \overline{\mathcal{E}\,n\vec{v}} \quad , \tag{3.41}$$

where the bar represents an averaged quantity

$$\vec{Q} = \frac{1}{4\pi^3} \int \mathcal{E}\,\vec{v}\,f\,d^3k \quad . \tag{3.42}$$

Again the energy is an even function of $\vec{k}$, $\vec{v}$ an odd function, and f_o an even function, so that this particular integral drops out. What is left then is

$$\vec{Q} = -\frac{1}{4\pi^3} \int \mathcal{E}\,\frac{1}{\hbar^2}\nabla_k\mathcal{E}\,\left\{\vec{V} - q\,[\overset{\leftrightarrow}{\tau}\,(\vec{\nabla}\overset{\leftrightarrow}{\mu})]\,x\,\vec{B}\right.$$

$$\left. + q^2\,(\vec{V}\cdot\vec{B})\,(\overset{\leftrightarrow}{\alpha}\,\vec{B})\right\}\cdot\nabla_k\mathcal{E}\,\frac{\partial f_o}{\partial\mathcal{E}}\,[1 + q^2\,(\overset{\leftrightarrow}{\alpha}\,\vec{B})\cdot\vec{B}]^{-1}\,d^3k \quad . \tag{3.43}$$

It should be emphasized that both $\vec{J}$ and $\vec{Q}$ from Eqs. 3.39 and 3.43 are for one elliptic band in the coordinate system of the elliptic band.

3.5 Many-Valley Model--n-Type Germanium. The conduction band of n-type germanium has eight equivalent minima located at the ends of the cube diagonals. These correspond to half-ellipsoids making a total of four complete ones. These are located in the $<111>$, $<\bar{1}11>$, $<\bar{1}\bar{1}1>$ and $<1\bar{1}1>$ directions. Assuming that the ellipsoids are ellipsoids of revolution, the transverse components of mass, relaxation time, and $\overset{\leftrightarrow}{\alpha}$ will be the same. In addition it is assumed that since the bands are

equivalent the transverse component is the same for all bands as is the longitudinal component.

In the many-valley model the bands are assumed to be noninteracting. Consequently, the contributions from each band must be added. As a result, quantities previously calculated in the coordinate system of the band must be transformed into the coordinate system of the crystal. If $\hat{I}$, $\hat{II}$ and $\hat{III}$ represent the coordinate unit vectors for the ellipse with $\hat{III}$ being the longitudinal direction and $\hat{1}$, $\hat{2}$ and $\hat{3}$ represent the crystal coordinates, one has for the $< \bar{1}\bar{1}1 >$ band the relationship among vectors shown in Fig. 3.1. The axes $\hat{I}$ and $\hat{II}$ can be chosen anyway and have been chosen to make equal angles with the $\hat{3}$ axis.

The unit vectors are related by the following transformation matrix:

$$\overset{\leftrightarrow}{A}_3 = \overset{\leftrightarrow}{A}_{< \bar{1}\bar{1}1 >} \begin{bmatrix} b & -a & c \\ -a & b & c \\ -c & -c & c \end{bmatrix} , \qquad (3.44)$$

where

$$\begin{bmatrix} \hat{I} \\ \hat{II} \\ \hat{III} \end{bmatrix} = \overset{\leftrightarrow}{A}_3 \begin{bmatrix} \hat{1} \\ \hat{2} \\ \hat{3} \end{bmatrix} \qquad (3.45)$$

and

$$c = \frac{1}{\sqrt{3}} ,$$

$$b = \frac{\sqrt{3} + 1}{2 \sqrt{3}} ,$$

$$a = \frac{\sqrt{3} - 1}{2 \sqrt{3}} . \qquad (3.46)$$
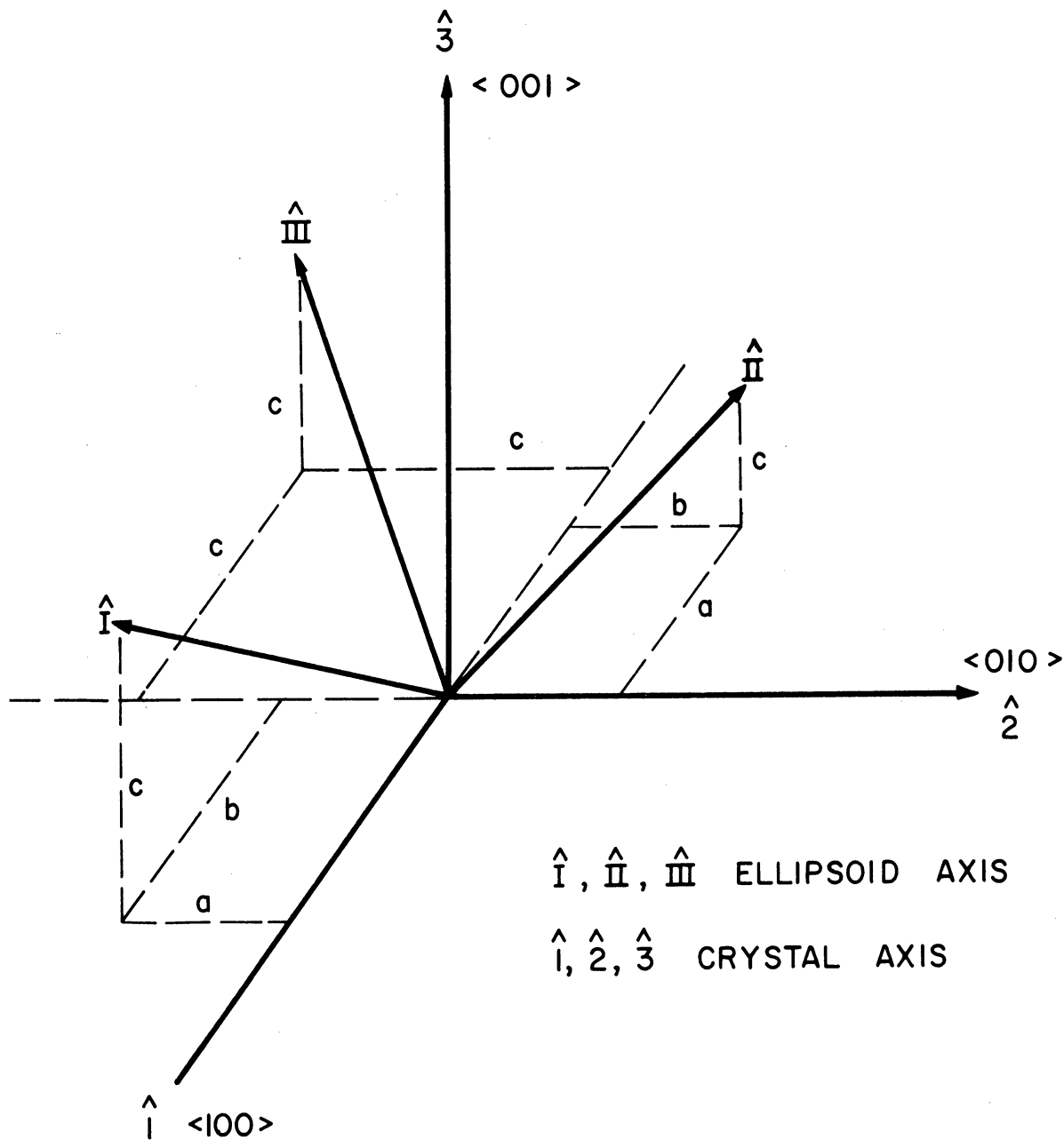
FIG. 3.1 ELLIPSOID AXIS FOR THE $< \bar{1}\bar{1}1 >$ ENERGY BAND.

For the other ellipsoids similarly oriented

$$
\hat{A}_1 = \hat{A}_{<111>} = \begin{bmatrix} -b & a & c \\ a & -b & c \\ c & c & c \end{bmatrix} , \tag{3.47}
$$

$$
\hat{A}_2 = \hat{A}_{<\bar{1}11>} = \begin{bmatrix} -a & -b & c \\ b & a & c \\ -c & c & c \end{bmatrix} , \tag{3.48}
$$

$$
\hat{A}_4 = \hat{A}_{<1\bar{1}1>} = \begin{bmatrix} a & b & c \\ -b & -a & c \\ c & -c & c \end{bmatrix} . \tag{3.49}
$$

It is easily shown that this is a unitary transformation and $\hat{A}^T = \hat{A}^{-1}$.

The current density in the crystal coordinate system due to one band is then given by

$$
\vec{J}^i = \hat{A}_i^{-1} \vec{J}_i' , \tag{3.50}
$$

where $\vec{J}_i'$ is the current density of the ith band in its own coordinate

system and

$\vec{J}^i$ is the current density of the ith band in the crystal coordinate

system.

Thus the total current is the sum over bands for noninteracting bands.

$$
\vec{J} = \sum_{i=1}^{4} \hat{A}_i^{-1} \vec{J}_i' . \tag{3.51}
$$

The $\vec{J}_i'$'s are given by Eq. 3.39 when $\vec{E}$ and $\vec{B}$ are expressed in the coordinate system of the band. It is necessary to transform Eq. 3.39 into the crystal coordinate system. The fields in the crystal coordinates are given by

$$\vec{B} = \overset{\leftrightarrow}{A}_i^{-1} \vec{B}_i$$

and

$$\vec{E} = \overset{\leftrightarrow}{A}_i^{-1} \vec{E}_i \quad . \tag{3.52}$$

Consequently for Eq. 3.39 used in Eq. 3.50,

$$\vec{J}^i = \overset{\leftrightarrow}{A}_i^{-1} \vec{J}_i' = \frac{-q}{4\pi^3 \hbar^2} \int \overset{\leftrightarrow}{A}_i^{-1} \nabla_k \mathcal{E} \left\{ \overset{\leftrightarrow}{A}_i \overset{\leftrightarrow}{A}_i^{-1} \vec{V}_i \right.$$

$$- q \left[\overset{\leftrightarrow}{\tau} \left(\overset{\leftrightarrow}{A}_i \overset{\leftrightarrow}{A}_i^{-1} \vec{V} \mu \right) \right] \times \overset{\leftrightarrow}{A}_i \overset{\leftrightarrow}{A}_i^{-1} \vec{B}$$

$$+ q^2 \left(\overset{\leftrightarrow}{A}_i \overset{\leftrightarrow}{A}_i^{-1} \vec{V} \cdot \overset{\leftrightarrow}{A}_i \overset{\leftrightarrow}{A}_i^{-1} \vec{B} \right) \left(\alpha \overset{\leftrightarrow}{A}_i \overset{\leftrightarrow}{A}_i^{-1} \vec{B} \right) \right\} \cdot \nabla_k \mathcal{E} \frac{\partial f_0}{\partial \mathcal{E}} \left[1 \right.$$

$$\left. + q^2 \left(\alpha \overset{\leftrightarrow}{A}_i \overset{\leftrightarrow}{A}_i^{-1} \vec{B} \right) \cdot \overset{\leftrightarrow}{A}_i \overset{\leftrightarrow}{A}_i^{-1} \vec{B} \right]^{-1} d^3k \quad . \tag{3.53}$$

Recall that

$$\nabla_k \mathcal{E} = \hbar^2 \overset{\leftrightarrow}{\mu} \left(\vec{k} - \vec{k}^j \right) \quad . \tag{3.25}$$

Let $\vec{k}' = \vec{k} - \vec{k}^j$, then $d\vec{k}' = d\vec{k}$ and $\vec{k} = \overset{\leftrightarrow}{A}_i^{-1} \vec{k}_i$. Consequently

$$\vec{J}^1 = \frac{-q}{4\pi^3 \hbar^2} \int \tilde{A}_i^{-1} \hbar^2 \tilde{\mu} \tilde{A}_i \tilde{A}_i^{-1} \vec{k}_i \left\{ \tilde{A}_i \vec{V} \right.$$

$$- q [\tilde{A}_i \tilde{A}_i^{-1} \tilde{\tau} (\tilde{A}_i \vec{V} \tilde{A}_i \tilde{A}_i^{-1} \tilde{\mu})] \times \tilde{A}_i \vec{B}$$

$$+ q^2 (\tilde{A}_i \vec{V} \cdot \tilde{A}_i \vec{B})(\tilde{\alpha} \tilde{A}_i \vec{B}) \left. \right\} \cdot \tilde{A}_i \tilde{A}_i^{-1} \hbar^2 \tilde{\mu} \tilde{A}_i \tilde{A}_i^{-1} \vec{k}_i \frac{\partial f_o}{\partial \mathcal{E}} [1$$

$$+ q^2 (\tilde{\alpha} \tilde{A}_i \vec{B}) \cdot (\tilde{A}_i \vec{B})]^{-1} d^3 k_i . \qquad (3.54)$$

Define

$$\tilde{\mu}_i = \tilde{A}_i^{-1} \tilde{\mu} \tilde{A}_i ,$$

$$\tilde{\tau}_i = \tilde{A}_i^{-1} \tilde{\tau} \tilde{A}_i ,$$

$$\tilde{\alpha}_i = \tilde{A}_i^{-1} \tilde{\alpha} \tilde{A}_i , \qquad (3.55)$$

since $\tilde{\mu}$, $\tilde{\tau}$ and $\tilde{\alpha}$ are the same for each band. Also using the properties,

$$\tilde{A} \vec{E} \cdot \tilde{A} \vec{B} = \vec{E} \cdot \vec{B}$$

and

$$\tilde{A} \vec{E} \times \tilde{A} \vec{B} = \tilde{A} \vec{E} \times \vec{B} , \qquad (3.56)$$

one obtains

$$\vec{J}^1 = \frac{-q\hbar^2}{4\pi^3} \int \tilde{\mu}_i \vec{k} \left\{ \vec{V} - q [\tilde{\tau}_i \tilde{\mu}_i \vec{V}] \times \vec{B} \right.$$

$$+ q^2 (\vec{V} \cdot \vec{B})(\tilde{\alpha}_i \vec{B}) \left. \right\} \cdot \tilde{\mu}_i \vec{k} \frac{\partial f_o}{\partial \mathcal{E}} [1 + q^2 (\tilde{\alpha}_i \vec{B}) \cdot \vec{B}]^{-1} d^3 k . \qquad (3.57)$$

For all the bands the expression over i is summed. Then since $q = -e$
for electrons

$$\vec{J} = \frac{+e\hbar^2}{4\pi^3} \sum_{i=1}^{4} \int \overset{\leftrightarrow}{\mu_i} \vec{k} \left\{ \vec{V} + e \left[\overset{\leftrightarrow}{\tau_i} \overset{\leftrightarrow}{\mu_i} \vec{V} \right] \times \vec{B} \right.$$

$$\left. + e^2 (\vec{V} \cdot \vec{B}) (\overset{\leftrightarrow}{\alpha_i} \vec{B}) \right\} \cdot \overset{\leftrightarrow}{\mu_i} \vec{k} \frac{\partial f_o}{\partial \mathcal{E}} [1 + e^2 (\overset{\leftrightarrow}{\alpha_i} \vec{B}) \cdot \vec{B}]^{-1} d^3k \quad . \quad (3.58)$$

A similar expression can be obtained for the heat current density
for the many-valley model. Since $\mathcal{E}$ has a constant component this comes
in through the appearance of $\mathcal{E}$ as well as $\nabla_k \mathcal{E}$ under the integral sign.
Consequently

$$\vec{Q}^i = \overset{\leftrightarrow}{A_i^{-1}} \mathcal{E}^i \frac{\vec{J}_i'}{q} - \frac{\overset{\leftrightarrow}{A_i^{-1}}}{4\pi^3 \hbar^2} \int \frac{\hbar^2}{2} (\vec{k}_i \cdot \overset{\leftrightarrow}{\mu} \vec{k}_i) \hbar^2 \overset{\leftrightarrow}{\mu} \vec{k}_i \left\{ \vec{V}_i - q \left[\overset{\leftrightarrow}{\tau} \overset{\leftrightarrow}{\mu} \vec{V}_i \right] \times \vec{B}_i \right.$$

$$\left. + q^2 (\vec{V}_i \cdot \vec{B}_i) (\overset{\leftrightarrow}{\alpha} \vec{B}_i) \right\} \cdot \hbar^2 \overset{\leftrightarrow}{\mu} \vec{k}_i \frac{\partial f_o}{\partial \mathcal{E}} [1 + q^2 (\overset{\leftrightarrow}{\alpha} \vec{B}_i) \cdot \vec{B}_i]^{-1} d^3k \quad . \quad (3.59)$$

This yields for electrons

$$\vec{Q} = - \sum_{i=1}^{4} \frac{\mathcal{E}^i \overset{\leftrightarrow}{A_i^{-1}} \vec{J}_i'}{e} - \sum_{i=1}^{4} \frac{\hbar^4}{8\pi^3} \int (\vec{k} \cdot \overset{\leftrightarrow}{\mu_i} \vec{k}) \overset{\leftrightarrow}{\mu_i} \vec{k} \left\{ \vec{V} + e \left[\overset{\leftrightarrow}{\tau_i} \overset{\leftrightarrow}{\mu_i} \vec{V} \right] \times \vec{B} \right.$$

$$\left. + e^2 (\vec{V} \cdot \vec{B}) (\overset{\leftrightarrow}{\alpha_i} \vec{B}) \right\} \cdot \overset{\leftrightarrow}{\mu_i} \vec{k} \frac{\partial f_o}{\partial \mathcal{E}} [1 + e^2 (\overset{\leftrightarrow}{\alpha_i} \vec{B}) \cdot \vec{B}]^{-1} d^3k \quad . \quad (3.60)$$

Thus the heat current and electrical current densities have been evaluated
for the time independent case or for the d-c part of the time dependent
case for n-type germanium. A similar treatment can be made for n-type

silicon, except here the bands are located on the cube edges. This only involves a different transformation matrix. From these equations the d-c conductivity can be evaluated along with the so-called Hall conductivity.

3.6 Conclusions. This analysis serves as an introduction to a theoretical understanding of solid-state plasma instabilities. The evaluation of the time dependent distribution function and the resulting dispersion relation for electromagnetic waves will be continued under Contract AF33(615)-1553.

4. Radiation From Solids   (D. C. Hanson)

4.1 Introduction. A number of reports[1-4] have appeared in the literature in the past few years concerning bulk oscillations in semiconductors. However, for the most part, only experimental evidence of the various instabilities in bulk semiconductors has been presented. Under idealized conditions of transport, interaction, and geometry,

1. Larabee, R. D., Steele, M. C., "The Oscillistor-- New Type of Semiconductor Oscillation", Jour. Appl. Phys., vol. 31, No. 9, pp. 1519-1523; September, 1960.

2. Misawa, T., Yamada, T., "Microwave Observation of Carrier Behavior in Oscillistors", Japanese JAP, vol. 2, No. 1, p. 19; January, 1963.

3. Gunn, J. B., Microwave Observation of Current in III-V Semiconductors, vol. 1, pp. 88-91, Pergamon Press Inc., London; 1963.

4. Gunn, J. B., "Instabilities of Current in III-V Semiconductors", IBM Jour., pp. 141-159; April, 1964.

theoretical models have been developed to explain at least partially some types of instabilities[5-8].

Investigation during the past year has been concerned mainly with a type of instability which occurs in n-type GaAs and which has come to be called the Gunn effect[3,4]. Since until the latter part of this period no suitable explanation of the predominant mechanism for this instability had been set forward, a considerable portion of time was spent investigating possible mechanisms. The Correspondence in the Proceedings of the IEEE by Kroemer[6] pointing out the earlier work of Ridley and Watkins[7,8] revealed a theory which explains the establishment of a high field domain and movement through the crystal of this domain with its associated space charge at the boundary between high and low field regions. The movement of such a domain has been directly observed by Gunn[9].

It is evident, however, that in addition to the predominant type of instability which produces the Gunn effect in n-type GaAs, additional types of fundamentally important interaction mechanisms, which are

5. Glicksman, M., "Instabilities in Cylindrical Electron-Hole Plasma in Magnetic Field", Physical Review, vol. 124, No. 6, p. 1655-1664; December 15, 1961.

6. Kroemer, H., "Theory of the Gunn Effect", Proc. IEEE, vol. 52, No. 12, p. 1736; December, 1964.

7. Ridley, B. K., "Specific Negative Resistance in Solids", Proc. Phys. Soc., vol. 82, pp. 954-966; 1963.

8. Ridley, B. K., Watkins, T. B., "The Possibility of Negative Resistance Effects in Semiconductors", Proc. Phys. Soc., vol. 78, pp. 293-304; 1961.

9. Gunn, J. B., "Instabilities of Current and of Potential Distribution in GaAs and InP", Proc. of Internat'l. Conference on Semiconductor Physics, Paris; 1964.

potentially important for device applications, will occur in the bulk crystal. These can be studied individually in addition to investigating how they interact with the moving space-charge domains detected in Gunn effect experiments. Particularly important in this class are interaction of hot electrons with optical phonons, plasma oscillations and impurity scattering effects which occur in the far infrared region in polar crystals such as GaAs. One such process, i.e., stimulated emission of Bremsstrahlung radiation, was initially investigated and will be discussed in the following section.

Experiments demonstrating the existence of far infrared radiation and its dependence on current density and spectral distribution are presented. In addition, studies concerned with the nature of "ohmic" contacts on GaAs are presented in relation to the Gunn experiment.

4.2 Stimulated Emission of Bremsstrahlung Radiation. Marcuse[10,11] has presented an analysis of stimulated emission of Bremsstrahlung radiation. By utilizing certain of the quantum mechanical expressions of Heitler[12] for the scattering of a stream of electrons in a Coulomb field, Marcuse[10] develops expressions for the differential scattering cross section for emission and absorption of plane electron waves incident on the Coulomb field of a nucleus. By utilizing conservation of energy and momentum, along with certain simplifying assumptions, he shows that stimulated emission should exist if the direction of electron velocity is

10. Marcuse, D., "Stimulated Emission of Bremsstrahlung", B.S.T.J., vol. XLI, No. 5, pp. 1557-1571, September, 1962.

11. Marcuse, D., "A Further Discussion of Stimulated Emission of Bremsstrahlung", B.S.T.J., vol. XLII, No. 2, pp. 415-430; March, 1963.

12. Heitler, W., The Quantum Theory of Radiation, Third Edition, Oxford; 1954.

within an angle of 54 degrees of the electric field vector stimulating the radiation and that absorption exists for larger angles.

By defining the loaded Q of the cavity in which the radiation occurs by[13]

$$Q_L = \frac{\omega NV}{n'} \; , \qquad\qquad (4.1)$$

where ω = angular frequency,

  N = photon density,

  V = volume of cavity and

  n' = number of photons dissipated per second to satisfy the condition for oscillation,

Marcuse derives the following equation for the onset of the oscillation[13], with electron velocities parallel to the E vector stimulating the emission,

$$N_e \left(\frac{N_n}{V} \right) = \frac{\pi \; \epsilon_o^3 \; m_e^3 \; v^4 \; f^3}{4 \; e^6 \; Z^2 \; Q_L \left[\left(\ln \frac{2 \; m_e v^2}{hf} \right) - 1 \right]} \; , \qquad (4.2)$$

where N_e = number of electrons penetrating a unit area per unit time,

  N_n = ion concentration,

  V = volume of specimen,

  v = electron velocity,

  f = frequency of oscillation,

  e = electronic charge,

  m_e = electronic effective mass,

---

13. Marcuse, D., "Stimulated Emission of Bremsstrahlung", B.S.T.J., vol. XLI, No. 5, p. 1566; September, 1962.

$$Z = \text{atomic number of nucleus,}$$

$$h = \text{Plank's constant and}$$

$$\epsilon_o = \text{dielectric constant of material.}$$

Equation 4.2 can be applied to determine the condition for oscillation in a thin slab of bulk GaAs with velocity (v), volume (V), and frequency (f).

The following parameter values will be used:

$$v = 10^7 \text{ cm sec}^{-1},$$

$$f = 10^{12} \text{ cps,}$$

$$Z = 22 \text{ (average for Ga and As),}$$

$$Q_L = 10^3,$$

$$m_e = 0.034 \ m_o{}^{14}, \text{ (n-type GaAs),}$$

$$V = (4 \times 10^{-2} \text{ cm}) \times \pi \ (10^{-1} \text{ cm})^2/4 = 3.14 \times 10^{-4} \text{ cm}^3,$$

$$\epsilon_o = 12.5, \text{ dielectric constant of GaAs}^{15}.$$

Then for the start of oscillation at 10^{12} cps one must have

$$N_e \left(\frac{N_n}{V} \right) \Bigg| = \frac{4.24 \times 10^{32}}{\text{cm}^3} \times \left(\frac{1}{\text{cm}^2 \text{ sec}} \right) . \tag{4.3}$$

If a current density of 100 amperes/cm² is applied, the required ion density for oscillation is

$$\left(\frac{N_n}{V} \right) = 1.2 \times 10^{11} \frac{\text{nuclei}}{\text{cm}^3} . \tag{4.4}$$

Marcuse calculates in his second paper[11] the available power from this mechanism using fourth-order perturbation theory. He assumes a

14. Bude, R. H., Photoconductivity in Solids, J. Wiley and Sons, Inc., New York, p. 209; 1960.

15. Hilsum, C., Rose-Innes, A. C., Semiconducting III-V Compounds, Pergamon Press, New York, p. 181; 1961.

model for the nucleus which allows electron shielding by assuming a scattering potential $V = -Ze^2 \epsilon^{-\gamma r}/r$, where γ is the exponential shielding constant. He obtains the result that the available radiated power should go as the fifth power of frequency. His expression for the radiated power[16] (with one correction) is

$$P_r = \frac{2\pi^2 h^2 f^5 V}{e^2 v^2} \left(\frac{1}{Q_L} - \frac{1}{Q_i} \right) \left[1 - \frac{\pi m^3 v^4 f^3 V}{4 e^6 Z^2 Q_L N_n N_e \ln\left(\frac{2}{\sqrt{\epsilon^2 + \eta^2}} \right)} \right] ,$$

$$(4.5)$$

where all quantities are as previously noted and in addition

$\qquad Q_i$ = unloaded Q of the cavity, $Q_i \gg Q_L$,

$\qquad \epsilon$ = hf/mv^2 and

$\qquad \eta$ = $e^2 Z^{1/3}/hv$.

Using this relationship and the parameter values previously used for the small GaAs specimen gives between 0.1 watt and 1.0 watt of power available at 1000 Gc. Marcuse points out that the limiting factor in achieving such power at frequencies above 100 Gc is the high required product of $N_e N_n$ for oscillation. However, this limitation does not hold for a semiconductor such as GaAs with large impurity concentrations where large electron current concentrations can be tolerated and where $v \ll c$.

---

16. Marcuse, D., "A Further Discussion of Stimulated Emission of Bremsstrahlung", B.S.T.J., vol. XLII, No. 2, p. 426; March, 1963.

A recent paper by Musha and Yoshida[17] is apparently the first publication to recognize the significance of Marcuse's theory[10, 11]. This paper points out the conflict of theories as to whether radiation can be generated by ionized impurity scattering and notes the significance of scattering parallel with the applied electric field for stimulated emission of radiation. Isotropic scattering will always absorb radiation.

By expanding the theory to a Maxwellian distribution of velocities along the applied electric field and by considering the net conductivity of the scattering region, Musha and Yoshida[17] show that the region develops a negative conductance if the ratio of the average drift velocity to the thermal spread in velocities is greater than 0.8 for the parameter values considered. For "hot electron" conduction in a semiconductor where a scattering limited (or otherwise limited) drift velocity occurs (as pointed out in the original work by Ryder[18]) this condition should be satisfied with saturated drift velocities in the range of 10^7 cm/sec. It is pointed out further that this effect is due to electron scattering from ions and is not due to two-stream instabilities or space-charge effects.

A similar type of analysis of electrostatic instabilities in drifted one-component solid-state plasmas by McCumber and Chynoweth[19] produced the following conclusions for the case where ionized-impurity scattering is the dominant scattering mechanism. The plasma presents a negative

17. Musha, T., Yoshida, F., "Negative Absorption Due to Coulomb Scattering of an Electron Stream", Physical Review, vol. 133, No. 5A, pp. 1303-1307; March 2, 1964.

18. Ryder, E. J., "Mobility of Holes and Electrons in High Electric Fields", Physical Review, vol. 90, pp. 766-769; June 1, 1953.

19. McCumber, D. E., Chynoweth, A. G., "Electrostatic Instabilities in Drifted One-Component Solid-State Plasmas", The Am. Phys. Soc. 6th Annual Meeting, Plasma Physics Division, New York, N. Y., PN 6; November 4-7, 1964.

resistance with unstable plasma oscillations when the average drift velocity v_o exceeds a critical velocity v_c. For effect mass m^*, the critical v_c is given by $(1/2)\ m^*\ v_c^2 = 1.2\ (kT + \hbar\omega_p)$. This negative resistance near the plasma frequency ω_p will be masked in materials with significant acoustic or optical phonon scattering.

These observations may be pertinent to the initial evaluation of the radiation spectrum observed in GaAs in the far infrared as presented in the experimental section of this report.

4.3 Scattering Effects in Semiconductors. It is apparent from a search of the literature that mobility calculation and measurement has been the predominant method of determining the validity of any scattering theory in semiconductors. The theory which has evolved from mobility studies can be utilized, however, to gain insight into the generation of radiation through scattering since the mobility depends inversely on the scattering cross section.

It is necessary to consider scattering both from the lattice (i.e., phonon scattering) and impurity scattering. Depending on the relative purity of the specimen, the temperature range and the applied electric field, either mechanism may predominate. In relatively pure specimens of III-V semiconductor compounds, mobility theory is well correlated with experiment[20]. It has been determined that in the range above 200°K, the mobility of relatively pure GaAs is accounted for by polar lattice scattering[20].

Impurity dominated scattering is not well understood[20]; especially at temperatures above 300°K and with high electric fields("hot electron

---

20. Ehrenreich, H., "Band Structure and Transport Properties of Some III-V Compounds", Jour. Appl. Phys., Sup. to vol. 32, pp. 2155-2166; October, 1961.

scattering"). Considerable discrepancies from impurity scattering mobility theory have been reported. In the initial report[21] of high-field impurity scattering in germanium, experiments justify theory only if the rate of energy loss was taken as being several times higher than that of the assumed model. More recently, it has been reported[22] that large variations in mobility occur in III-V semiconductors with the same carrier concentration and temperatures above 300°K due to an unexplained impurity scattering mechanism, although the fit is good at 78°K. A very recent calculation[23] of the high frequency resistivity in degenerate semiconductors indicates that the resistivity due to electron-phonon interaction is less than 20 percent of that due to electron-ion collisions for electron energies up to the Fermi energy. The crossover in the effectiveness of phonon and impurity scattering occurs for electron energy about six times the Fermi energy.

Sclar[24] has reported an analysis of ionized impurity scattering in which he considers the effects of attractive, repulsive, and in a companion paper, neutral impurities. Although his results are only valid at relatively low temperatures and low fields, they are enlightening because they show that resonances in the scattering cross section occur for attractive impurity scattering but not for repulsive impurity

21. Conwell, E. M., "High Field Mobility in Ge with Impurity Scattering Dominant", Physical Review, vol. 90, pp. 769-772; June 1, 1953.

22. Weisberg, L. R., Blanc, J., "Evidence for a Mobility Killer in GaAs, InAs, and InP", Bull. of Am. Phys. Soc., p. 62; January 27, 1960.

23. Tzoar, N., "High-Frequency Resistivity of Degenerate Semiconductors", Physical Review, vol. 133, pp. 1213-1214; February 17, 1964.

24. Sclar, N., "Ionized Impurity Scattering in Nondegenerate Semiconductors", Physical Review, vol. 104, pp. 1548-1561; December 15, 1956.

potentials. Predominately attractive scattering occurs with electrons as majority carriers and ohmic contacts in the n-type GaAs specimens.

It is predicted[25] that the lowest infrared absorption lines in germanium and silicon are due to impurity bands and that the Raman vibrational, optical phonon modes are within four percent of the observed absorption frequencies.

The infrared absorption spectrum of GaAs has been reported[26] along with the actual frequencies of the individual vibrational modes obtained from neutron spectrometry[27]. The vibrational modes occur in the range 2×10^{12} to 2×10^{13} cps (15 μ to 150 μ) which may be significant for explaining the sharp decrease in the observed infrared spectrum near 16 μ presented in the experimental section of this report.

4.4 <u>Experimental Program</u>. Based on the above theory concerning the possibility of detecting an infrared radiation mechanism in addition to Gunn's observation of a microwave spectrum from bulk n-type GaAs, a mounting procedure for the crystal, radiation mount and experimental procedure was devised to allow simultaneous observation of infrared and microwave radiation. The following sections will describe these programs in detail.

4.4.1 <u>GaAs Structures</u>. The GaAs crystals were obtained from Texas Instruments since it was possible to obtain bulk devices with contacts applied. A program has since been initiated to apply our own

25. Lax, M., Burstein, E., "Infrared Lattice Absorption in Ionic and Homopolar Crystal", <u>Physical Review</u>, vol. 97, pp. 39-52; January 1, 1955.

26. Cochran, W., Fray, S. J., et. al., "Lattice Absorption in GaAs", <u>Jour. Appl. Phys.</u>, Sup. to vol. 32, pp. 2102-2106; October, 1961.

27. Waugh, J. L. T., Dolling, G., "Crystal Dynamics in GaAs", <u>Physical Review</u>, vol. 132, pp. 2410-2412; December 15, 1963.

contacts since, as will be discussed later, the former type of contacts did

not prove suitable for observation of microwave instabilities of the type

reported by Gunn[3,4].

The crystals obtained from Texas Instruments have the following

characteristics:

Table 4.1

GaAs Structures

No.	Material Type	Carrier Concentration	Dopant	Resistivity (Ω-cm)
1	n-type	$5 \times 10^{16}/cm^3$	not doped	0.10
2	n-type	$1 \times 10^{17}/cm^3$	tellurium	0.01
3	n-type	$1 \times 10^{18}/cm^3$	tellurium	0.0008
4	p-type	$1 \times 10^{17}/cm^3$	zinc	0.05
5	p-type	$1 \times 10^{18}/cm^3$	zinc	0.027

These crystals are 0.080 inch x 0.080 inch x 0.004 inch volume and

are first plated on the two large area surfaces with rhodium to allow the

subsequent application of indium-tin solder to adhere. The In-Sn contacts

as initially applied are not ohmic since it is necessary to alloy them to

form a suitable contact with the crystal. In addition, the lower limits

in the carrier concentrations noted in Table 4.1 are the lowest available

from Texas Instruments; to go to lower carrier concentrations would require

compensation of the material. The above types of contacts are not applied

to such compensated material.

It became apparent after mounting and evaluating over 20 devices of

the above types that the instability observed by Gunn was not being

developed with this type of contact. In the reported cases[3,4,9,28] either diffused tin or tin over electroless nickel contacts are used, whereas in this case a layer of indium-tin solder is placed over rhodium-plated crystal and ohmic contacts are subsequently formed by heating in the mount.

A recent paper by Gunn[9], in which a moving region of high electric field has been demonstrated to be associated with the occurrence of a radiation threshold, states that "In GaAs the nature of the instability is not affected by the nature of the contacts". However, it was demonstrated experimentally[9] that a narrow (≈ 30 μ), high field (≈ 2 x 10^4 volts/cm) region leaves the cathode at threshold and travels with the electron velocity at nearly constant amplitude through the crystal. It may be that for the types of contacts used in the reported experiments[4,9] the nature of the contact is immaterial; however, it seems evident that a crystal-contact boundary condition establishes, at least in part, the threshold condition.

To form small area ohmic contacts (i.e., near point contacts) on rhodium plated GaAs surfaces covered with a thin layer of InSn solder, Texas Instruments discharges a capacitor through the contact to form an ohmic contact with a transition region similar to those obtained by alloy-ing. However, they do not know precisely what temperature is reached during this process in the contact region nor is the pulse duration known since the resistance changes during the pulse. Thus for the larger area contact surfaces required in these experiments, investigation of optimum alloying conditions is required not only to achieve ohmic contacts but also to determine crystal boundary conditions for radiation. With an

28. Hakki, B. W., Irvin, J. C., "C. W. Microwave Oscillations in GaAs", Proc. IEEE, vol. 53, No. 1, p. 80; January, 1965.

S.K.L. nanosecond pulser, it is possible to examine radiation threshold and pulse resistance conditions without altering the pulse and d-c resistance of the GaAs structures.

Initial experiments indicated the existence of appreciable junction capacitance before the crystal was alloyed. It is desirable to obtain a quantitative measure of this effect as a function of junction potential. This was done on both a pulsed basis and through microwave impedance measurements with successive alloying.

Since the mount in which the crystals are held was designed to be a matched 50 ohm line with the crystals just above the shorted end of the transmission line, it is possible to accurately measure the small-signal microwave impedance of the GaAs device. By varying the bias during these measurements the effect of any junction capacitance becomes readily apparent.

Previous to alloying, the d-c resistance of the GaAs device is typically 50,000 ohms. Figure 4.1 shows the measured pulse voltage-current characteristics of device No. 20 (5×10^{16} carriers/cm^3, n-type) before alloying. This characteristic was measured with 10 nsec pulses so as not to affect the crystal contact conditions. It is noted that the characteristic is quite nonlinear with the pulse resistance varying from considerably more than 50 Ω at low voltages to considerably less than 50 Ω at an applied pulse voltage of 70 volts.

Figure 4.2a shows the pulse resistance characteristic at -24.5 volts applied during a 10 nsec pulse. This voltage corresponds to the point of intersection of the crystal I-V curve and that of a linear 50 ohm termination (two Tektronix 017-044 10 db pads) as shown in Fig. 4.1. It is apparent from Fig. 4.2a that the unalloyed crystal differs from the
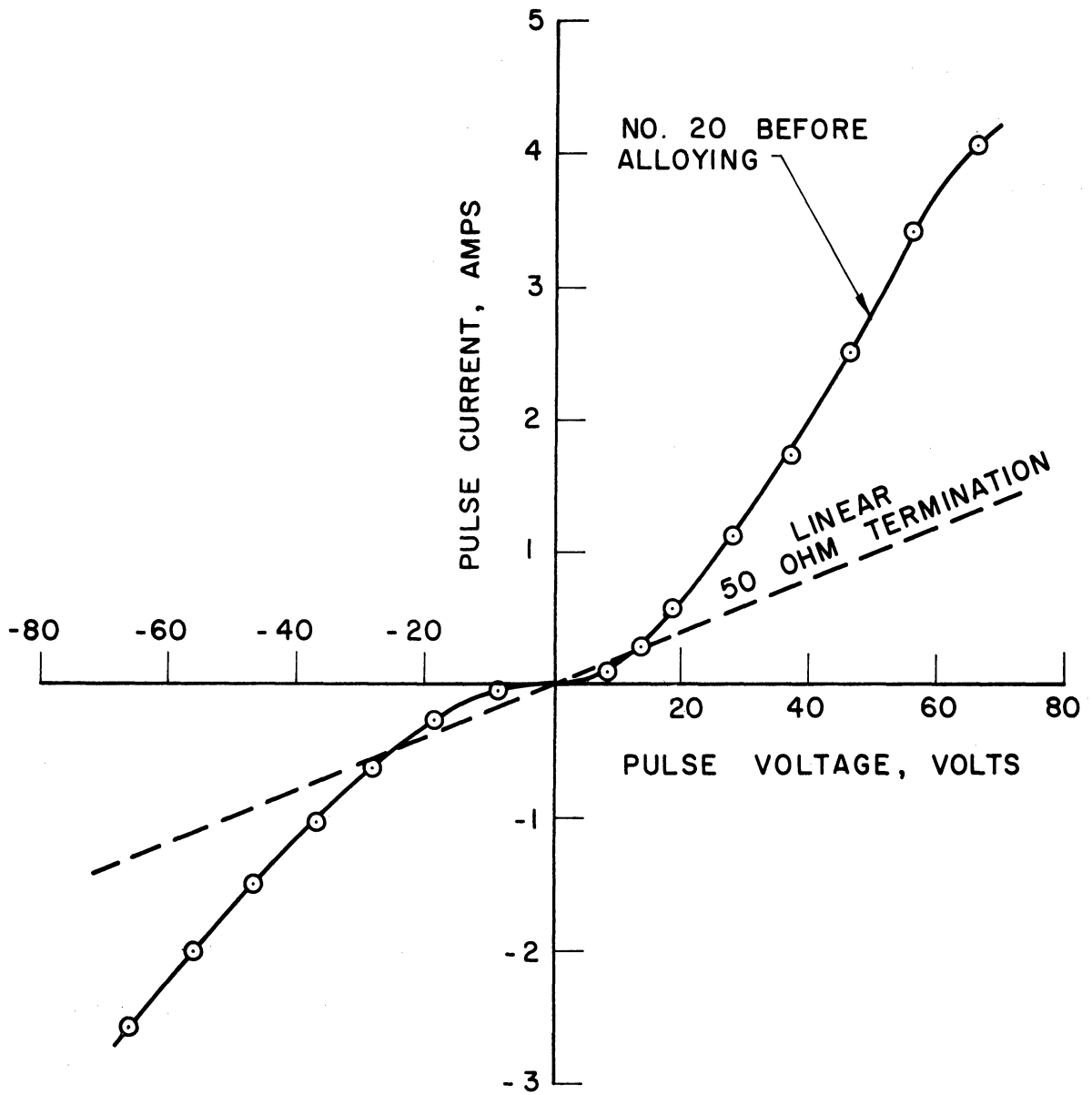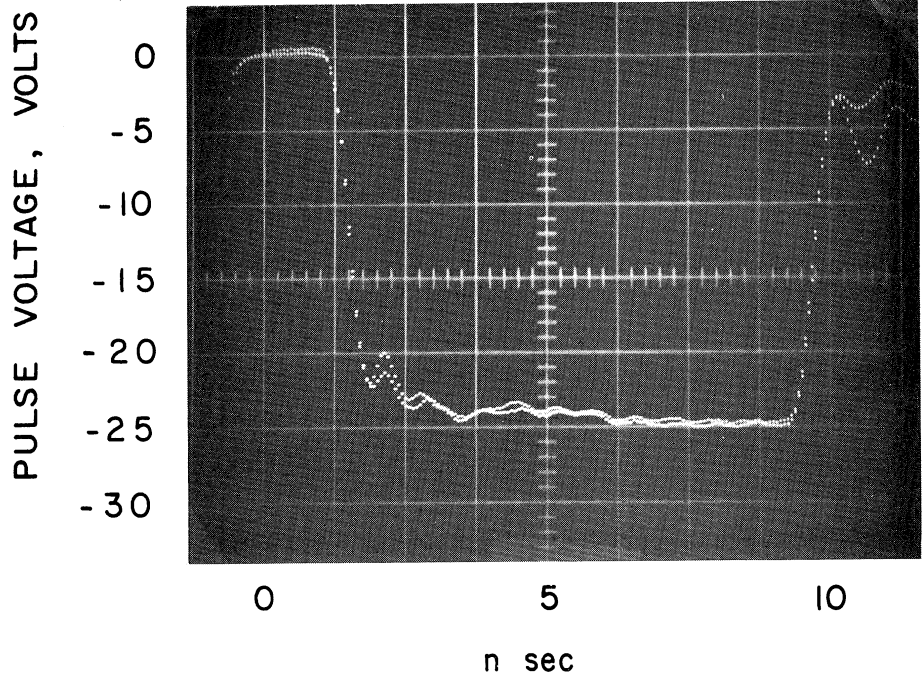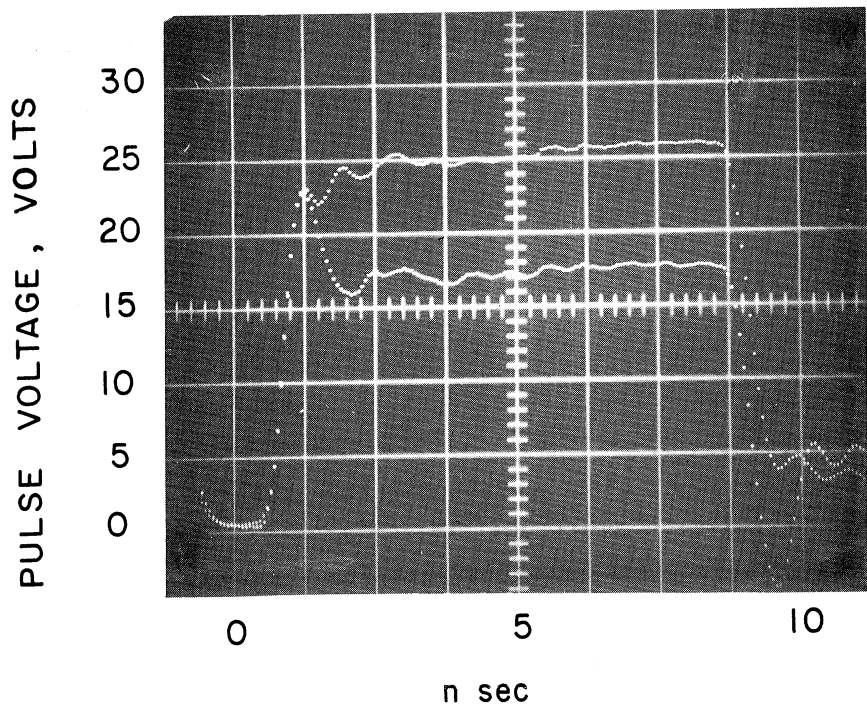
FIG. 4.1 PULSE CURRENT-VOLTAGE CHARACTERISTICS OF GaAs STRUCTURE
BEFORE ALLOYING.

FIG. 4.2 COMPARISON OF GaAs CRYSTAL-VOLTAGE CHARACTERISTIC WITH
50 OHM TERMINATION.

50 ohm termination at this point only in that it has somewhat more over-shoot due to its capacitive reactance.

Figure 4.2b shows the same two characteristics with 24.5 volt pulses applied. The 24.5 volt pulse is measured with the 50 ohm termination. The crystal voltage pulse rises to the same initial value due to the rise time of the pulse but drops to 17.5 volts within 1 nsec. This corresponds to the lower resistance in the positive voltage direction shown in Fig. 4.1.

Figure 4.3 shows the 800 mc impedance of GaAs devices No. 20 and No. 21 as a function of bias both before and after alloying. Bias was applied with a 45 volt battery and 100 K ohm potentiometer. A series current limiting resistor of 10 K ohm was used.

The impedance curve of device No. 20 before alloying corresponds to the pulse data in Fig. 4.1. It is noted in Fig. 4.3 that there is consider-able impedance variation as the negative bias is increased to five volts. The increase in the capacitive reactance along a nearly constant resist-ance circle with increased negative bias is due to the decrease in the total junction capacitance of two contacts.

It is interesting to note that with small positive bias the impedance of the structure backtracks on a constant resistance circle over the negative bias impedance curve (corresponding to an initial decrease in total contact capacitance), but as the positive bias exceeds 2.5 volts the total capacitance exceeds that at zero bias and the impedance shifts to smaller capacitive reactance.

After alloying device No. 20 with -0.44 ampere current for five seconds, a decided shift in impedance to the 0.5 normalized resistance circle occurs with a considerable decrease in capacitive reactance. It is interesting to note that since a negative alloying current is used, the
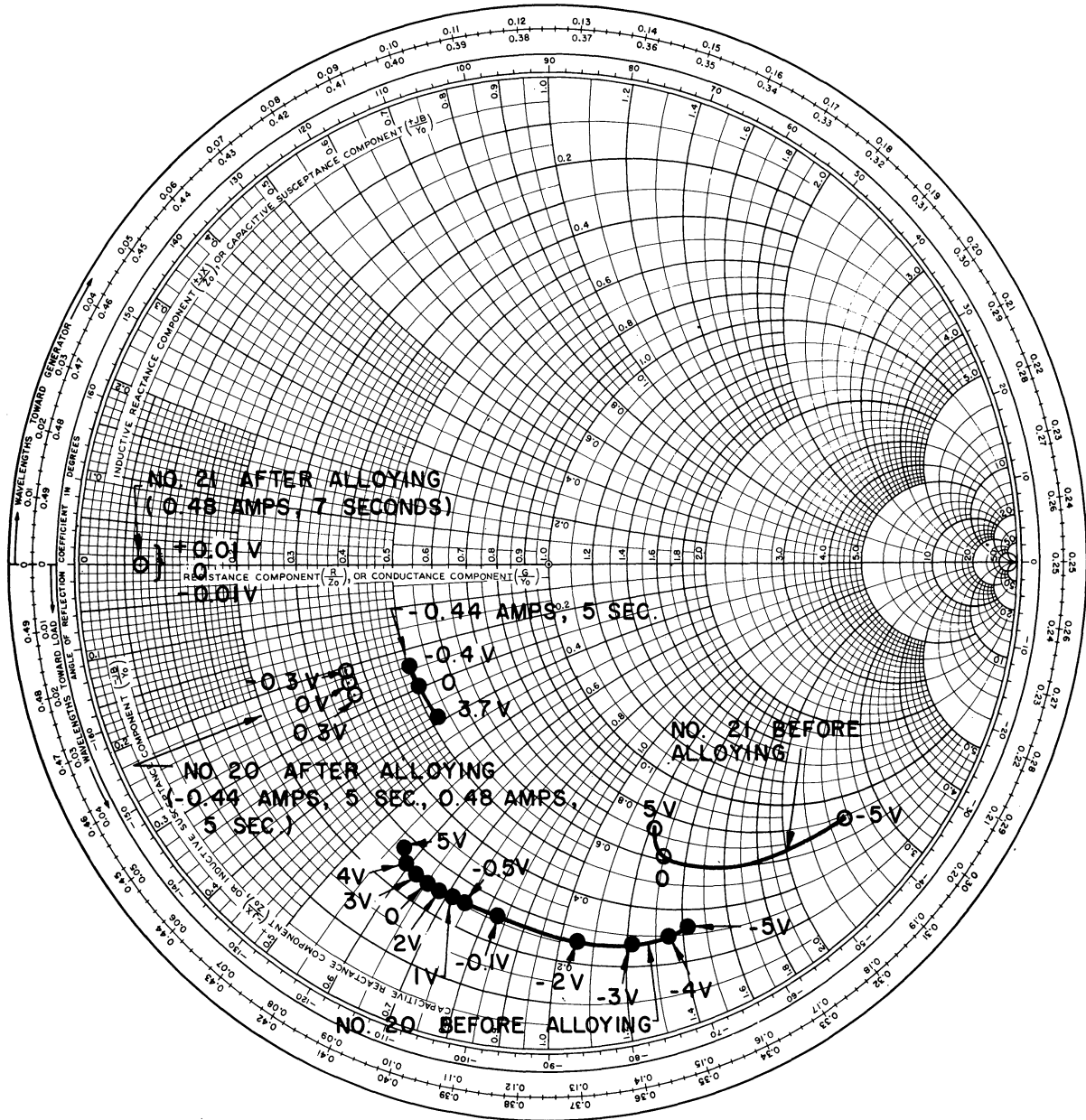
FIG. 4.3 800 MC IMPEDANCE OF TWO GaAs STRUCTURES BEFORE AND AFTER
ALLOYING AS A FUNCTION OF BIAS VOLTAGE.

capacitive reactance with negative bias is now less than with positive

bias, i.e., there is a reversal in capacitance change with bias from that

shown in the impedance characteristic before alloying. After a second

alloying with the opposite current direction, i.e., 0.48 ampere for five

seconds, a further shift occurs, reducing the impedance variation with

bias. With two successive alloying operations of five seconds each, the

device resistance of No. 20 never becomes completely resistive.

The other characteristic shown in Fig. 4.3 is that of device No. 21.

Before alloying its impedance variation is similar to that of No. 20.

However, in this case No. 21 was alloyed with 0.48 ampere current for

seven seconds. As shown in Fig. 4.3 the total device impedance becomes

purely resistive from this one alloying operation, producing a small-signal

microwave resistance of $R_s \big|_{800 \text{ mc}} = 3.29$ ohms. The d-c resistance as measured

with an ohmmeter is $R_s \big|_{d-c} = 3.00$ ohms. There is no variation with bias over

the range allowed by the bias potentiometer and current limiting resistor.

Device No. 21 as alloyed should be suitable for observation of

microwave instabilities provided only purely resistive ohmic contacts are

required. However, subsequent pulse investigation established that no

such instability occurs although such an instability is readily detectable

in the same mount under the same conditions with a GaAs device mounted on

the same heat sink arrangement by IBM[29]. For this reason a program has

been initiated to apply our own contacts in this laboratory.

---

29. "Microwave Generator Uses Thin GaAs Slab", Electronics, p. 147;
    October, 1964.

4.4.2 <u>Infrared Radiation Mount and Experiments</u>. Initial

consideration was given to obtaining a suitable detector in the 100 μ to

1000 μ region. A mount was constructed, as shown in Fig. 4.4, with

symmetrical coaxial input and output lines and tunable cavities which will

allow an InSb photoconductive detector to be placed at one focus of a

confocal elliptical radiation plate while the GaAs emitting structure is

at the other focus.

It was considered advisable in the initial experiments, however, to

use a detector which does not require cooling and whose use is well

established. The logical choice is the Golay cell which has been used

successfully to detect radiation from the ultraviolet out to the 50 Gc

region. As shown schematically in Fig. 4.4, the Golay cell has a radiation

absorbing membrane which has a mirror surface on its reverse side. A lens

focuses an internal light beam onto this surface which reflects the beam

to a photodetector. As radiation is absorbed, the membrane vibrates due

to gas collision, thus modulating the internal light beam. One potential

limitation of the Golay cell is its response time to 15 msec which is

incompatible with the nanosecond pulses initially required in the Gunn

effect experiments.

To establish the existence of submillimeter and far infrared

radiation, a 0.120 inch x 0.120 inch cross-section waveguide, 0.600 inch

long, is coupled into the coaxial microwave cavity as shown in Fig. 4.4.

Since this waveguide section is cut off below 50 Gc, radiation as high

in frequency as 6 Gc will be reduced by at least 100 db (about 27 db for

every length a = 0.120 inch of the waveguide). This, along with the low

frequency response limit of about 50 Gc for the Golay cell, insures that

any observed radiation is at least above 50 Gc with no monochrometer
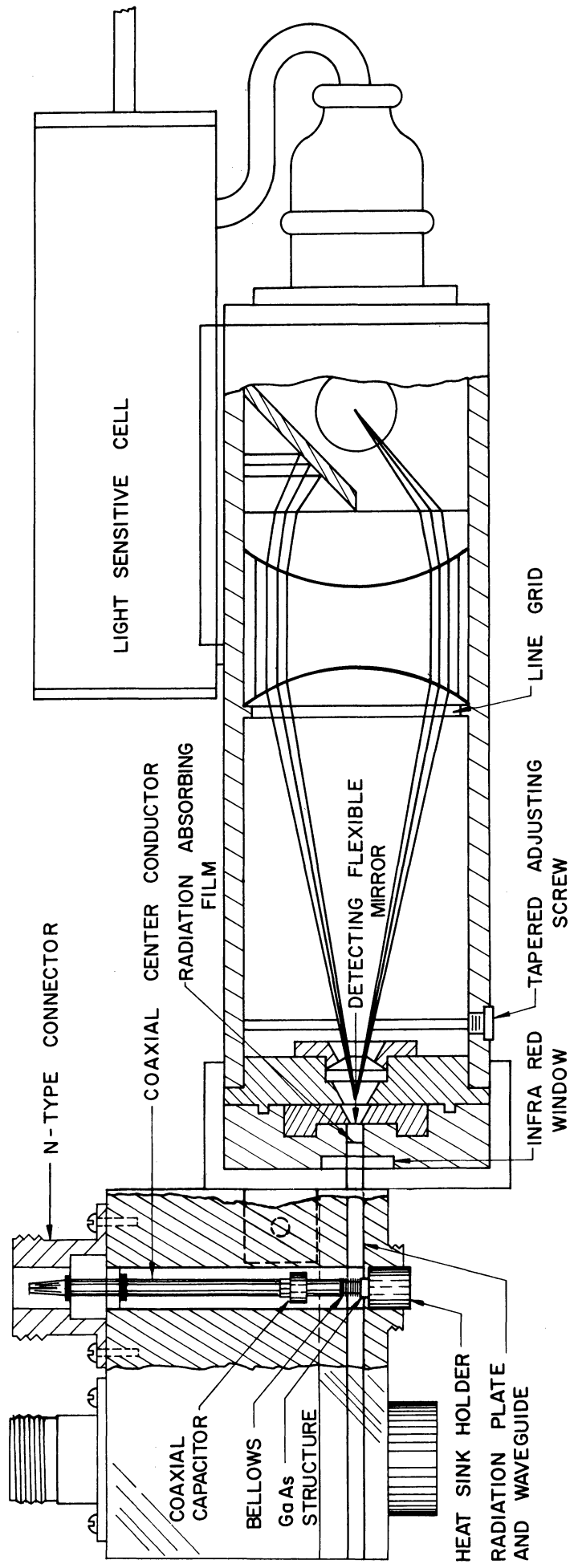
between the source and Golay cell.

LIGHT SENSITIVE CELL

N-TYPE CONNECTOR

COAXIAL CENTER CONDUCTOR

RADIATION ABSORBING FILM

DETECTING FLEXIBLE MIRROR

LINE GRID

TAPERED ADJUSTING SCREW

INFRA RED WINDOW

COAXIAL CAPACITOR

BELLOWS

GaAs STRUCTURE

HEAT SINK HOLDER

RADIATION PLATE AND WAVEGUIDE

FIG. 4.4 COAXIAL SEMICONDUCTOR RADIATION MOUNT AND GOLAY CELL.

90

In the initial experiments to ascertain the existence of far infra-
red radiation, a two megohm impedance, four-stage transistorized preampli-
fier was designed with a flat response from about 15 cps to above 100 kc.
This was followed by a low-pass filter network to peak the overall response
of the preamplifier at 20 cps with a voltage gain of 100. This drastically
reduced the noise output of the photodetector high-impedance transistor
preamplifier circuits.

A mercury wetted relay circuit is used to switch up to 20 amps of
current at a 10-20 cps rate, with a 50 percent duty cycle, directly into
the GaAs device. With a good heat sink arrangement, such long current
pulses are possible without heating damage to the crystal.

With the latter 20 cps square-wave modulated current source,
radiation was initially detected in the frequency range above 50 Gc
using the circuit shown in Fig. 4.5. The preamplifier output increased
to 70 mv peak-to-peak with 20 amperes of current being switched into a
0.048 inch x 0.056 inch structure (J = 1150 amps/cm^2.) However, since
the Golay cell has a flat frequency response it is necessary to utilize
a spectrometer to determine the radiation spectrum.

A Perkin-Elmer (Model 301) Far Infrared Double Beam Spectrometer
was initially used to evaluate the frequency spectrum of the radiation.
To utilize this instrument the internal globar and mercury H-4 sources
were switched off and instead the GaAs source, in the mount shown in
Fig. 4.4, was positioned where the specimen is normally located during
absorption measurements. With an internal circuit change and external
switching source it was possible to synchronize the 211-A square-wave
generator to the internal 13 cps chopping rate of the spectrometer. The
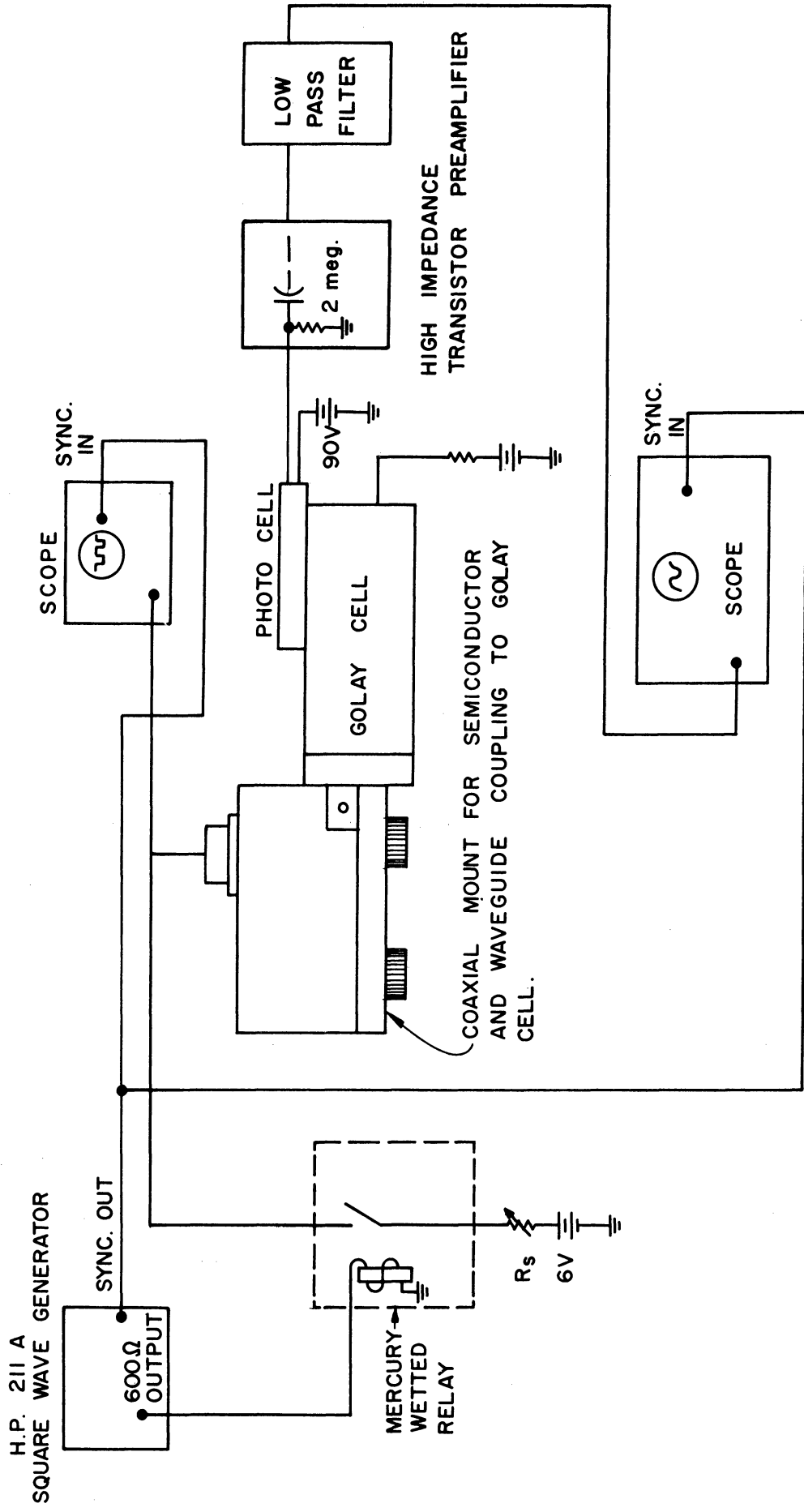output was then maximized by positioning the beam emitted by the GaAs

FIG. 4.5   INFRARED RADIATION DETECTION CIRCUIT FROM GaAs STRUCTURES.

structure through the 0.6 inch long, 50 Gc cutoff waveguide. The exit of the radiation mount was placed approximately five inches from the entrance to the monochrometer in a chamber flushed with dry nitrogen gas to reduce the water vapor absorption lines.

This instrument is designed to operate in the region from 25 μ to 200 μ and has diffraction gratings available with lines spaced by 125 μ, 50 μ, 33.3 μ and 25 μ. These gratings are blazed for maximum reflection at 112.5 μ, 45 μ, 30 μ and 22.5 μ respectively.

Figure 4.6 shows a chart recorder plot of emitted radiation as a function of current density as the grating angle is varied. From these tests it was not yet possible to establish the spectral distribution of the radiation. The GaAs crystal was pulsed with a 13 cps, 50 percent duty cycle current source. It can be seen from Fig. 4.6 that the radiated spectrum from the lowest current density (345 amp/cm^2) is very smooth; however, as the current density is increased, fine structure appears in the spectrum. For the highest current density (715 amps/cm^2) the spectrum becomes more peaked.

Since the above spectral data indicated that at least a portion of the radiation spectrum might occur in the region beyond 100 μ, a vacuum far infrared spectrometer was used to investigate this region. Such an instrument was designed by Randall[30] in the late 1930's. This instrument is still in use and has recently been improved with a better far infrared spectral purification system. Since transmission and reststrahlen materials with good band characteristics have not been found in the region beyond 100 μ, this instrument uses three gratings in zeroth order with alternating polarity to eliminate shorter wavelength radiation.

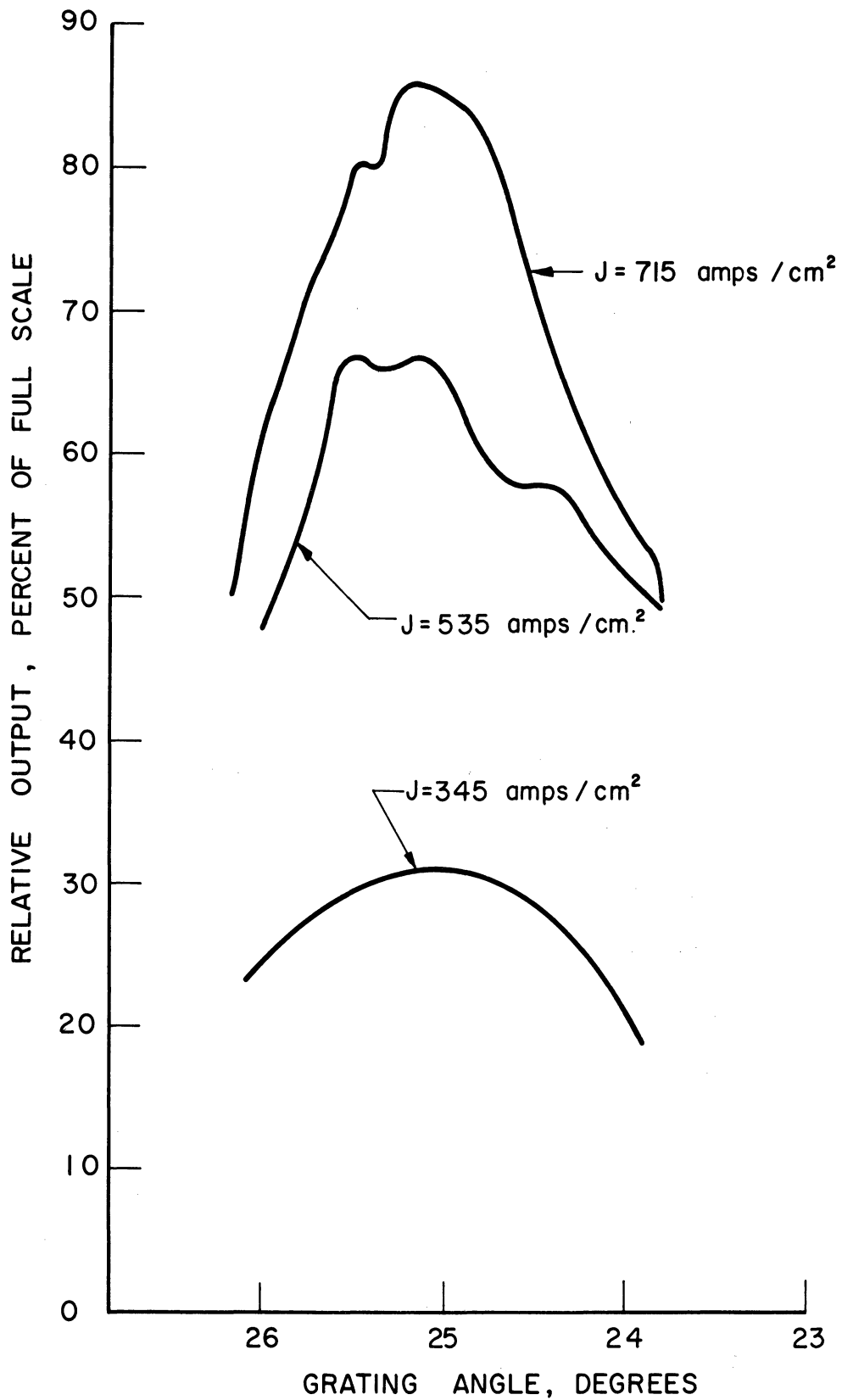30. Randall, H. M., "The Spectroscopy of the Far Infrared", Rev. of Mod. Phys., vol. 10, pp. 72-85; January, 1938.

FIG. 4.6   SPECTRAL OUTPUT VS. ANGLE OF 125 μ GRATING FOR VARIOUS CURRENT DENSITIES.

With this instrument set to eliminate radiation shorter than 100 μ, it was determined that with current densities up to 715 amps/cm^2 (the highest investigated in the previous Perkin Elmer Model 301 spectrometer data) no radiation could be detected beyond 100 μ. Subsequent tests established that the observed radiation is concentrated in the region between 4 μ and 40 μ. These included the following transmission filter tests:

a. The reference condition was established by transmitting directly into a Golay cell with a diamond window. Diamond has a flat transmission characteristic[31] for wavelengths longer than 1 μ, except for a sharp absorption band at 5 μ, thus its reference output will be considered 100 percent.

b. A glass slide (which transmits[31] wavelengths shorter than 2.6 μ) reduced the relative output of the diamond window Golay cell to the point where it could not be detected, indicating that the majority of the radiation is longer than 2.6 μ.

c. A quartz window (which has an absorption band between 4.5 μ and 44 μ) reduced the relative output of the diamond window Golay cell to about five percent of full scale.

d. A potassium iodide window (which has a flat 80 percent transmission characteristic[31] between 0.25 μ - 35 μ) reduced the relative output of the diamond window Golay cell to 72 percent of full scale.

Thus it is apparent that the majority of the radiation is between 4 μ and 40 μ.

Figure 4.7 shows the threshold and variation of the total radiated power from a GaAs source as measured with a diamond window Golay cell.

---

31. Smith, R. A., Jones, F. E., Chasmar, R. P., Detection and Measurement of Infrared Radiation, Oxford Press, London; 1957.
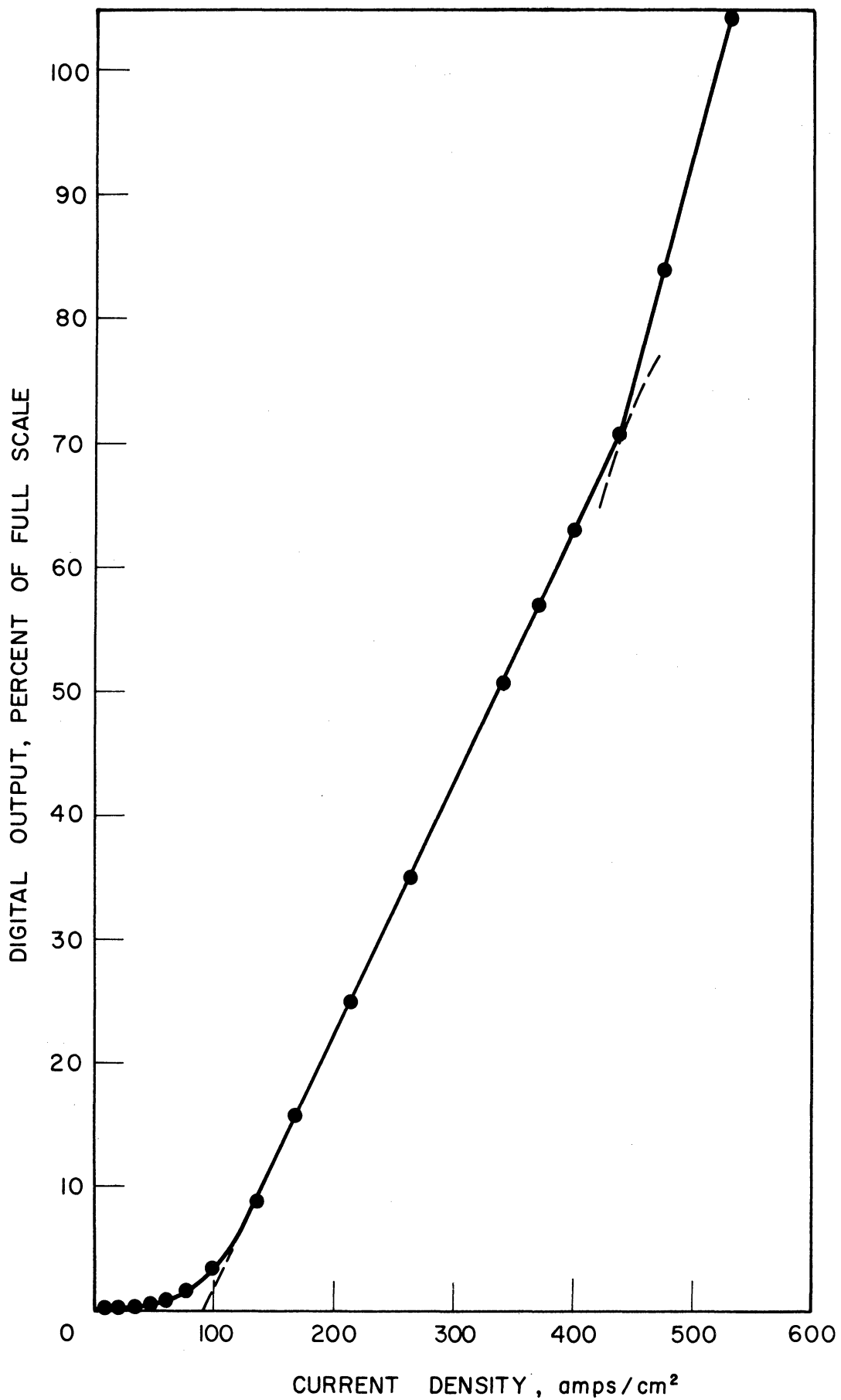
FIG. 4.7 SPECTRAL OUTPUT AT CENTER BAND AND THRESHOLD CONDITION VS. APPLIED CURRENT DENSITY.

The digital reading is recorded in relative units as measured with the electronics of the Perkin Elmer Model 301 spectrometer. It is to be noted that the output rises linearly and is asymptotic to 90 amps/cm^2. This is a distinctly different behavior than one would expect from a thermal radiation source since an ideal black body has a peak radiation intensity which goes as T^4 and the temperature of a bulk crystal goes as I^2; thus one would expect a total radiated power increase which is much more rapid than linear from a black body source excited by direct current.

In the above data, indicating a linear relationship exists between total infrared radiated power and current density, the current source was chopped at a 13 cps rate with a mercury wetted relay to produce chopped radiation with a 13 cps fundamental frequency corresponding to the response time of the Golay cell. A question arises concerning the return of crystal temperature to the ambient (300°K) during the off half cycle of the chopped source current. If the crystal did not return to the ambient during the half period (77 msec), at least a portion of the linear IR power vs. current relationship could be due to an increasing background temperature during the off half period temperature with increased current density. This would give a differential IR power vs. current density measurement.

To evaluate this possible discrepancy, measurements were made with a circuit which allows direct recorder plots of IR power vs. current density with the radiation being chopped at 10 cps rather than the current which produces the radiation being chopped.

Figure 4.8 shows the infrared detection and plotting circuit. The radiation mount is covered by a black background except for a 0.120 x 0.120 inch^2 exit radiation aperature from the waveguide coupled to the
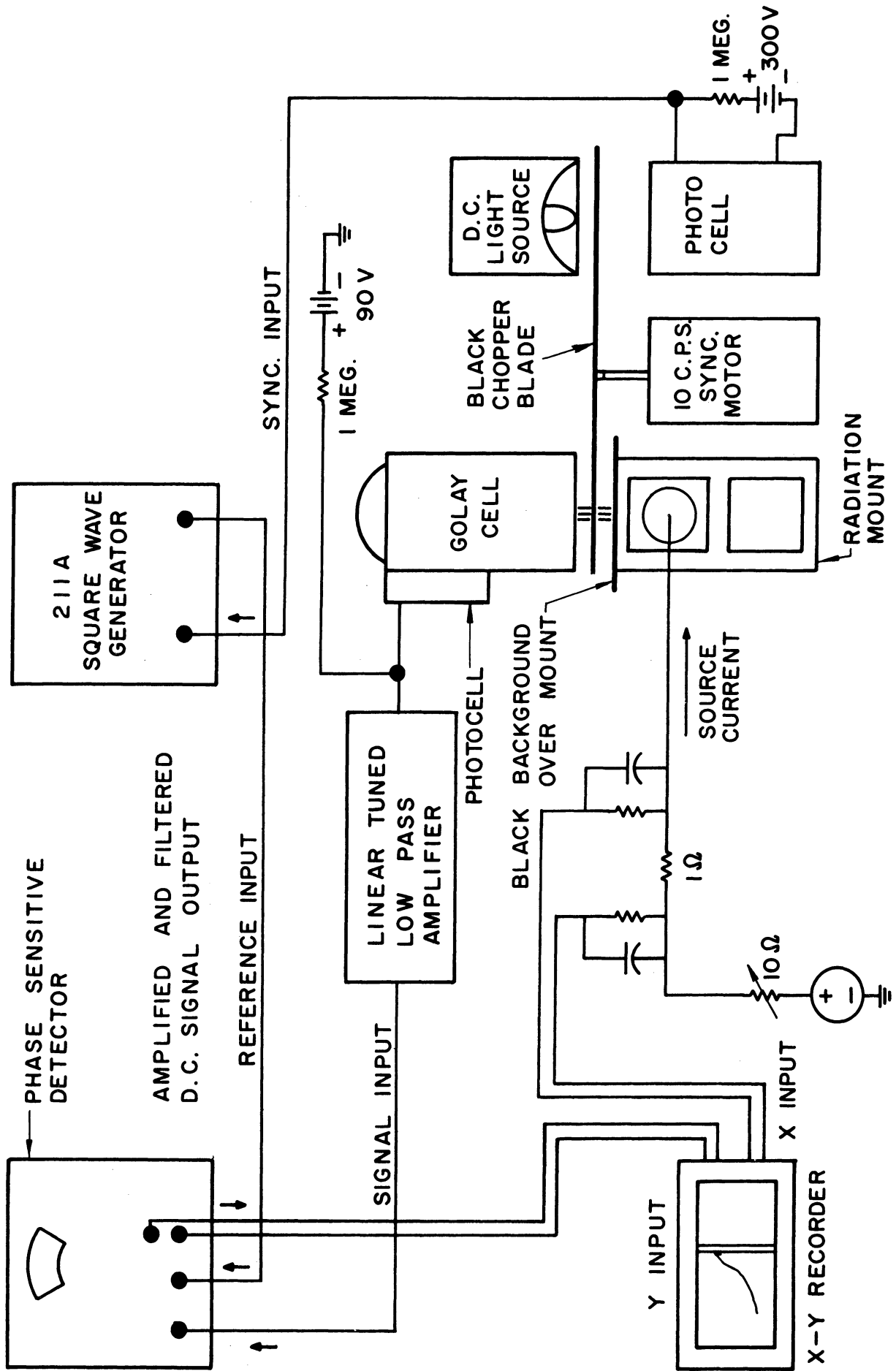
FIG. 4.8 INFRARED DETECTION AND PLOTTING CIRCUIT.

98

GaAs source. The radiation from the mount is chopped with a 10 cps synchronous motor. A d-c light source illuminating a photocell is chopped 180 degrees out of phase and the detected signal is used to synchronize an HP-211A square-wave generator which supplies the reference input to a phase sensitive detector. The IR radiation output from the detecting photocell of the Golay cell is preamplified by a transistorized, high impedance, low pass, linear amplifier. The phase sensitive detector is tuned to 20 cps with a 1 cps bandwidth. The amplified and filtered d-c signal output of the phase sensitive detector supplies the Y input to the X-Y recorder while the X input is derived from the voltage drop across a 1 ohm (50 watt) resistor at the input to the radiation mount.

Measurements have been made on two n-type GaAs crystals with dimensions of approximately 0.020 x 0.020 x 0.008 inch^3. Contacts of electroless nickel over a gold flash were deposited in this laboratory. Carrier concentration is (1-2) x 10^{17}/cm^3 and total device resistance is approximately 1.5 ohms. Figures 4.9 and 4.10 show radiation data taken on devices No. 2 and No. 3, respectively.

It is apparent that a nearly linear relationship of IR power vs. current density is automatically plotted in each case for a current density up to 700 amperes/cm^2. Thus it appears that the possibility that a differential temperature was measured in the initially reported data can be discounted.

4.4.3 Spectral Distribution of Infrared Radiation. The infrared spectral distribution of radiated power from two n-type GaAs crystals of (1-2) x 10^{17} carriers/cm^3 with electroless nickel contacts has recently been measured. A Perkin Elmer Model 21 Double Beam Infrared Spectrophotometer was used with a rock salt prism to cover the region
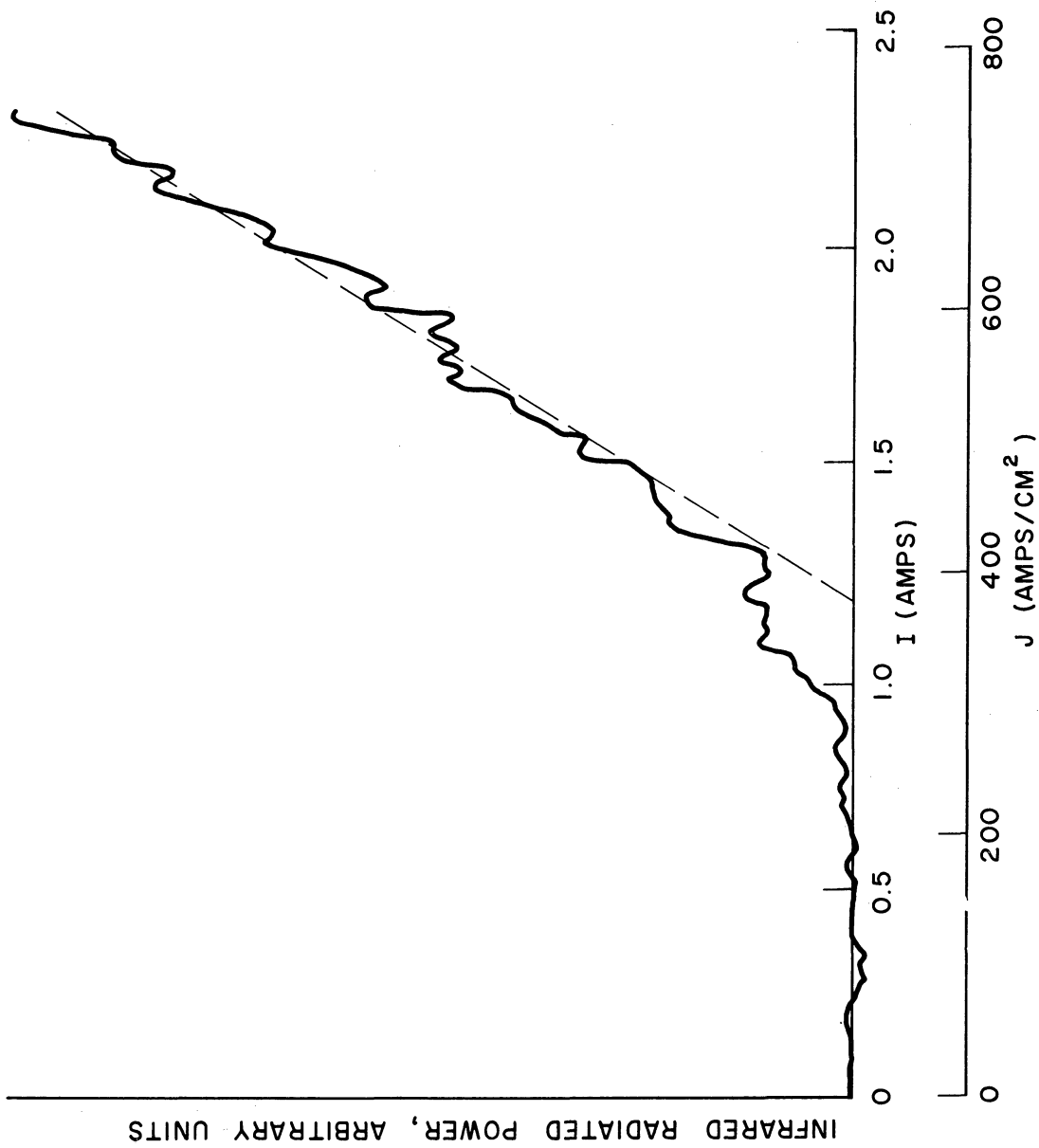
FIG. 4.9 IR RADIATION VS. CURRENT (CURRENT DENSITY) WITH GOLAY CELL DETECTOR. (DEVICE NO. 2)
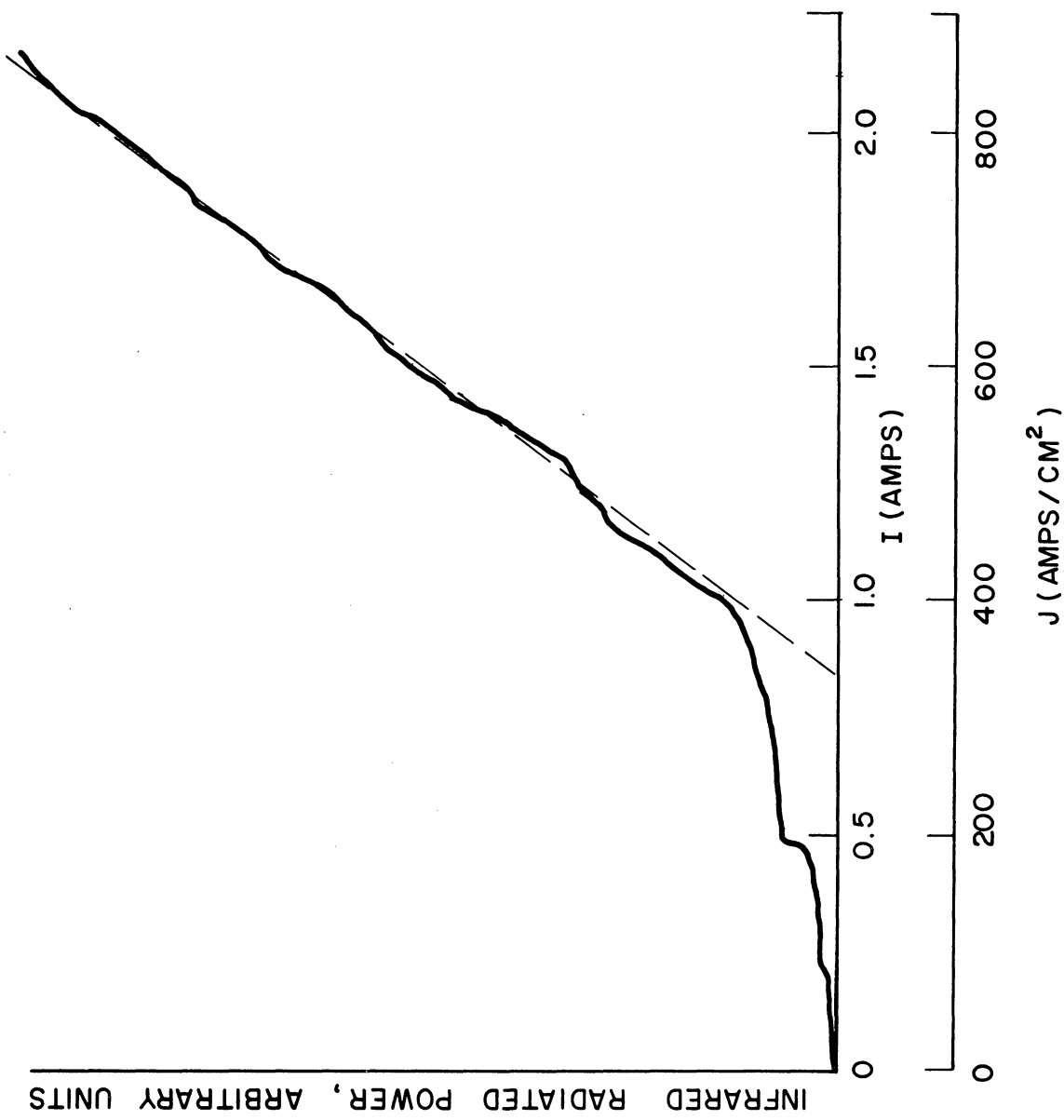
FIG. 4.10 IR RADIATION VS. CURRENT (CURRENT DENSITY) WITH GOLAY CELL DETECTOR. (DEVICE NO. 3)

between 2 - 16 μ. A thermocouple with a KBr window was used as the detector. The radiation is chopped at 13 cps by the spectrometer.

Figure 4.11 shows the spectral distribution with two different current densities for device No. 2 (previous data on this device is shown in Fig. 4.9). It is apparent that there is no radiated power with wavelength shorter than 4 μ as previously determined from transmission filter tests. At 800 amps/cm^2 a nearly constant radiation spectrum occurs between 4.6 μ and 8.0 μ. At 10 μ very interesting peaks and fine structure begin to appear in the radiation spectrum. With increased current density double peaks develop in the spectrum and shift toward longer wavelength with increased current density. In addition a very sharp absorption occurs near 15.8 μ. This latter effect may be due to the prism or optical phonon absorption since absorption measurements[26] have established that in GaAs the optical phonons are distributed in the 15 μ - 150 μ region.

Work is presently progressing to utilize a prism which will allow examination of the spectrum between 16 μ - 40 μ. In addition, a mount is being designed with a cesium iodide window which will allow operation at 77°K in order to examine the potentially significant changes in the radiation spectrum with reduced temperature.

At this point no statement will be made concerning the source of the observed infrared spectrum until the indicated measurements can be completed. However, it is felt that the detail of the radiation spectrum revealed in initial measurements indicates the potential importance of this investigation for fundamental studies of generation and interaction of radiation in bulk semiconductors and potential device application in the intermediate region between the previously exploited optical and
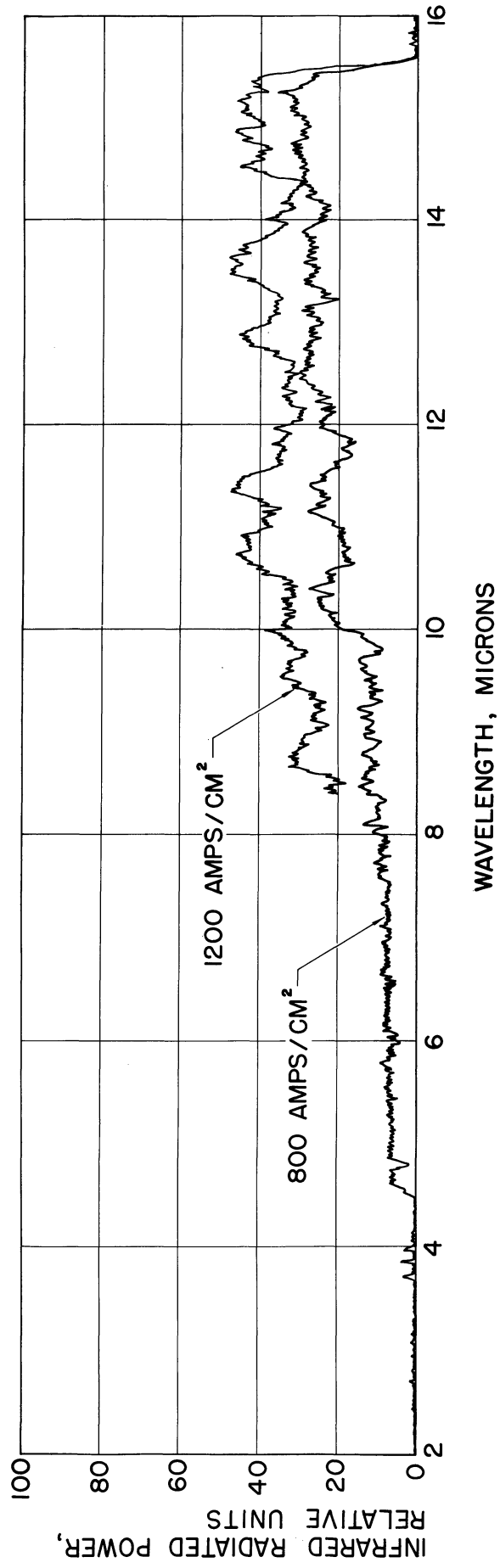
FIG. 4.11 RELATIVE INFRARED RADIATED POWER VS. WAVELENGTH FOR A 1 x 10^{17} n-TYPE

GaAs CRYSTAL AT ROOM TEMPERATURE.

microwave regions. Work in this area will be continued under Contract AF33(615)-1553.

5. The Traveling-Wave Phonon Amplifier   (C. Yeh, J. E. Rowe)

5.1 Introduction. The traveling-wave phonon interaction in bulk semiconductor materials may be described by the coupling of the electron wave functions and the phonon eigenstates for lattice vibrations. In its simplist form, a longitudinal acoustical vibration in a crystal expands or compresses the lattice at various points giving rise to a change in the effective electrostatic potential acting on the electron. Such interactions result in an interchange of energy between the lattice vibrations and the electrons (the drifting charge carriers) when a d-c drift field is applied in the direction of the traveling phonon wave. Acoustic gain is realized when the carrier drift velocity exceeds the acoustic wave velocity.

An extensive literature survey was prepared at the beginning of this investigation and was reported in Interim Scientific Report No. 1. In the present report theoretical investigations of two fundamental aspects of the interaction phenomena are described, i.e., the piezoelectric and the deformation potential effects. In the first case, a simple one-dimensional theory of amplification using the piezoelectric effect in CdS crystals is presented. Equations for the determination of gain, the acoustic velocity, and the ω-β diagram are derived and discussed. In the second case, the results of Spector's[1] study on the use of deformation potentials as the coupling mechanism for phonon interaction are modified

---

1. Spector, H. N., "Amplification of Acoustic Waves Through Interaction with Conduction Electrons", Physical Review, vol. 127, No. 4, pp. 1084-1090; August 15, 1962.

and presented. This is followed by a discussion on the possible extension of the theory to include microwave frequency operation.

Experimental work was carried out at low frequencies (in the 30-100 mc region) and acoustic gain was actually observed. However, it was found that the principal limitation to phonon-wave amplifier performance is the very high coupling loss associated with the usual $\lambda/2$ X-cut quartz transducers attached to the traveling-wave phonon interaction crystal. Furthermore, the use of $\lambda/2$ quartz resonant transducers automatically limit the high frequency operation of the device. Motivated by these findings, a project was initiated to study the coupling loss of various schemes, particularly of thin film CdS on different substrate materials. Some preliminary results are presented in this report.

An interesting theoretical study on the waves in a solid-state plasma has been initiated in connection with this project. Although the subject is not directly related to the phonon-wave amplifier, the possibility of some interesting devices is worthy of further investigation.

5.2 General Analysis of the Traveling-Wave Phonon Amplifier. The general problem of wave propagation in anisotropic piezoelectric material is a complex one and leads to a fifth degree secular equation[2,3]. The five coupled system waves are made up of two transverse electromagnetic waves and three acoustic waves. In a piezoelectric material, each transverse electromagnetic wave creates stresses in the material which are accompanied by an acoustic wave forced to vibrate at the speed of light.

2. Kyame, J. J., "Wave Propagation in Piezoelectric Crystals" Jour. of Acoustical Soc. of America, vol. 21, p. 159; 1949.

3. Koga, I., Azuga, M., Yoshinaka, Y., "Theory of Plane Elastic Waves in a Piezoelectric Crystalline Medium and Determination of Elastic and Piezoelectric Constants of Quartz", Physical Review, vol. 109, pp. 1467-73; 1958.

Its amplitude is small and thus its effect on the electromagnetic wave is negligible. Each acoustic wave creates an electric field with transverse and longitudinal components. The transverse component corresponds to an electromagnetic wave forced to travel at the velocity of sound. Its effect on the acoustic wave is again small. However, the longitudinal component is electrostatic in nature and therefore couples to charge carriers in the medium and markedly changes the acoustic wave propagation constants. Thus a simplified analysis in one dimension is usually accurate enough to give a clear picture of the principle of operation of the traveling-wave phonon amplifier.

5.2.1 Longitudinal Acoustic-Wave Amplifier--A One-Dimensional Analysis[4]. In developing the theory of the traveling-wave phonon amplifier, the interaction of the phonon wave and the drifting carrier in a piezoelectric material is studied. Let us assume that the acoustic wave propagates in the z-direction and the charge carriers drift in the same direction. With the assumption of a small-signal analysis, the r-f current density can be written as

$$J_1 = u_0 \rho_1 + \rho_0 u_1 - \mu \frac{kT}{q} \frac{\partial \rho_1}{\partial z} , \qquad (5.1)$$

where u_0, u_1 are the d-c component and first-order perturbation in drift velocity respectively, ρ_0 and ρ_1 are the average density and its first-order perturbation of the charge carriers respectively. ρ_1 is of course related to the electric flux D_1 by the one-dimensional Poisson's

---

4. A similar derivation was given by Hutson, A. R., White, D. L., "Elastic Wave Propagation in Piezoelectric Semiconductors", Jour. Appl. Phys., vol. 33, No. 1, pp. 40-47; January, 1962.

equation, $\partial D_1/\partial z = \rho_1$. μ is the mobility of the charge carrier. The continuity equation in one dimension is written as

$$\frac{\partial J_1}{\partial z} + \frac{\partial \rho_1}{\partial t} = 0 \qquad (5.2)$$

and the equations of state of the piezoelectric material are

$$T = cs - eE$$
$$D = es + \epsilon E \quad , \qquad (5.3)$$

where T = the stress in newtons/m^2,

s = the dimensionless strain,

c = the elastic constant in newtons/m^2,

ϵ = the dielectric permittivity in farads/m and

e = the piezoelectric constant in coulombs/m^2.

The simultaneous solution of Eqs. 5.1, 5.2 and 5.3 yields a new equation of state such that

$$T = c's \quad , \qquad (5.4)$$

where

$$c' = c\left\{1 + \frac{e^2}{c\epsilon}\left[\frac{1 - (u_o/v) - j(u_o/v)^2 (\omega/\omega_D)}{1 - (u_o/v) - j(u_o/v)^2 (\omega/\omega_D) - j(\omega_c/\omega)}\right]\right\} \qquad (5.5)$$

and $\omega_c \triangleq \mu\rho_o/\epsilon$, the conductivity frequency and $\omega_D \triangleq qu_o^2/\mu k T$, the diffusion frequency. The details of this derivation have been represented in Interim Scientific Reports Nos. 1 and 3, and are therefore omitted in this report.

<u>a</u>. <u>The Gain Equation</u>. The acoustic gain/loss in the medium can be computed from Eq. 5.5 by calculating the attenuation constant. It is found that

$$\alpha = \frac{\omega}{v} c^{1/2} \text{Im}(c')^{-1/2}$$

$$= \frac{\omega}{v_o} \frac{e^2}{2c\epsilon} \frac{\omega_c/\gamma\omega}{1 + (\omega_c/\gamma\omega)^2 [(1-\gamma)^2 (\omega^2/\omega_c\omega_D) + 1]^2} , \qquad (5.6)$$

where $\gamma = 1 - u_o/v$ and

$v_o = (c/\rho_m)^{1/2} = $ the unperturbed acoustic velocity.

The scale factor $e^2/c\epsilon$ is an electromechanical coupling constant which is proportional to the ratio of mechanical to electrical energy stored in the medium. It can be seen that if $u_o > v$, i.e., if the drift velocity of the carriers is maintained at a value slightly greater than the acoustic wave velocity in the medium, γ becomes negative and so is the attenuation constant α. In other words acoustic gain instead of attenuation results.

If one introduces a modified Debye length defined as

$$\Lambda^2 \triangleq [\omega^2/\omega_c\omega_D k^2] (1-\gamma)^2 \qquad (5.7)$$

into Eq. 5.6 and normalized α with respect to the mechanical factor, the following equation results:

$$[\alpha] \triangleq \frac{\alpha v_o}{\omega(e^2/2c\epsilon)} = \frac{\gamma\omega/\omega_c}{(\gamma\omega/\omega_c)^2 + (k^2\Lambda^2 + 1)} . \qquad (5.8)$$

Since $\gamma\omega/\omega_c$ and $k^2\Lambda^2 + 1$ always appear as individual entities, they can be treated as variables and/or parameters respectively. Figure 5.1 is
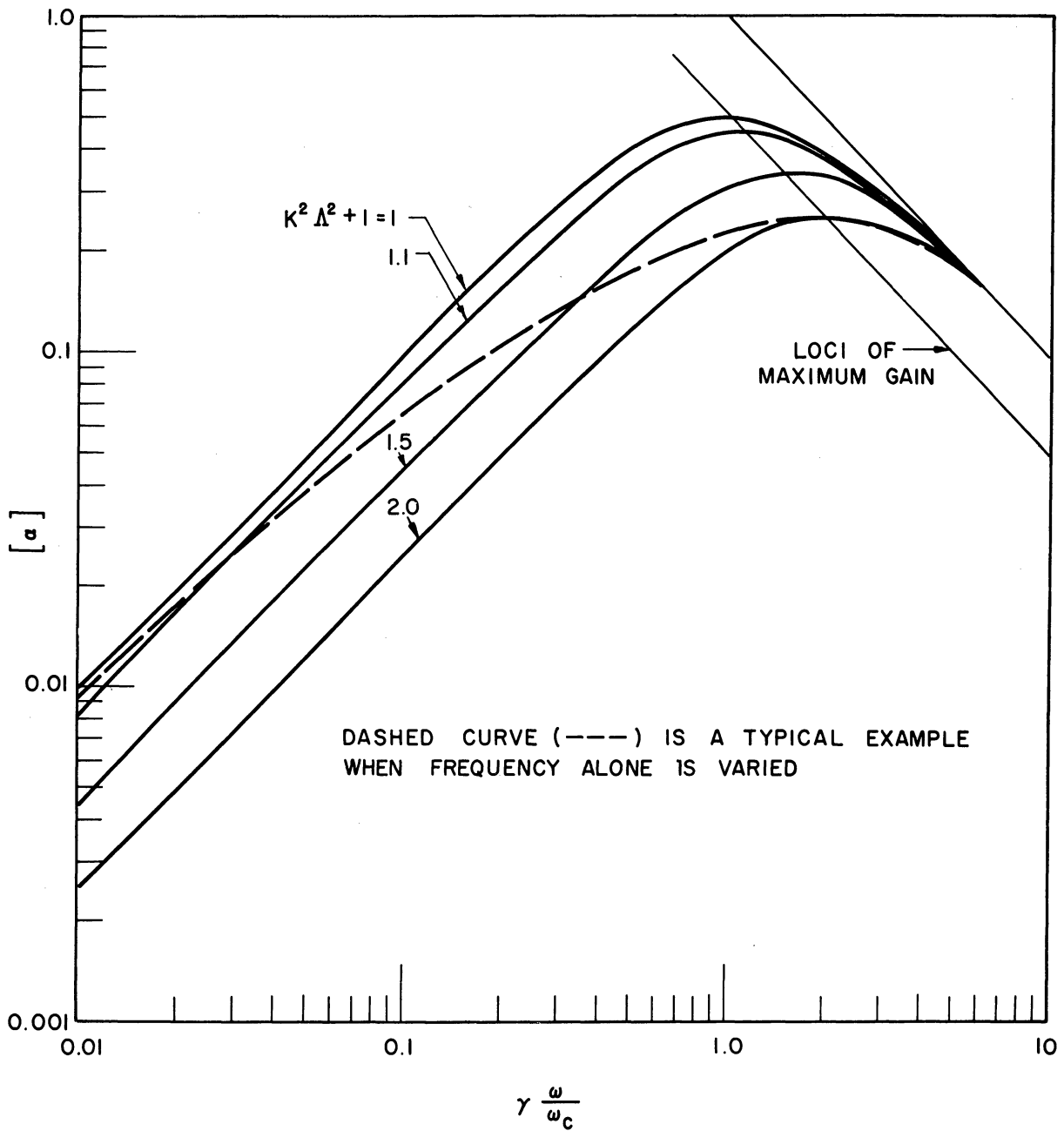
FIG. 5.1 NORMALIZED GAIN/ATTENUATION $[\alpha]$ VS. NORMALIZED FREQUENCY $\gamma\omega/\omega_c$ FOR VARIOUS VALUES OF $k^2\Lambda^2 + 1$.

a plot of Eq. 5.8 using $\gamma\omega/\omega_c$ as a variable and $(k^2\Lambda^2 + 1)$ as a parameter. Notice that $-[\alpha]$ is plotted as positive for convenience. In using this plot to discuss the variation of the gain/attenuation constant with frequency, (condiser $k^2\Lambda^2$ as a constant for the time being) it must be remembered that $[\alpha]$ varies as $1/\omega$. At low frequencies where $(\gamma\omega/\omega_c) \ll (k^2\Lambda^2 + 1)$, α is actually proportional to ω^2. This situation is represented as a straight line with unit positive slope on a log-log plot of $[\alpha]$ vs. $\gamma\omega/\omega_c$. On the other hand, a straight line with a negative unity slope actually signifies the frequency independance of α. Curves of the normalized $[\alpha]$ for various values of $(k^2\Lambda^2 + 1)$ show a general pattern of increasing with $\gamma\omega/\omega_c$ at lower values of $\gamma\omega/\omega_c$ and then gradually leveling off toward a maximum indicated by

$$[\alpha]_m = \frac{1}{2(k^2\Lambda^2 + 1)} . \qquad (5.9)$$

This occurs at $(\gamma\omega/\omega_c) = k^2\Lambda^2 + 1$. From there on, the curves fall off asymptotically toward a straight line given by Eq. 5.9. Notice that the loci of the maximum $[\alpha]$ also follows a line parallel to this straight line. This indicates that the maximum gain/attenuation constant is also frequency independent.

The above discussion is strictly true only when $k^2\Lambda^2 + 1$ is constant. According to Eq. 5.7, $k^2\Lambda_2^2 = (1 - \gamma)^2 \omega^2/\omega_c\omega_D$, indicating that for a constant drift velocity u_o, and a nearly constant acoustic velocity v, $k^2\Lambda^2$ is proportional to ω^2. Thus at lower frequencies, when $k^2\Lambda^2$ is small, the gain curve $[\alpha]$, calculated for say $k^2\Lambda^2 = 1$, is actually too conservative. In other words, the actual $[\alpha]$ curve would run from the curve marked $k^2\Lambda^2 + 1 = 1$, crossing all curves of $1 \leq (k^2\Lambda^2 + 1) \leq 2$ to reach the point of maximum gain on the $k^2\Lambda^2 + 1 = 2$ curve and then cutting

back into the curves for $k^2\Lambda^2 + 1 > 2$. A typical curve of this kind is shown as the dotted line in Fig. 5.1.

The significance of the parameter $k^2\Lambda^2 + 1$ needs further explanation. From Eq. 5.7, it is clear the $k^2\Lambda^2$ is intimately related to the conductivity and diffusion frequencies. Since $\gamma = 1 - u_o/v$ is usually a small negative number for practical amplifiers, then $1 - \gamma \simeq 1$ and $k^2\Lambda^2 \simeq \omega^2/\omega_c\omega_D$. Thus $k^2\Lambda^2 + 1 = 2$ (or $k^2\Lambda^2 = 1$) would actually specify $\omega^2 = \omega_c\omega_D$ or $(\omega_c/\omega) = \omega/\omega_D$. In other words, the conduction current equals the diffusion current. This is also the condition for maximum gain if ω alone is varied. $k^2\Lambda^2 + 1 = 1$ (or $k^2\Lambda^2 = 0$) is a limiting case at low frequencies. At these frequencies, $\omega_c/\omega \gg \omega/\omega_D$. In other words, the ratio of conduction to diffusion current is much greater than unity. Under these conditions, the maximum gain becomes

$$\alpha_m = \frac{\omega_c}{v_o} \frac{e^2}{2c\epsilon} \frac{1}{2\gamma} .$$ (5.10)

Now if $N = (\omega/2\pi v_o)L = L/\lambda$ is the length of the crystal in acoustic wavelengths, then the maximum gain in db is given by

$$G_{max} = 27.3 \, (e^2/2c\epsilon) \, N \quad \text{db} .$$ (5.11)

For $k^2\Lambda^2 + 1 > 2$, or $k^2\Lambda^2 > 1$, or $\omega/\omega_c > \omega_D/\omega$, one has a high frequency case and the gain is reduced.

Sometimes it is helpful to present the gain/attenuation curves in a slightly different form. Equation 5.8 can be modified to the following form:

$$[\alpha] = \frac{\alpha v_o}{\omega} \left(\frac{e^2}{2c\epsilon} \right) = \frac{(1 - u_o/v)(\omega_c/\omega)}{(1 - u_o/v)^2 + [(\omega/\omega_d) + (\omega_c/\omega)]^2} .$$ (5.12)

Here $\omega_d = (v^2/u_o^2)\, \omega_D$ has been defined to remove the effect of μ and E on ω_D. In Eq. 5.12, u_o/v appears as a discrete parameter and can be treated as a single variable. Since $u_o = \mu\, E_o$, and if v remains unchanged, the variation in u_o/v can be considered either as the variation of the drift field E_o for a constant μ or as the variation of mobility μ for constant E_o. Constant v is considered as a reasonable approximation. In fact, for actual amplifier application, ω_c/ω and ω/ω_d are chosen so as to make v approximately constant.

The variation of $[\alpha]$ in response to the change of u_o/v can be seen from two plots in Figs. 5.2 and 5.3. Notice that the shape of these curves are quite similar. The curves start to show amplification (posi-tive $[\alpha]$) as soon as u_o/v becomes slightly greater than unity. They reach the respective maximum at $(u_o/v) = 1 + (\omega_c/\omega) + (\omega/\omega_d)$ and decreases monotonically thereafter for increasing u_o/v.

The maximum value of $[\alpha]$ is

$$[\alpha]_m = \frac{(\omega_c/\omega)}{2[(\omega/\omega_d) + (\omega_c/\omega)]} . \qquad (5.13)$$

In general, it is desirable to have the maximum gain occur at a value of u_o/v as close to unity as possible. This would mean either a low drift field E or a lower mobility μ or both. This is possible if both ω/ω_d and ω_c/ω are less than unity and as small as possible.

One interesting case exists if $\omega/\omega_d = \omega_c/\omega$. Under this condition $[\alpha] = 1/4$ and remains unchanged. This occurs at $\omega = \sqrt{\omega_c \omega_d}$, and is also the frequency at which maximum gain can be obtained if ω alone is varied. The horizontal dotted line in Fig. 5.2 with points indicating the various values of $\omega/\omega_d = \omega_c/\omega$ depicts this special case.
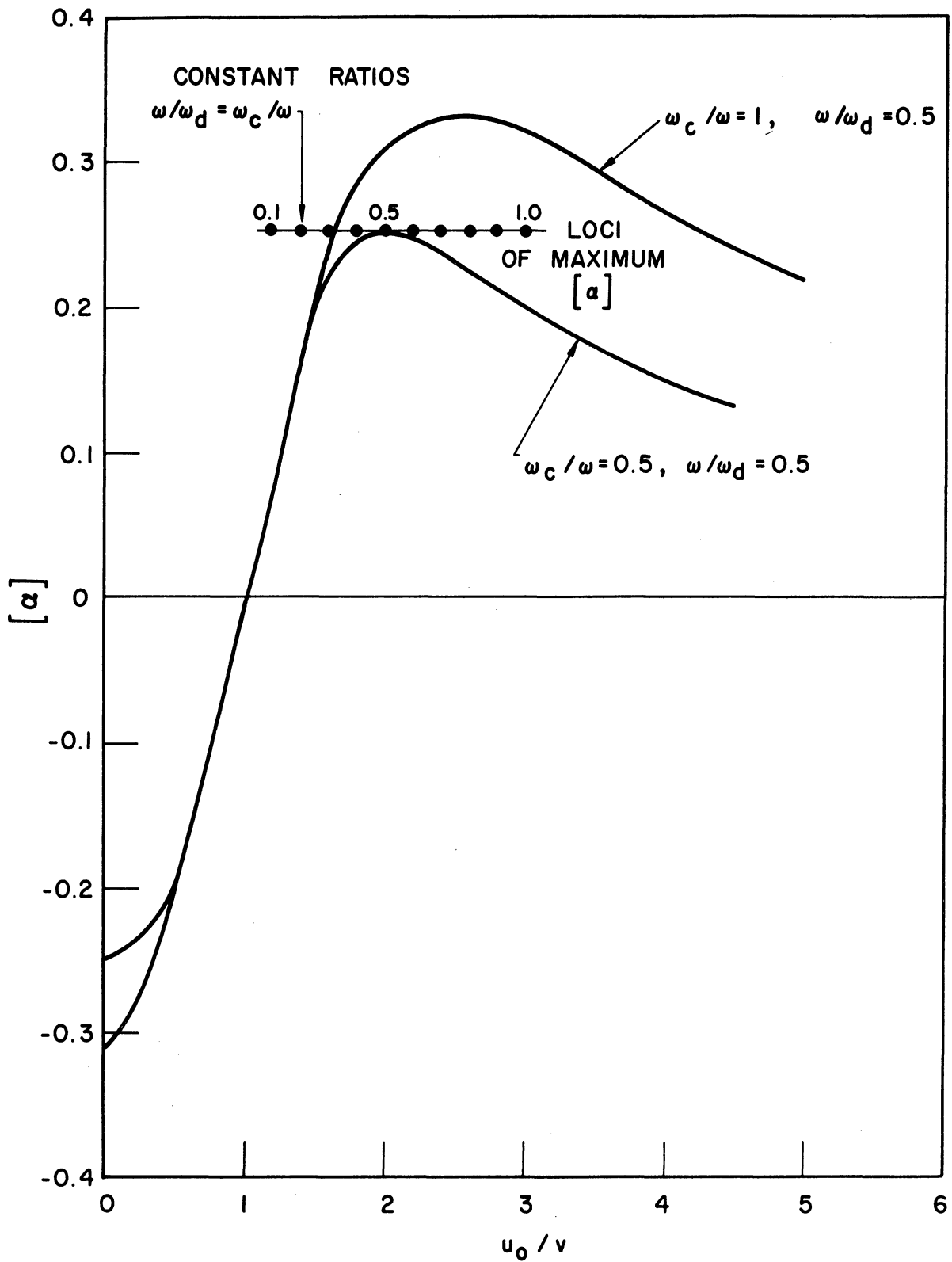
FIG. 5.2 NORMALIZED GAIN/ATTENUATION $[\alpha]$ VS. u_o/v FOR $\omega_c/\omega = 1$, $\omega/\omega_d = 0.5$;

$\omega_c/\omega = 0.5$, $\omega/\omega_d = 0.5$.
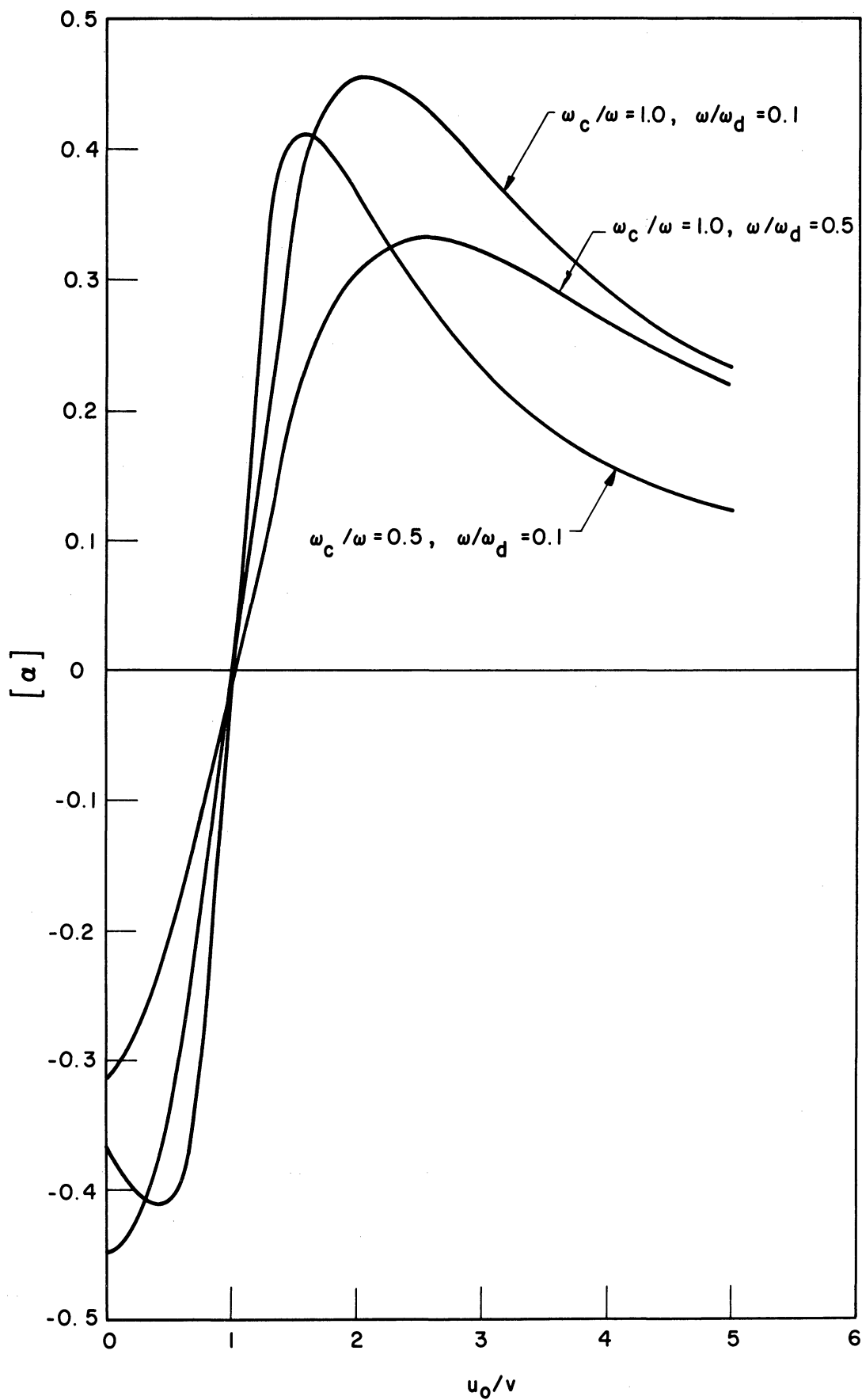
FIG. 5.3 NORMALIZED GAIN/ATTENUATION $[\alpha]$ VS. u_o/v FOR $\omega_c/\omega = 1.0$, $\omega/\omega_d = 0.1$; $\omega_c/\omega = 1.0$, $\omega/\omega_d = 0.5$; $\omega_c/\omega = 0.5$, $\omega/\omega_d = 0.1$.

114

The maximum gain as a function of ω/ω_d for various values ω_c/ω is plotted in Fig. 5.4. It is obvious that the maximum gain decreases as ω_c/ω is decreased and decreases as ω/ω_d is increased. For high frequency operation for a given crystal, the combination of lower ω_c/ω and increasing ω/ω_d is therefore responsible for the rapid decrease in gain.

Figure 5.4 might lead one to believe that a larger ω_c or a higher material conductivity might be helpful in order to maintain a higher ω_c/ω ratio at high frequencies and thus obtain a higher gain. Unfortunately this criterion cannot be used without bound. For materials with high conductivity, it is difficult to maintain a d-c field of the proper magnitude for adequate operation, i.e., to maintain a drift velocity higher than the acoustic velocity in the medium. Even if such a field could be maintained, the drift current due to this field would be so excessive as to overheat the crystal and thus change its property. In practice therefore, a limit is set such that both ω_c/ω and ω/ω_d are less than unity. In other words, both the conduction and diffusion currents are small in comparison with the displacement current.

The mobility μ of the material is important in determining the critical d-c field required for proper operation, i.e., $u_o \geq v_s$. As $u_o = \mu E$, high mobility is advantageous since it reduces the critical field required to match the acoustic velocity. This leads also to the criterion that the carrier density should not be too high.

b. The Acoustic Velocity. Equation 5.5 can also be used to derive the equation for the acoustic velocity. It can be shown that the acoustic velocity of propagation is given by

$$v = \text{Real} \frac{(c')^{1/2}}{\rho_m^{1/2}} = v_o \text{ Real} \frac{(c')^{1/2}}{c^{1/2}} . \tag{5.14}$$
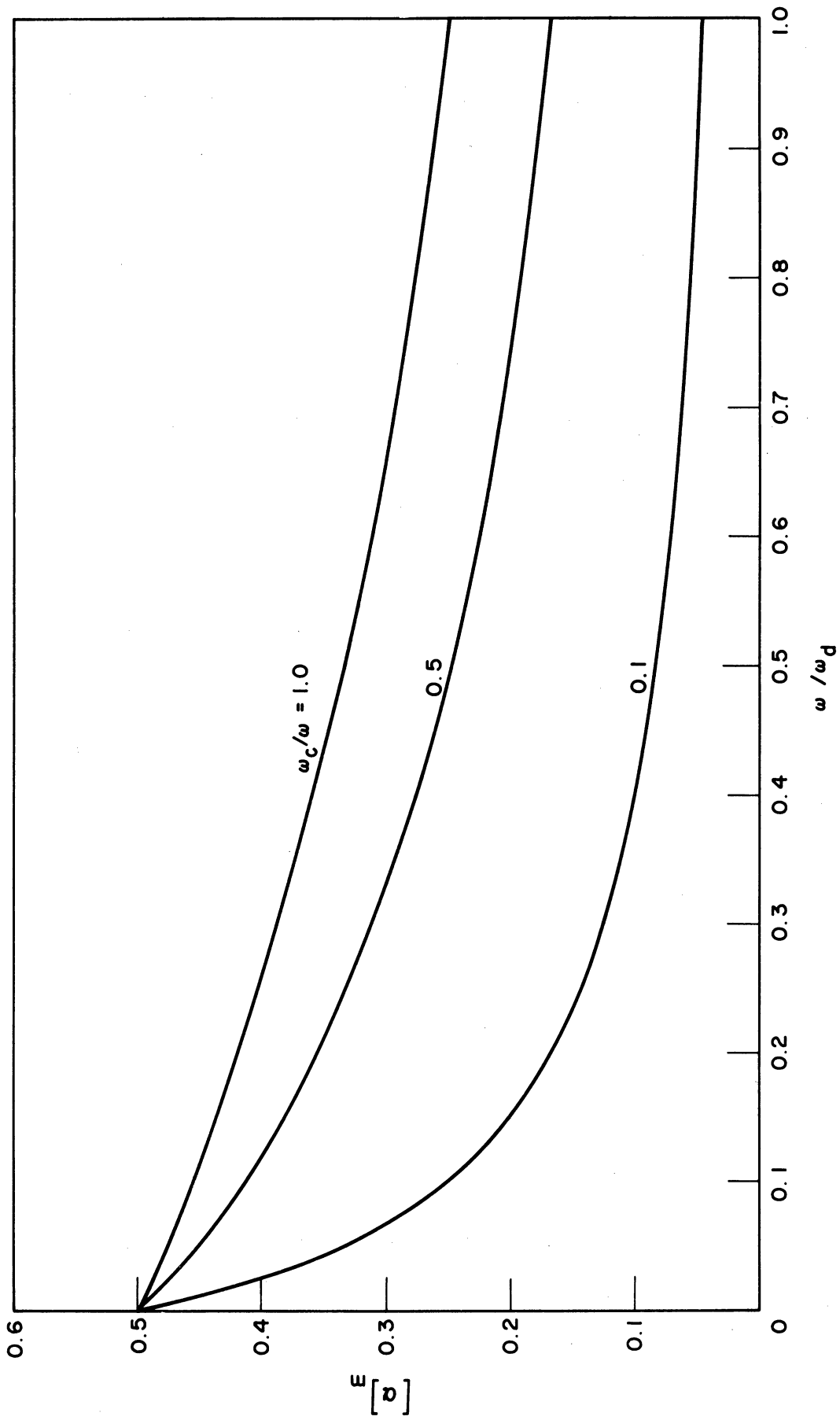
FIG. 5.4 MAXIMUM GAIN/ATTENUATION $[\alpha]_m$ VS. ω/ω_d FOR VARIOUS VALUES OF ω_c/ω.

If Eq. 5.7 is used for c' in Eq. 5.14 and carrying out the indicated manipulation yields

$$[v] \triangleq \frac{(v - v_o)/v_o}{e^2/2c\epsilon} = \frac{(\gamma\omega/\omega_c)^2 + k^2\Lambda^2 (k^2\Lambda^2 + 1)}{(\gamma\omega/\omega_c)^2 + (k^2\Lambda^2 + 1)^2} \, . \qquad (5.15)$$

A plot of $[v]$ vs. $\gamma\omega/\omega_c$ with $k^2\Lambda^2 + 1$ as parameter results in a universal graph as shown in Fig. 5.5. Curves for constant $k^2\Lambda^2 + 1$ remain horizontal for smaller values of $\gamma\omega/\omega_c$ at their respective zero frequency limiting values and increase asymptotically to unity, the upper limit at infinite frequency. If Fig. 5.5 is used to discuss the variation of $[v]$ with frequency, it must be remembered that $k^2\Lambda^2 + 1$ also varies with frequency. The dotted curve indicates one typical variation of $[v]$ with frequency.

One useful form for the discussion of the acoustic velocity in the medium is to find the ω-k diagram. This can be accomplished by solving Eq. 5.15 in terms of ω and k, noticing that $v = \omega/k$. Equation 5.15 can be rewritten as

$$\frac{v - v_o}{v_o \, e^2/2c\epsilon} = \frac{(1 - u_o/v)^2 + (\omega/\omega_d) [(\omega_c/\omega) + (\omega/\omega_d)]}{(1 - u_o/v)^2 + [(\omega_c/\omega) + (\omega/\omega_d)]^2} \, . \qquad (5.16)$$

Notice that the original diffusion frequency ω_D has been redefined as $\omega_d = \omega_D(v/u_o)^2$ so as to rid its dependence on the drift velocity u_o. Solve Eq. 5.16 for ω and k, with the result that

$$\omega^5 - v_o k (1 + A) \omega^4 + (1 + 2 \, \omega_c/\omega_d) \, \omega_d^2\omega^3 - \omega_d^2 k \{2u_o + v_o [1 + A$$

$$+ (2 + A) \, \omega_c/\omega_d]\} \, \omega^2 + \omega_d^2 [\omega_c^2 + 2u_o k^2 v_o (1 + A) + u_o^2 k^2] \, \omega$$

$$- \omega_d^2 v_o k [\omega_c^2 + u_o^2 (1 + A) k^2] = 0 \qquad (5.17)$$

DASHED CURVE (———) IS A TYPICAL EXAMPLE
WHEN FREQUENCY ALONE IS VARIED.
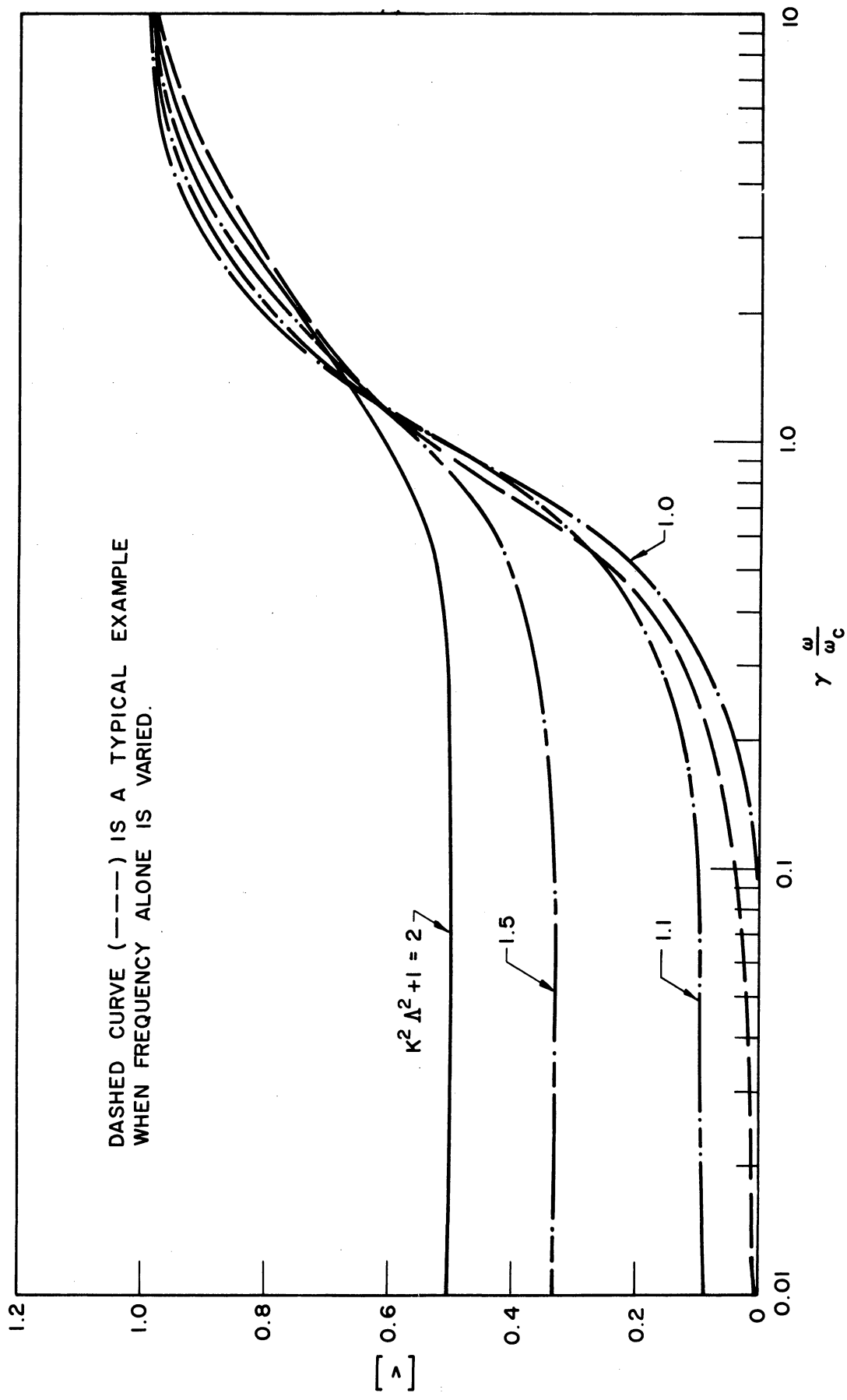
FIG. 5.5 NORMALIZED ACOUSTIC VELOCITY [v] VS. FREQUENCY $\gamma\omega/\omega_c$ FOR VARIOUS VALUES OF $k^2\Lambda^2 + 1$.

or

$$u_o^2 v_o \ (1 + A) \ k^3 - 2u_o \ [v_o \ (1 + A) + u_o/2] \ \omega k^2$$

$$+ \ \{2u_o + v_o \ (1 + A) + v_o \ [(\omega_c/\omega) + (\omega/\omega_d)] \ [(\omega_c/\omega) \ \omega \ (1 + A)/\omega_d]\} \ \omega^2 k$$

$$- \ \{1 + [(\omega_c/\omega) + (\omega/\omega_d)]^2\} \ \omega^3 \ = \ 0 \ , \quad (5.18)$$

where $A = e^2/2c\epsilon$. Equations 5.17 and 5.18 can be solved numerically. To

solve Eq. 5.17, k is assumed to be a real value, positive or negative.

For a typical set of parameters, the roots of ω are found. Negative

real roots of ω are rejected because they are physically unrealizable.

Complex roots are retained as they help to identify the time instability

of the amplifier. The results of the computation for a typical set of

parameters are summarized and plotted in Fig. 5.6. There are five roots

for ω. ω_1, which is the only positive real root of the system, varies

linearly with k. This is perhaps the working mode of the amplifiers in

which the phase and group velocities are the same. This makes the match-

ing of the drift velocity of the carriers to the acoustic wave velocity a

simple matter. There are two pairs of complex conjugate roots of ω,

labeled as ω_2, ..., ω_4, each with a prefix Re or Im to indicate respec-

tively the real or imaginary part of the complex frequency. The real

parts of these frequencies are very close to the positive real frequency

ω_1 as is indicated by the dotted line beside ω_1. The imaginary parts of

one pair of conjugate roots remain practically unchanged at 10^{10} cps

while the other pair, which is much smaller in magnitude, remains virtu-

ally unchanged at lower values of k but increases for the values of k

greater than 1000. The existence of these complex roots may indicate the

possibility of time instabilities. However, whether oscillation will take

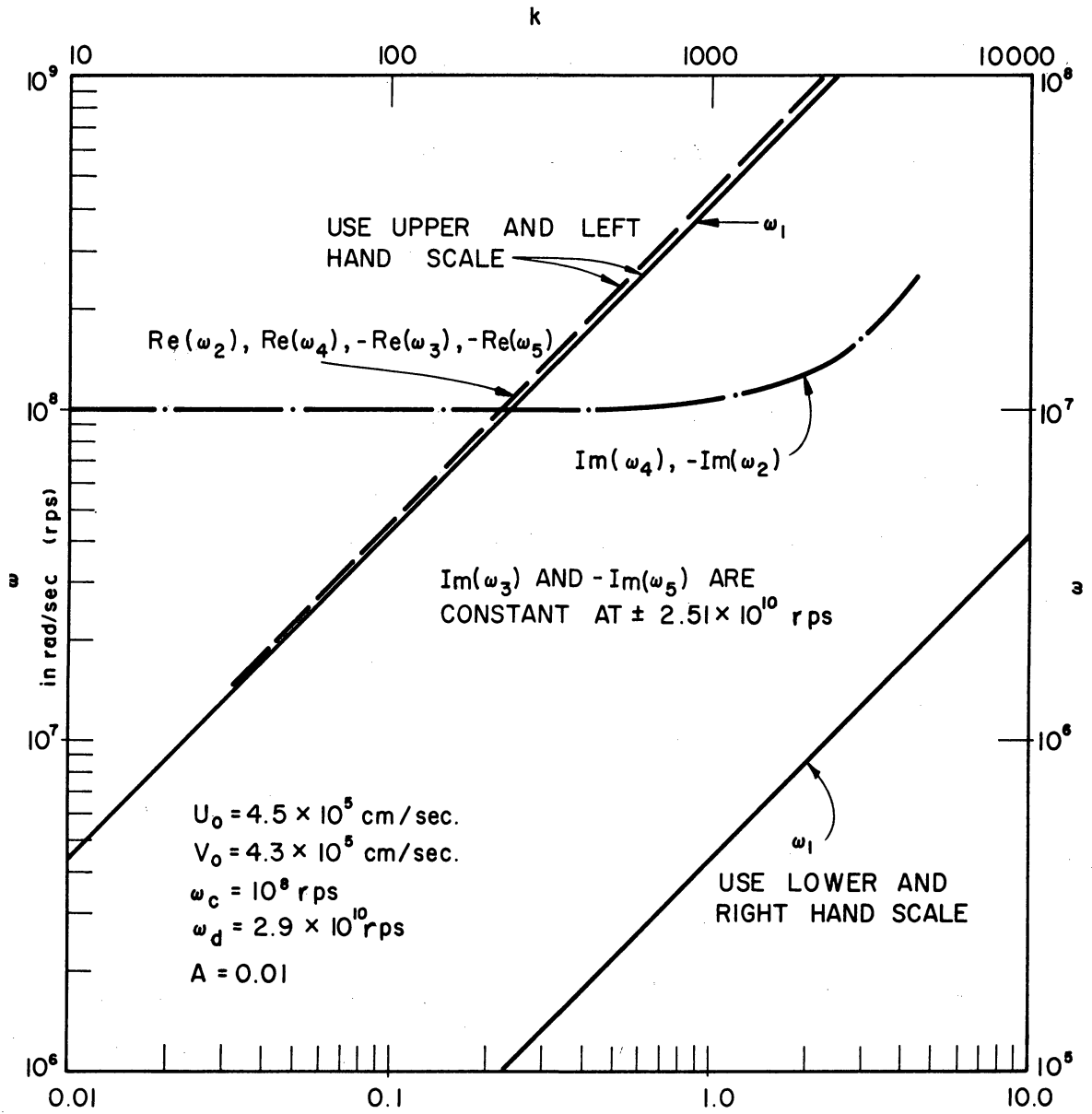place depends upon the boundary conditions appropriate to the crystal.

FIG. 5.6 ω-k PLOT FOR THE SOLUTION OF EQ. 5.17 ASSUMING k IS POSITIVE AND REAL.

Complex roots also exist for negative values of k and thus it may be possible to have a backward-wave mode of oscillation (see discussion in the next section).

To solve Eq. 5.18, assume ω is positive and real and solve for the roots of k. In this way a negative real root of k indicates a backward mode of propagation and a complex k indicates a spatial instability. For a typical set of parameters, Eq. 5.18 is solved numerically and the roots are plotted in Fig. 5.7. There are three roots of k, one positive real and a pair of complex conjugate roots. There is no negative real root of k, indicating that backward-wave modes are not likely. The imaginary part of the complex k is virtually constant for all values of ω up to 10^9 cps. The real part of the complex root follows close to but is slightly smaller than the real root of k. However, if ω_c is changed by a factor of 10 (smaller), the imaginary part of the complex k is reduced by almost tenfold and increases with increasing frequency.

5.2.2 The Shear Mode Interaction. Crystals of appropriate orientation can also be excited into shear mode vibrations. Interaction between carriers and the shear mode of vibration in piezoelectric crystals has the advantage of requiring a lower electric field for amplification. This is because the velocity of propagation of the shear mode of vibration is lower than that of the longitudinal vibration and thus requires a lower drift field for the carriers to match the wave velocity. It is, therefore, interesting to investigate the characteristics of the traveling-wave phonon interaction for the shear mode.

Let us still limit our discussion to a one-dimensional model. In a shear mode of operation, the conduction carriers produced by the drift field are moving in a direction perpendicular to the direction of propagation
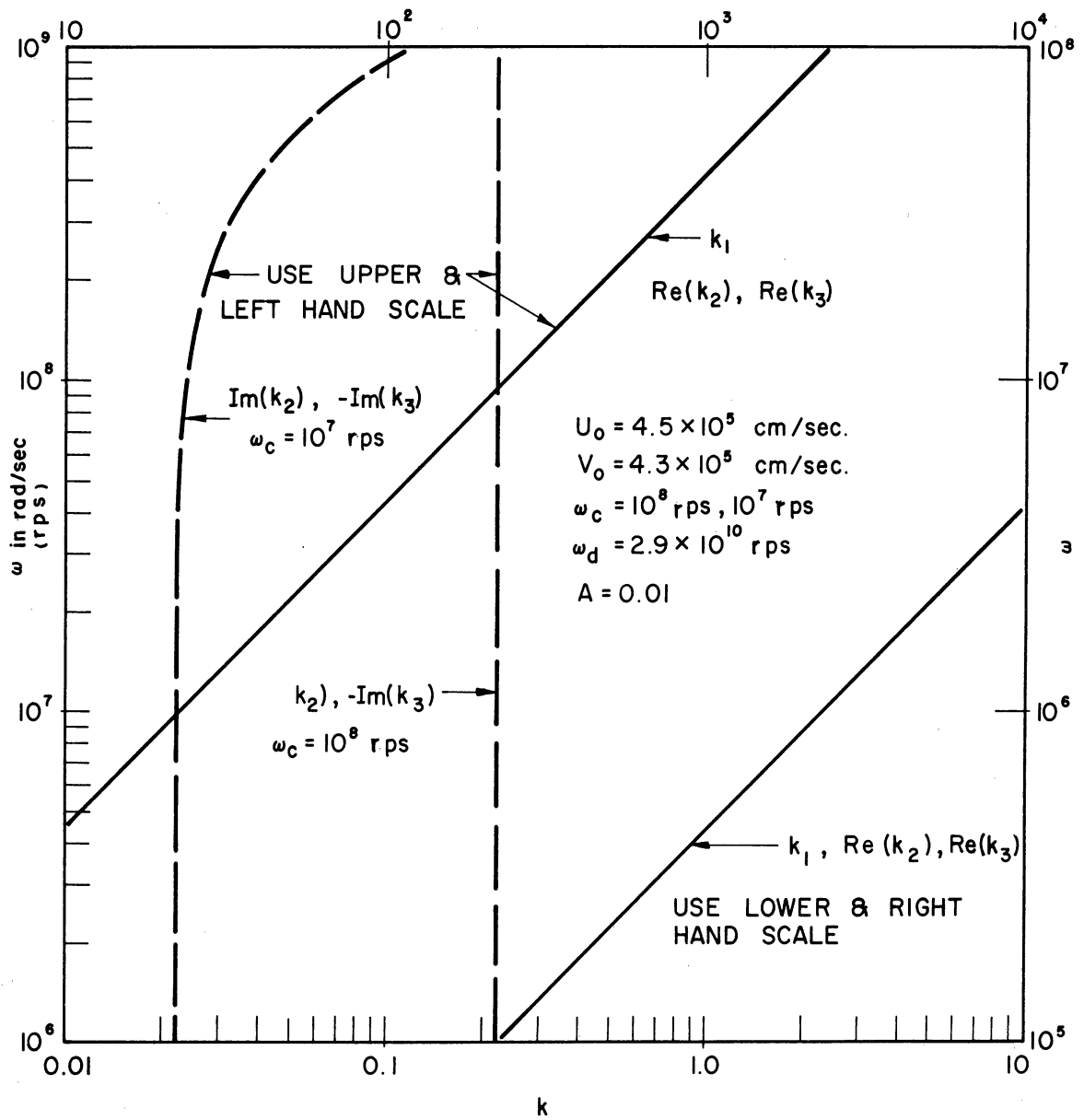
FIG. 5.7 ω-k PLOT FOR THE SOLUTION OF EQ. 5.18 ASSUMING ω IS POSITIVE AND REAL.

122

of the acoustic wave. Amplification of an acoustic wave can only take place if there is a mechanism which couples the shear waves to the drifting carriers. Such a mechanism is provided for by the longitudinal field of piezoelectric origin accompanying a transverse wave. In such a case, one still only needs to solve a one-dimensional problem provided that the proper piezoelectric coefficient and electric constants are chosen. Return now to the equations of state. These equations, in the most general form, (the piezoelectric constants e_{ijk}, the elastic constants c_{jk} and the dielectric constant ϵ_{jk}) are all tensors. However, by utilizing the hexagonal symmetry of the piezoelectric crystal, one can still use the simplified version of these equations for either longitudinal or shear wave modes provided that the appropriate coefficients are used. The effect of changing the mode of operation will manifest itself in two ways: the unperturbed acoustic velocity will be changed as $v_o = (c/\rho_m)^{1/2}$, where c is actually c_{11} for the longitudinal wave and c_{44} for the transverse wave; also the piezoelectric constants will be different, e_{333} in the longitudinal mode and e_{113} in the transverse mode. Further discussion in this connection will be brought out in the next section.

_5.2.3_ _Deformation_ _Potential_ _Interaction_. As phonon waves propagate within the crystal, the momentary change in compression (in a longitudinal wave) produces local variations in the size and shape of the unit cell. The change in lattice constant will thus change the energy-band structure in the crystal. The change in energy-band boundaries may be seen to be substantially equivalent to the introduction of a varying potential for an electron which is referred to here as the deformation potential. This effect is in general quite small in most crystals. Particularly for piezoelectric materials, the effect of the deformation

potential may be negligible in comparison to the corresponding piezoelectric effect. However, certain semiconductors which may be chosen for the phonon-wave amplifiers due to their high carrier mobility may not have the desired piezoelectric effect, while the effect due to the deformation potential may be significant. A typical material of this kind is the very pure n-type InSb. It has a mobility of 5×10^5 cm^2/volt-sec and a deformation potential constant C of about 10 ev.

In a recent publication by Spector[5], the problem of phonon wave amplification through interaction with conduction electrons was treated using the deformation potential as the coupling mechanism for both longitudinal and transverse waves. In order to use his results, Spector's equations are rewritten in terms of our present notations. Details of conversion are omitted.

a. Longitudinal wave (Eq. 3.56 in Spector's paper). For $\lambda > \ell$, (ω/ω_c) $(k\ C_{zz}/q\ E) > 1$,

$$\alpha = \frac{N_0 qE}{9\ c_{zz}} \frac{\gamma \left(\dfrac{\omega}{\omega_c}\right)^2 \dfrac{k^2 C_{zz}^2}{q^2 E^2}}{\left(\gamma \dfrac{\omega}{\omega_c}\right)^2 + \left[1 + \dfrac{\omega^2}{\omega_c \omega_D} (1 - \gamma)^2\right]^2} , \qquad (5.19)$$

where C_{zz} is the deformation potential constant in the z-direction and C_z is the elastic constant in the same direction. E is the drift field in the same direction, ℓ is the mean free path of the electrons. For $\lambda < \ell$,

$$\alpha = \frac{\pi N_0 qE}{2\ c_{zz}} \frac{\gamma(1 - \gamma)^2 \dfrac{\omega}{\omega_D} \left[1 + \dfrac{\omega}{\omega_c} \dfrac{kC_{zz}}{qE}\right]^2}{\left[1 + \dfrac{\omega^2}{\omega_c \omega_D} (1 - \gamma)^2\right]^2} . \qquad (5.20)$$

5. Loc. cit.

b. Transverse wave. For $\lambda > \ell$, $(\omega/\omega_c)(kC_{xz}/qE) > 1$,

$$\alpha = \frac{N_o qE}{c_{xz}} \frac{k^2 C_{xz}^2}{q^2 E^2} \frac{\gamma \left(\dfrac{\omega}{\omega_c}\right)^2}{\left(\gamma \dfrac{\omega}{\omega_c}\right)^2 + \left[1 + \dfrac{\omega^2}{\omega_c \omega_D}(1-\gamma)^2\right]^2} . \qquad (5.21)$$

For $\lambda > \ell$,

$$\alpha = \frac{\pi N_o qE}{2c_{xz}} \frac{k^2 C_{xz}^2}{q^2 E^2} \frac{\gamma (1-\gamma)^2 \dfrac{\omega}{\omega_D}\left(\dfrac{\omega}{\omega_c}\right)^2}{\left[1 + \dfrac{\omega^2}{\omega_c \omega_D}(1-\gamma)^2\right]^2} . \qquad (5.22)$$

A few general remarks can be made before we proceed to simplify these equations for further discussion. It is observed that the effect of the deformation potential on the gain resembles that of the piezoelectric effect in that the gain is proportional to either the square of the piezoelectric coefficient "e" or to the square of the deformation potential coefficient "C". Furthermore, the gain equations for the longitudinal mode differ from those for the transverse mode only by the proper choice of the elements of the deformation potential tensor and the elastic constant tensor respectively.

In order to facilitate discussion of the above-mentioned equations, a new parameter τ_R is introduced where τ_R is defined as

$$\frac{1}{\tau_R} = \omega_c + \frac{\omega^2}{\omega_D}(1-\gamma)^2 \qquad (5.23)$$

and τ_R is the relaxation time of the carriers. This total relaxation time is composed of two contributions: that primarily due to the conduction (the first term) and that due to the diffusion (the second term) of the carriers. Rewrite Eq. 5.21 in terms of τ_R and notice that $c_{xz} = v_o^2 \rho_m$,

125

$(qE/v_o k^2 \tau_R) = k_e T_e$, where k_e is the Boltzmann's constant and T_e is the carrier temperature; then

$$\frac{\alpha}{\alpha_o \omega_c} = \frac{\gamma \, \omega \, \tau_R}{1 + (\gamma \, \omega \, \tau_R)^2} \, \frac{\omega}{\omega_c} \, , \qquad (5.24)$$

where

$$\alpha_o = \frac{N_o \, C_{xz}^2}{9 \, \rho_m \, v_o^3 \, k_e T_e} \, . \qquad (5.25)$$

The variations of $\alpha/\alpha_o \omega_c$ as a function of ω/ω_c is shown in Fig. 5.8. (It must be remembered that τ_R is also a function of ω/ω_c.) The gain increases from a low value at low frequencies and approaches a steady value at higher frequencies. However, at high frequencies the wavelength of the acoustic wave is no longer large compared with the mean free path of the electrons, so that Eq. 5.21 loses its validity. Instead, Eq. 5.22 or its equivalent form after introducing τ_R should be used. Thus,

$$\frac{\alpha}{\beta_o \omega_c} = \gamma \, \frac{\omega}{\omega_c} \, (1 - \tau_R \omega_c) \, (\tau_R \omega_c)^2 \, , \qquad (5.26)$$

where

$$\beta_o = \frac{\pi}{18} \, \frac{N_o \, C_{xz}^2}{\rho_m \, v_o^3 \, k_e T_e} \, . \qquad (5.27)$$

By using the frequency dependence of τ_R in Eq. 5.26, it can be shown that $\alpha/\beta_o \omega_c$ is inversely proportional to ω^3 and thus decreases rapidly for high frequencies.

In deriving the above equation an identity has been brought out which is rather interesting. It is found that

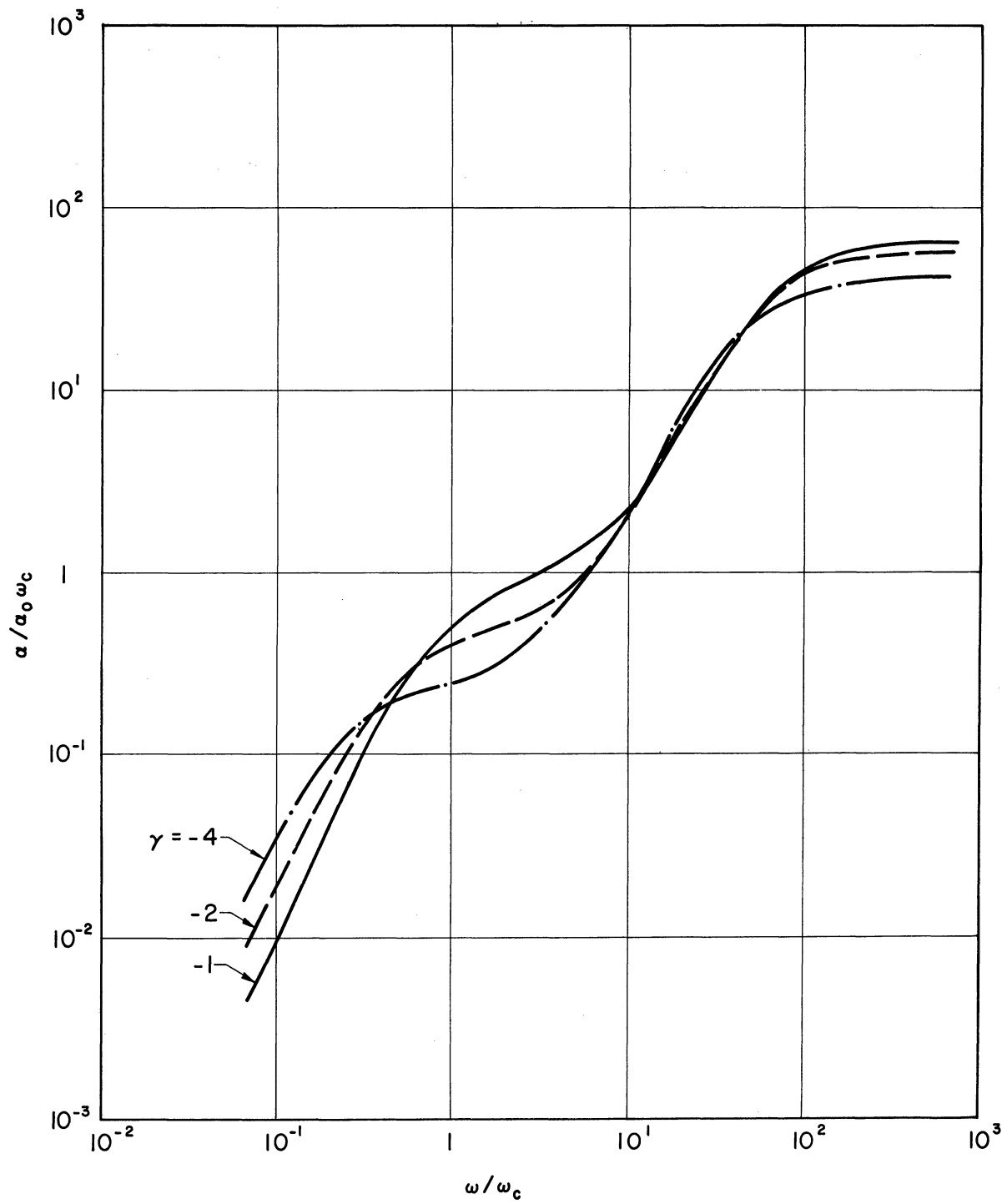$$\omega_c \omega_D = N_o \, q^2 \, v_o^2/\epsilon \, k_e T_e \, . \qquad (5.28)$$

126

FIG. 5.8 $\alpha/\alpha_0\omega_c$ VS. ω/ω_c FOR γ = -1, -2, -3 AND -4.

Since τ_R can be made larger by choosing a higher $\omega_c \omega_D$ product, it is therefore desirable to operate the phonon material at a low temperature. Other considerations, such as reducing collisions and thus reducing the material loss in the crystal, also favor low-temperature operation.

The effect of varying the drift field can be discussed in terms of the variation of γ, since $\gamma = 1 - \mu E/v_o$. Thus $\gamma = 0$ implies that the drift field E is just sufficient to cause the drift velocity μE of the carriers to equal the unperturbed acoustic velocity v_o. Positive values of γ mean small drift fields and negative values of γ signify large drift velocity. The discussion can best be presented by considering a fixed frequency, say $\omega = n\omega_c$, where n is any positive fraction or whole number and is treated as a parameter in this discussion. From Eq. 5.23, it is seen that τ_R is a function of γ. However, ω_D as defined previously as $\omega_D = u_o^2/D_n$ is not a constant if the drift field is varied. Using $\omega_d = \omega_D/(1 - \gamma)^2$, one can eliminate the field dependence of τ_R; then ω_c, ω_d and τ_R can be treated as constants and Eq. 5.24 can be rewritten as

$$[\alpha] = \frac{\gamma \, \omega_c \tau_R}{1 + (\gamma n \, \omega_c \tau_R)^2} \, , \qquad (5.29)$$

where $[\alpha] = \alpha/n^2 \alpha_o \omega_c$.

Variation of $[\alpha]$ as a function of γ is shown in Fig. 5.9 and it is noted that this function is symmetric with respect to γ and therefore only the absolute values of $[\alpha]$ are plotted against γ. These curves behave in a similar way as in the case of the piezoelectric acoustic-wave amplifier.

5.2.4 Microwave Aspect of Traveling-Wave Phonon Interactions.
The question of extending the theory of traveling-wave phonon interaction to microwave frequencies has been a subject of intensive discussion in
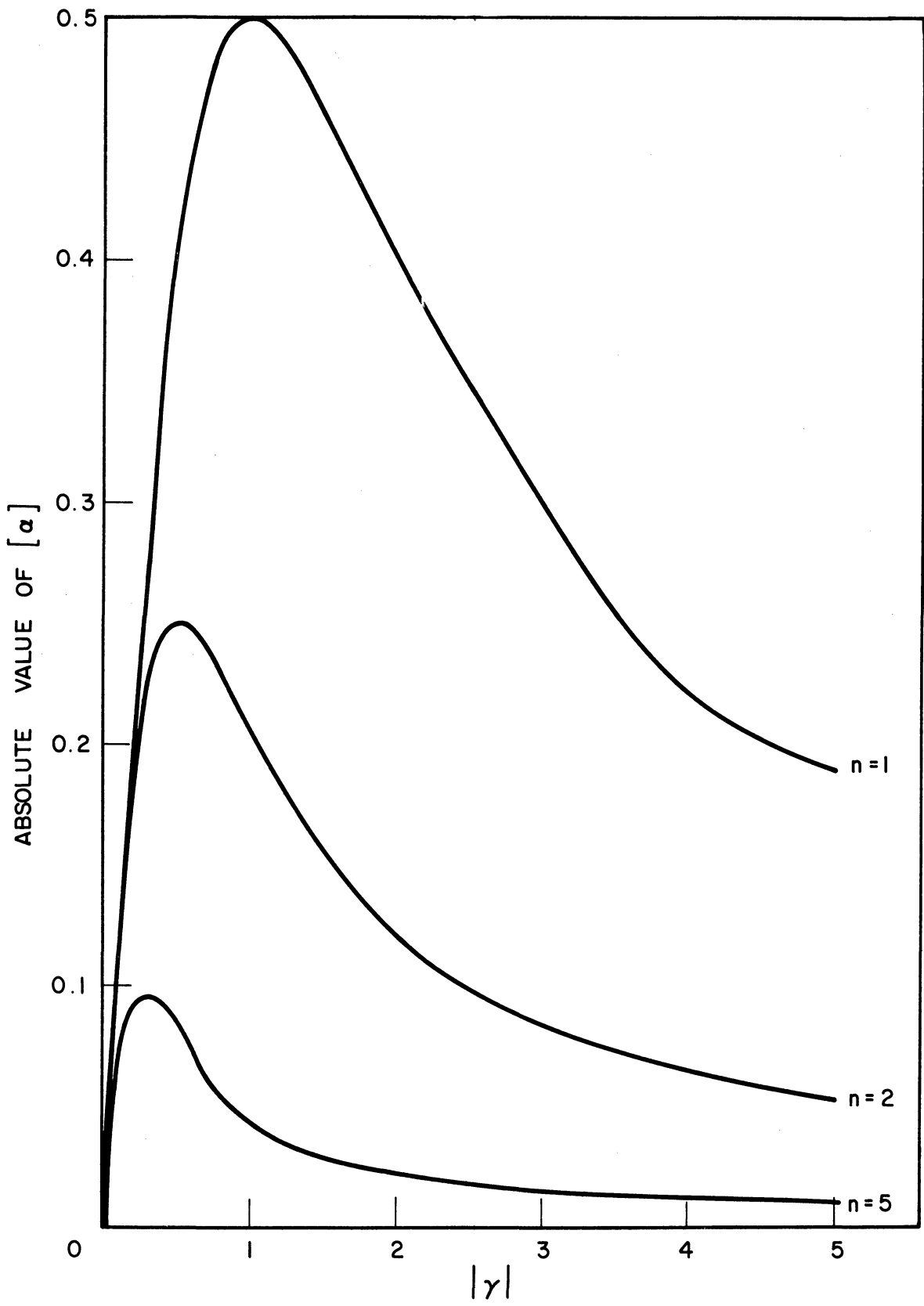
128

FIG. 5.9 $[\alpha]$ VS. $[\gamma]$ FOR n = 1, 2 AND 5.

recent years. In fact, many authors have revealed their optimistic views about this extension. To reduce the material loss, microwave operation is possible only at cryogenic temperature. Spector, by introducing the deformation potential in computing the gain of a traveling-wave phonon interaction, has suggested the use of other materials than CdS whose mobility is too low to be used at microwave frequencies. Materials such as GaAs and InSb have carrier mobilities many thousand times larger than that of CdS and are therefore better materials to use at microwave frequencies. Panwells[6] has computed the gain/cm of InSb using Spector's formula and found a gain of 5 db/cm under an electric field of 8 volts/cm at 10 Gc. Higher gain is obtained by using GaAs. In fact, in GaAs, the piezoelectric effect is several times larger than the deformation potential and can therefore be used promisingly at microwave frequencies. On the other hand, Conwell[7], in a paper published recently, argued that the estimate of gain at microwave frequencies using the low-field parameters of the crystal may lead to very optimistic results since power dissipation in the crystal heats the carriers. The increase in electron temperature affects the carrier mobility which in turn changes the diffusion frequency ω_D. The effect is to reduce the gain. Conservative estimates put a reduction factor of 10 or more on the gain.

5.3 Waves in Solid-State Plasma. The concept of using solids to study the plasma behavior is quite new and interesting. It offers many advantages over the gaseous plasma in experimental studies. Solids

6. Panwells, H. J., "Possibilities of Amplification of Sound Waves at Microwave Frequencies", Proc. IEEE, vol. 52, No. 3, p. 300; March, 1964.

7. Conwell, E. M., "Amplification of Acoustic Waves at Microwave Frequencies", Proc. IEEE, vol. 52, No. 8, pp. 964-965; August, 1964.

provide an ideal subject for comparing theory with experiment because some of the parameters characterizing the plasma, such as temperature, charge densities, etc., are well defined in contrast to the nonuniform and time-varying values in a transient gaseous discharge.

Two types of magnetoplasma waves in solids at low temperatures currently under intensive study are the "whistlers" and "Alfvén" waves[8]. Whistlers, or the helicon wave, have been observed in the electron gas of a metal at liquid helium temperature and are characterized by a frequency which is inversely proportional to the square of the wavelength so that the velocity increases as frequency increases. Alfvén waves result from the interaction between magnetic and kinetic energies in a plasma and are characterized by a frequency which is inversely proportional to the wavelength so that the velocity is constant.

An analysis of the hydromagnetic wave is given here with the suggestion that they be further investigated in appropriate semiconductor and semimetals.

Figure 5.10 illustrates a simple solid-state plasma configuration in which the possible current, velocity, magnetic field and electric field directions are indicated. Assume that the collision effects in plasma are neglected and that the effects of pressure and the gravitational potential are negligible. Assume also that the magnetoplasma has a time average velocity along the static B field, then the Boltzmann transport equation and the momentum equation simply reduce to the microscopic Lorentz equation, which in an assumed one-dimensional system becomes

$$\left(\frac{\partial v_x}{\partial t} + u_o \frac{\partial v_x}{\partial z} \right) = \frac{J_y B_o}{\rho_m} \, , \qquad (5.30)$$

8. Haus, H., "Alternating Current Generation Wire Moving Conducting Fluids", Jour. Appl. Phys., vol. 33, No. 7, pp. 2161-2172; July, 1962.
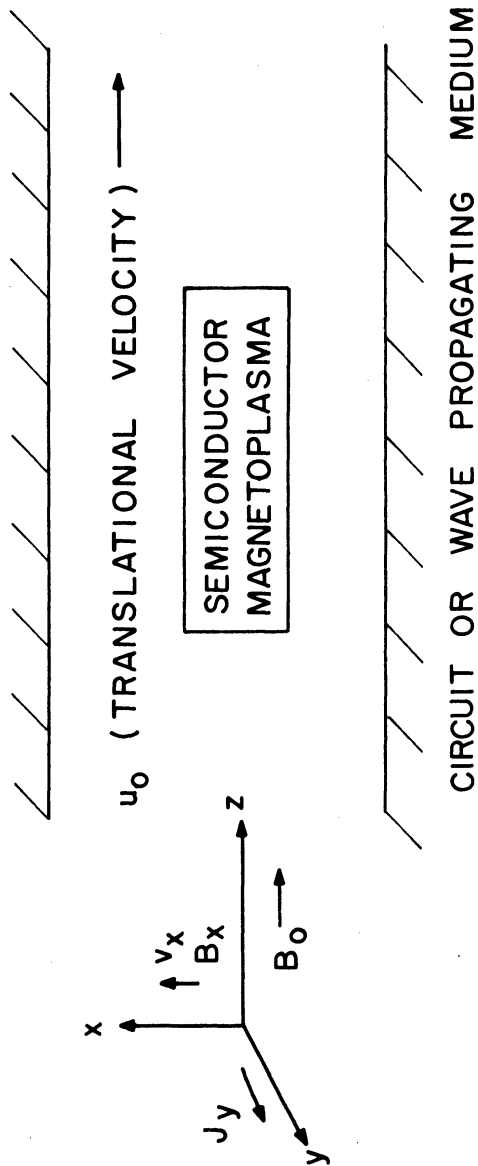
FIG. 5.10 SOLID-STATE PLASMA CONFIGURATION.

where $\rho_m = n_e m_e + n_h m_h$ is the mass density, v_x and J_y are the component velocity and current in the simplified system, B_o is the static magnetic field and u_o is the velocity along the B_o field. The Maxwell field equations are also simplified as

$$\frac{\partial E_y}{\partial z} = \frac{\partial B_x}{\partial t} \qquad (5.31)$$

and

$$\frac{\partial B_x}{\partial z} = \mu_o J_y \quad , \qquad (5.32)$$

where for a perfectly conducting magnetoplasma

$$E_y = - \left(u_o B_x - v_x B_o \right) \quad . \qquad (5.33)$$

The above equations are combined to give the following after some manipulation:

$$\left(\frac{\partial}{\partial t} + u_o \frac{\partial}{\partial z} \right)^2 v_x = V_A^2 \frac{\partial^2 v_x}{\partial z^2} \quad , \qquad (5.34)$$

where $V_A^2 \triangleq B_o^2 / \mu_o \rho_m$, the Alfvén velocity. For an ansatz of the form $e^{j(\omega t - kz)}$, Eq. 5.34 reduces to

$$(\omega - u_o k)^2 = k^2 V_A^2 \quad . \qquad (5.35)$$

The quadratic nature of Eq. 5.35 suggests two waves with phase constants

$$\beta_{1,2} = \frac{\omega}{u_o \pm V_A} \quad . \qquad (5.36)$$

For $V_A < u_o$, both waves are forward and the group velocity is

$$v_g = u_o \pm V_A \quad . \qquad (5.37)$$

133

The propagation of a wave along the circuit (z-direction) surrounding the semiconductor may be described in terms of the usual transmission line circuit and field equations and can be simplified to yield

$$(\beta^2 - \beta_o^2) \, E \;=\; -\, \omega \, \beta \, B_x \quad , \tag{5.38}$$

where $\beta_o^2 \;=\; \omega^2 \, LC$,

     $L, C \;=\;$ inductance and capacitance per unit length along the circuit and

     $E \;=\;$ the circuit field $\;=\; (\beta/\omega C) I$.

The combined magnetoplasma and circuit equations yield the system determinantal equation

$$(\omega - u_o \beta)^2 \;=\; \left[1 + \frac{\mu_o \beta_o^2 / L}{(\beta_o^2 - \beta^2)} \right] V_A^2 \beta^2 \quad . \tag{5.39}$$

It can be shown that complex β arises when $u_o > V_A$, i.e., when the carrier drift velocity exceeds the medium Alfvén velocity and thus energy may be transferred to the circuit wave.

    5.4 <u>Acoustic-Wave Transducer</u>. One of the principal limitations to acoustic-wave amplifier performance is the very high coupling loss associated with the usual $\lambda/2$ x-cut quartz transducers which are in general glued to the photoconductive material. In addition to high coupling loss such transducers are generally limited to the frequency region below about 1 Gc.

    5.4.1 <u>Thin Film Transducers</u>. Thin film diffused copper layer and thin insulating CdS films have been used for transducers with success. The latter scheme is even more promising for high microwave frequency operation. Films of CdS having a thickness for fundamental

resonance $\lambda/2$ for various frequencies are indicated in Table 5.1 assuming that the compressional velocity along the C-axis of CdS is 4.4×10^5 cm/sec.

Table 5.1

CdS Film Thickness vs. Frequency

$$(v = 4.4 \times 10^5 \text{ cm/sec})$$

f(ge)	Thickness t = $\lambda/2$
1	2.2 microns
3	0.72 microns
10	0.22 microns
30	720 Å
50	440 Å
100	220 Å
1000	22 Å

An evaporation setup has been constructed as shown in Fig. 5.11 by Dr. V. A. Vis of this laboratory to deposit CdS films on materials such as quartz, sapphire, cadmium sulfide, etc. Two problems regarding the thin film deposition immediately arise, i.e., the determination of film thickness and that of the crystal orientation. X-ray diffraction patterns are used to study these problems.

5.4.2 Microwave Measurement of Transducer Coupling Loss.
The microwave evaluation of the transducer efficiency represents a challenging measurement problem. At room temperature, the attenuation of acoustic-wave propagation in the substrate material increases exponentially with frequency. At X-band frequencies this may amount to 50-100 db/cm in most materials. Cryogenic cooling will reduce the attenuation significantly although the complications involved are quite significant.
Figure 5.12 is a block diagram of the measurement setup. A 2J51 magnetron
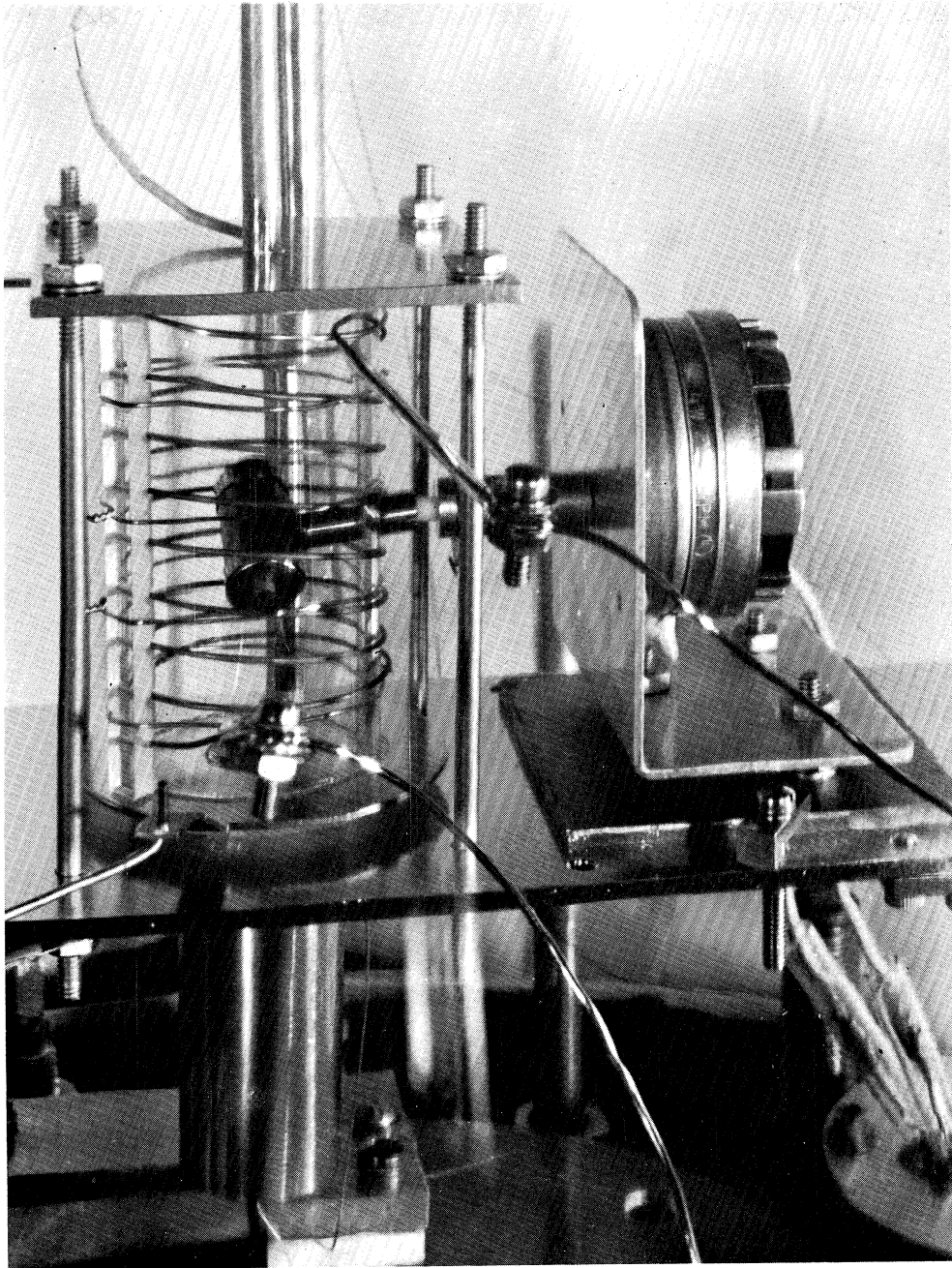
135

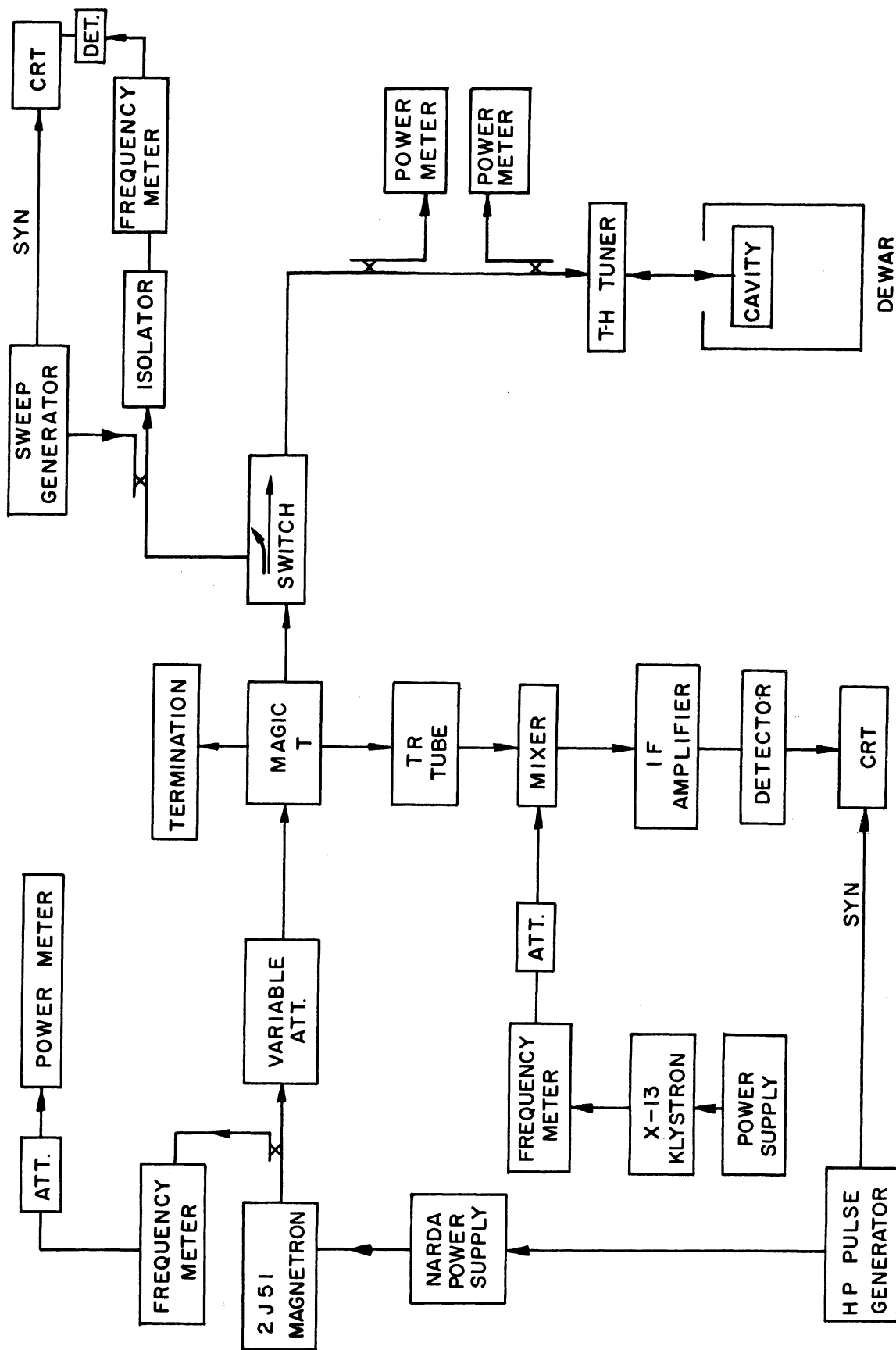FIG. 5.11 EXPERIMENTAL SETUP FOR EVAPORATING THIN CADMIUM SULFIDE FILMS.

FIG. 5.12 BLOCK DIAGRAM OF THE MICROWAVE SETUP FOR EVALUATING THE COUPLING LOSS OF A THIN FILM TRANSDUCER.

137

capable of delivering peak power of 1-4 kw at a pulse width of one micro-second and a prf of 1 kc/s is used as the microwave source in the lower X-band region (8.2-9.8 Gc). The pulse power supply is a Narda pulser capable of delivering up to 25 kv and the pulse width is controlled by another HP pulser. The microwave power is piped into a magic-T which divides the input power into a terminated load and a matched cavity where the transducer is located. The reflected power goes back to the magic-T and feeds into the receiver branch through a protective TR tube. The receiver consists of a balanced microwave mixer, a klystron local oscil-lator, an IF amplifier and a detector. The video output is displayed on a CRT. Two directional couplers connected back to back in the cavity branch enable one to measure both the input power to and the reflected power from the cavity. A side branch operated by a microwave switch in the cavity arm is used to monitor the cavity tuning.

5.4.3 Power Relations. Let P_i be the input power supplied by the signal generator measured at the cavity arm. One portion of it, say P_r, is reflected at the cavity junction and the other portion, P_t, is fed into the cavity. If there are no other losses in the system, then

$$P_t = P_i - P_r = P_i (1 - \gamma) ,$$

where $\gamma = P_r/P_i$.

The power fed into the cavity is used to overcome losses. There is a transducer loss due to (1) coupling of the electromagnetic field to the transducer and (2) transforming it into acoustic power by the piezoelectric effect. These can be grouped together as the coupling loss P_c. There is also loss in the material (the substrate) traversed by the acoustic wave or material loss P_m. Thus

$$P_i(1 - \gamma) = 2(P_c + P_m)$$

or

$$P_c = \frac{P_i(1 - \gamma)}{2} - P_m \quad .$$

The factor of two comes from the fact that the transducer has been used twice and the acoustic wave also travels back and forth along the rod. The material loss P_m is computed from the decay of the echoes in an echo measurement.

$\underline{5.4.4}$ $\underline{The}$ $\underline{Echo}$ $\underline{Measurement}$. An X-cut quartz rod has been used for the first experiment. This is to check out the experimental technique and measurement procedures before thin film transducers are introduced. The quartz rod is inserted into the open end of a re-entrant type cavity mounted at the end of an X-band waveguide which is then lowered into a double jacket dewar and cooled to $4.2°K$. The frequency of the cavity is adjusted to the desired value by a tuning knob on top of the dewar. The magnetron, which is set at the exact frequency of the cavity, is pulse modulated and delivers its output to the cavity. The transducer, which is at the high field region of the cavity, will convert the electromagnetic energy into mechanical energy which in turn excites an acoustic wave. The acoustic wave would travel along the rod and is reflected at the other end and thus travels back toward the cavity and is reconverted into electromagnetic energy. The reflected wave in the wave-guide appears as echoes in the receiver and are displayed on the CRT during the period when the driving pulse is absent. A typical echo pattern obtained by this measurement method is shown in Fig. 5.13. It is evident that the successive echoes appear at a regular interval corresponding to the time required for the acoustic wave to traverse the rod back and forth
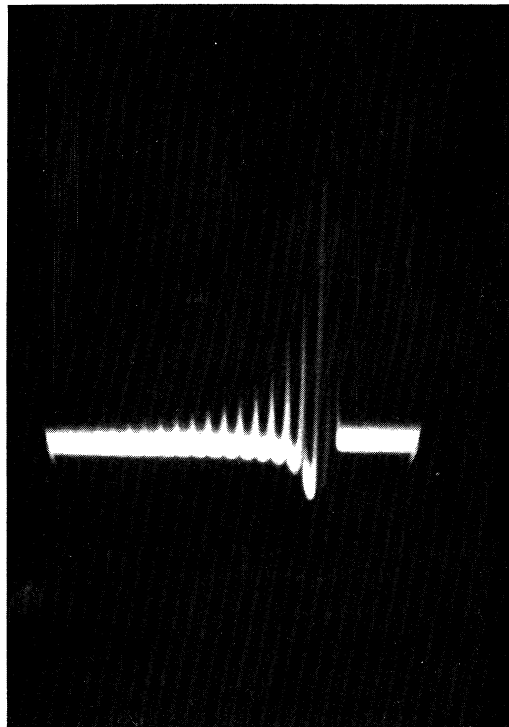
FIG. 5.13 ECHO RETURN FROM AN X-CUT QUARTZ ROD OPERATED AT 9.36 Gc

AT LIQUID HELIUM TEMPERATURE.

and the amplitudes of the successive echoes decay almost exponentially. For an exponential decay, the loss per unit length can be computed. This is the material loss P_m mentioned in the above section.

The loss measured from this run is rather high, amounting to about 1 db/cm which is approximately 10 times larger than it should be. After rechecking the quartz rod by optical methods, it was found that the surface of the rod is not exactly perpendicular to the X-axis and that the two surfaces are off parallel by as much as 30 seconds of an arc. This can account for the high loss of the crystal and also the fact that only 11 echoes were detected on the scope. The crystal is being sent back for reprocessing and the echoes will be rechecked later.

5.5 Conclusions and Recommendations. A simple theory of the traveling-wave phonon amplifier using the piezoelectric effect in a semiconductor crystal has been developed. Equations and graphs are represented to enable one to predict the parameters important to the operation of such devices. The theory is then extended to include the use of the deformation potential for the coupling mechanism between the phonon wave and the drifting electrons (introduced by Spector and others) and to microwave frequency operation where future applications will be important. It is found that high mobility semiconductor materials with suitable carrier concentrations are important and that cryogenic operation is a necessity. It is recommended that future efforts in solid-state plasma research should emphasize wave propagation studies. It has also been suggested that Alfvén wave and helicon wave propagation may be important in both semiconductors and semimetals and should be explored further from the standpoint of device applications.

Due to the importance of the coupling loss in transducers of a phonon-wave amplifier, an elaborate experimental program has been initiated to evaluate the coupling efficiency of thin film CdS transducers applicable to microwave frequency operation. It is most important that the transducer problem be solved before any real progress in phonon-wave amplifiers can be achieved.

6. Recommendations for Further Study   (J. E. Rowe)

Specific recommendations for further investigation were given at the end of each particular section. As a result of these studies it is recommended that investigations be carried on along the following specific lines:

1. Microwave acoustic-wave amplifiers using high deformation materials such as indium antimonide.

2. Thin film transducers for both low and high frequency acoustic-wave amplifiers.

3. Infrared radiation from semiconductors.

4. Various types of ohmic contacts and their effect on instabilities in solids.

5. Theoretical studies on determining criteria for time and spatial instabilities in solids.

No. Copies	
2	Advisory Group on Electron Devices, Attn: Mr. T. Henion, 346 Broadway, Eighth Floor, New York, New York 10013
20	Commander, Defense Documentation Center, Cameron Station, Alexandria, Virginia
1	General Motors Defense Research Laboratories, Attn: Mr. Gail T. Flesher, Box T, Santa Barbara, California
1	Philco Corporation, Lansdale Division, Attn: Mr. J. R. Gordon, Church Road, Lansdale, Pennsylvania
1	Westinghouse Electric Corporation, Applied Research Laboratory, Defense and Space Center, Attn: Mr. S. D. Schreyer, Friendship International Airport, Box 746, Baltimore, Maryland
1	Varian Associates, Central Research Laboratory, Attn: Dr. Herbert Kroemer, 611 Hansen Way, Palo Alto, California
1	General Electric Company, Attn: E. L. Bartels, 118 West First Street, Dayton, Ohio 45402
1	Motorola, Inc., Solid State Systems Division, Attn: Mr. N. G. Sakiotas, 3102 North 56th Street, Phoenix 10, Arizona
1	Radcom Division, Litton Industries, Emertron Information and Control Division, Attn: Mr. R. A. Sparks, 5009 Calvert Road, College Park, Maryland 20740
1	Microwave Electronics Corporation, Attn: Dr. Frank A. Olson, 3165 Porter Drive, Palo Alto, California
1	ITT Research Institute, Attn: H. N. Spector, Chicago 16, Illinois
1	Stanford University, Attn: C. F. Quate, Stanford, California
2	Microwave Associates, Attn: Dr. A. Uhlir, Jr., Burlington, Massachusetts
1	Motorola, Inc., Attn: Mr. William Taylor, 5005 East McDowell Road, Phoenix, Arizona
1	Hewlett-Packard, Inc., Attn: Dr. M. Atalla, 2900 Park Boulevard, Palo Alto, California
1	Texas Instruments Inc., Attn: Dr. J. R. Biard, 13500 North Central Expressway, Dallas, Texas 75222
1	Rome Air Development Center, RALTP, Attn: Mr. H. Chiosa, Griffiss Air Force Base, New York

1   Microwave Associates, Inc., Attn: Dr. Arthur Uhlir, Jr.,
Burlington, Massachusetts

1   United Aircraft Research Laboratory, Attn: Mr. A. W. Penney,
Silver Lane, East Hartford, Connecticut

1   Texas Instruments Inc., Attn: Mr. Philip Thomas, P. O. Box 5012,
Dallas, Texas

1   The University of Arizona, University Library, Tucson, Arizona

1   Electrical Engineering Department, Tulane University, Attn:
Dr. Walter M. Nunn, Jr., New Orleans, Louisiana

1   National Aeronautics and Space Administration, Head, Operations
Section, Scientific & Technical Information Division (SAK/DL),
P. O. Box 5700, Bethesda, Maryland 20014

1   Stanford Research Institute, Attn: G-037 External Reports,
Menlo Park, California 94025

1   Office of Research Administration, Project Files, The University of
Michigan, Ann Arbor, Michigan

15   Electron Physics Laboratory, The University of Michigan, Ann Arbor,
Michigan

DISTRIBUTION LIST

1	Commanding Officer, USAERDL, Attn: SIGRA/SL-PF, Mr. H. Jacobs, Fort Monmouth, New Jersey 07003
1	Chief, Bureau of Ships, Department of the Navy, Attn: Mr. A. Young, 681A1A, Washington, D. C.
1	Commanding Officer, USAELRDL, Attn: SIGRA/SL-PRM, Mr. H. J. Hersh, Fort Monmouth, New Jersey 07003
1	Chief, Bureau of Ships, Department of the Navy, Attn: Mr. C. C. Walker, Room 3337, Code 681A1D, Washington, D. C.
1	Commanding Officer, Naval Air Development Center, Johnsville, Pennsylvania
1	Chief, Bureau of Naval Weapons, Attn: DL13, Navy Department, Washington, D. C.
1	Chief, Bureau of Naval Ships, Attn: 300, Navy Department, Washington, D. C.
1	Director, USAEL, Headquarters USAECOM, Attn: AMSEL-RD-ADT, Fort Monmouth, New Jersey 07003
1	U. S. Army Research Office, Box CM, Duke Station, Durham, North Carolina 27706
1	Naval Research Laboratories, Attn: Earle Ditzel, 5212F, Washington, D. C.
1	Director, NASA, Langley Research Center, Langley Air Force Base, Virginia
1	The Pentagon, Room 3E-1065, Technical Library, Washington, D. C.
1	Director, ARPA, Attn: C. F. Yost, Room 3D155, The Pentagon, Washington, D. C.
1	Marshall Space Flight Center, Research Projects Division, Attn: R-RP-S, W. J. Robinson, Huntsville, Alabama
1	National Security Agency, Attn: Mr. J. T. Tippett, Fort George G. Meade, Maryland
1	Harry Diamond Laboratories, Attn: Library, Room 211, Building 92, Washington, D. C. 20438
1	Sandia Corporation, Sandia Base, Albuquerque, New Mexico
2	Scientific & Technical Information Facility, Attn: NASA Representative (SAK/DL), P. O. Box 5700, Bethesda, Maryland 20014